BRNO UNIVERSITY OF TECHNOLOGY

VYSOKÉ UČENÍ TECHNICKÉ V BRNĚ

FACULTY OF MECHANICAL ENGINEERING

FAKULTA STROJNÍHO INŽENÝRSTVÍ

ENERGY INSTITUTE

ENERGETICKÝ ÚSTAV

VORTEX INDUCED VIBRATIONS

KMITÁNÍ VYVOLANÉ VÍRY

BACHELOR'S THESIS

BAKALÁŘSKÁ PRÁCE

AUTHOR — Beáta Szarka

AUTOR PRÁCE

SUPERVISOR — doc. Ing. Pavel Rudolf, Ph.D.

VEDOUCÍ PRÁCE

BRNO 2024

BRNO UNIVERSITY OF TECHNOLOGY
FACULTY OF MECHANICAL ENGINEERING

Assignment Bachelor's Thesis

Institut:	Energy Institute
Student:	**Beáta Szarka**
Degree programm:	Fundamentals of Mechanical Engineering
Branch:	Fundamentals of Mechanical Engineering
Supervisor:	**doc. Ing. Pavel Rudolf, Ph.D.**
Academic year:	2023/24

As provided for by the Act No. 111/98 Coll. on higher education institutions and the BUT Study and Examination Regulations, the director of the Institute hereby assigns the following topic of Bachelor's Thesis:

Vortex induced vibrations

Brief Description:

Energy harvesting based on vortices generated by the flow around a body is a relatively new topic. It makes use of periodically shedding vortex structures behind a body in a stream of water that is connected to an electrical generator. The problem is being addressed in the Horizon Europe H–HOPE project.

Bachelor's Thesis goals:

The student will research the possibilities and already implemented solutions for energy harvesting using vortex–induced oscillations. Subsequently, using CFD, the student will model the vortex flow behind a body in a stream for its different shapes and evaluate the forces acting on the body.

Recommended bibliography:

BISHOP, R.E.D. Kmitání. SNTL, 1978.

JANALÍK, J. Obtékání a odpor těles [online]. 2008 [cit. 2023-11-02]. Vysoká škola báňská – Technická univerzita Ostrava.

BURESTI, G. Vortex shedding from bluff bodies. In: RIERA, J.D. a DAVENPORT, A.G. Wind Effects on Buildings and Structures. 1998.

BERNITSAS, M.M.; RAGHAVAN, K.; BEN-SIMON, Y. a GARCIA, E.M.H. VIVACE (Vortex Induced Vibration Aquatic Clean Energy): A New Concept in Generation of Clean and Renewable Energy From Fluid Flow. J. Offshore Mech. Arct. Eng. 2008, roč. 130, č. 4.

Deadline for submission Bachelor's Thesis is given by the Schedule of the Academic year2023/24

In Brno,

L. S.

doc. Ing. Jiří Pospíšil, Ph.D. Director of the Institute	doc. Ing. Jiří Hlinka, Ph.D. FME dean

ABSTRACT

This thesis deals with vortex-induced vibrations on different bluff body cross-sections. The theoretical part provides an overview of current energy production trends and introduces a hydrokinetic energy harvester, the VIVACE converter. The main principle of the system is a bluff body immersed in fluid flow undergoing vortex shedding formulating Kármán vortex street. The practical part deals with the evaluation of different profiles by forces acting on the bodies, frequency, and Strouhal number using 2D CFD simulations. The output of the investigation is the selection of the ideal cross-section shape of a cylinder for a VIVACE converter.

KEYWORDS

Vortex-induced vibrations, vortex shedding, Kármán vortex street, Strouhal number, hydrokinetic energy harvester, VIVACE converter, CFD

ABSTRAKT

Tato bakalářská práce se zabývá kmitáním vyvolaném vírami na různých průřezech. Teoretická část poskytuje přehled současných trendů výroby energie a představuje typ hydrokinetického sběrače energie VIVACE konvertor. Hlavním principem systému je odtrhávání víru a vznik Kármánové vírové stezky podél tělesa ponořeného do proudící tekutiny. Praktická část se zabývá vyhodnocením různých profilů podle sil působící na těleso, frekvencí a Strouhalového čísla pomocí 2D CFD simulací. Výstupem je výběr ideálního tvaru průřezu válce pro konvertor VIVACE.

KLÍČOVÁ SLOVA

Kmitání vyvolané víry, odtrhávání víru, Kármánova vírová stezka, Strouhal number, hydrokinetický sběrač energie, VIVACE konvertor, CFD

ROZŠÍŘENÝ ABSTRAKT

Bakalářská práce se zabývá výzkumem kmitání vyvolanýho víry, na jehož principu je založená jedna z nových forem obnovitelných zdrojů energie: konvertor VIVACE. Tento druh sběrače hydrokinetické energie využívá odtrhávání vírů z povrchu obtékaného tělesa. Konstrukčně zahrnuje těleso ponořené pod hladinu nádrže. Vzniklé střídavě odtrhávající se víry způsobují nerovnoměrné rozložení tlaku na povrchu, kvůli čemu se obtékané těleso dává do pohybu. Předložená práce zahrnuje stručné shrnutí poznatků o existujících formách obnovitelných zdrojů energie, teoretický popis obtékání těles a vznik Kármánovy vírové stezky. Dále numerické simulace obtékání různých těles a jejich porovnávání z pohledu jejich použitelnosti pro systém VIVACE.

Teoretická část začíná popisem existujících forem obnovitelných zdrojů energie. Stručně charakterizuje sluneční a větrné energie a udává přehled o roční maximální čisté výrobní kapacitě elektráren využívajících obnovitelné zdroje energie v České republice. Dále zahrnuje rozvoj hydroelektrické energie a zavádí pojmy forem výroby hydroenergie. Dnes nejrozšířenějším způsobem je vodní elektrárna, jejíž druhy jsou probrané podrobněji. Tato forma výroby energie využívá potenciální energii kapaliny a pomocí turbín ji přemění na elektřinu. Dalším způsobem jsou hydrokinetické systémy, které využívají kinetickou energii proudící kapaliny. Do této kategorie patří harvestor VIVACE, což je konkrétně bezturbínový proudový hydrokinetický systém.

Další sekce teoretické části je věnována k porozumění teoretickému zázemí obtékání těles. Pokud je těleso obtékané reálnou kapalinou, tak kvůli smykovému napětí se odporová síla skládá z třecího odporu a z odporu tvarového. Velikost odporové síly závisí na vícero faktorech. Jeden z nich je tvar tělesa, který může být tzv. špatně obtékané nebo aerodynamické těleso. U aerodynamických profilů proudnice sledují povrch tělesa, kvůli čemuž je tlakový odpor zanedbatelný. Naopak u špatně obtékaných těles je tlakový odpornejvýznamnější a dojde k odtrhávání mezní vrstvy. Špatně obtékaná tělesa jsou dále dělena na zaoblené a hranaté geometrie. Toto dělení je důležité kvůli bodu separace víru: hranaté tvary mají zafixovaný bod separace naopak u zaoblených tvarů poloha tohoto bodu závisí mj. na Reynoldsově čísle. Od jisté velikosti Reynoldsova čísla u obtékaného tělesa dochází ke střídavému odtrhávání úplavu, který je dále unášen ve směru proudění. Tento jev se nazývá Kármánova vírová stezka podle maďarského vědce židovského původu Theodora von Kármána. Kvůli tomuto jevu se rozložení tlaku periodicky mění. Vzniklou tlakovou sílu z můžeme rozložit na sílu odporovou a vztlakovou. Velikost vztlakové síly u tělesa, které má nula stupňů volnosti, se mění s frekvencí odtrhávání víru.

Poslední část rešerše se zabývá systémem VIVACE. Nejjednodušší schéma se skládá z tělesa, které je ponořeno do kapaliny, z pružiny, z ložiska, z ozubného převodu a z generátoru. U systému, kde těleso už není zafixované, periodická změna vznikající síly vyvolává oscilaci obtékaného tělesa. Kinetická energie této oscilace pomocí ozubeného převodu a generátoru se převádí na elektrickou energii. Tato sekce dále odvozuje pohybovou rovnici systému. Rovnice je odvozena z Lagrangeovy rovnici druhého druhu a tato rovnice je využívaná k výpočtu výkonu a účinnosti.

Praktická část se zabývá výpočtovou simulací obtékaného tělesa. Výpočet byl prováděn pomocí softwaru studentské verze Ansys Fluent. Analýza byla značně zjednodušená kvůli experimentálním řešením: namísto reálného tělesa, geometrie byla zjednodušená na 2D. Těleso bylo uložené nepohyblivě, okrajové podmínky u hladiny a u spodního povrchu nádrže byly branné jako symetrie a jako okrajová podmínka pro hranici tvaru byla použita podmínka ulpívání. Simulace byly prováděné pro různé rychlosti, u pěti průřezů: kruhového, elipsového, čtvercového, obdélníkového a trojúhelníkového. Pro modelování turbulence byl zvolen model SST k-ω, který používá k výpočtu RANS rovnice. Tento model je vhodný pro modelování mezní vrstvy.

Poslední kapitoly se věnují popisu a porovnávání provedených numerických simulací. Tělesa byly zkoumané z pohledu působících sil a podle frekvencí odtržení mezní vrstvy. Podle těchto vstupů bylo vypočítáno Strouhalovo číslo. Tyto parametry sloužily pro porovnávání různých geometrií. Dále bylo zkoumáno rozložení tlaku a rychlosti v doméně a odtržení mezní vrstvy (pomocí vířivosti). U pozorování vířivosti byl dobře viditelný zmíněný jev z teorie o poloze bodu separace. Dále se dalo vidět, že u hranatých těles se po odtržení mezní vrstvy dojde k jejich opětovnému připojení k povrchu, což způsobuje rušení v průběhu funkcí sil. Největší síly vyšly pro čtvercový průřez a nejmenší síly pro kruhový průřez. U frekvencí je tomu naopak. Aby bylo možné vypočítat výkon, bylo by potřebné znát i vychýlení. Bez této informace se dá jen předpokládat, že největší výkon by měl mít čtvercový průřez. U vypočítaných Strouhalových čísel (hlavně u čtvercového průřezu) je mírná odchylka vůči experimentálním datům. Tato odlišnost je pravděpodobně zapříčiněna okrajovými podmínkami a také zjednodušením problematiky.

Závěrem lze říct, že navzdory odlišnosti vůči experimentálním hodnotám pomocí CFD, lze dobře předpokládat chování obtékaných těles s různými průřezy a jejich charaktakteristiky odtrhávání víru. Tato bakalářská práce by měla přinést další cenné výsledky a poskytnout informace o jevu odtržení víru pro budoucí výzkum v této oblasti.

BIBLIOGRAPHIC CITATION

SZARKA, Beáta. *Kmitání vyvolané víry* [online]. Brno, 2024 [cit. 2024-05-20]. Dostupné z: https://www.vut.cz/studenti/zav-prace/detail/158151. Bakalářská práce. Vysoké učení technické v Brně, Fakulta strojního inženýrství, Energetický ústav. Vedoucí práce Pavel Rudolf.

DECLARATION

I hereby declare that this bachelor's thesis, titled "Vortex induced vibrations" is my original work and has been written according to the instructions of my supervisor, doc. Ing. Pavel Rudolf, Ph.D. All sources of information and data used in this thesis have been appropriately cited and referenced in the bibliography.

_____ _____

Datum Beáta Szarka

ACKNOWLEDGMENT

I want to express my sincere gratitude to my supervisor, doc. Ing. Pavel Rudolf, Ph.D., for his invaluable guidance, insightful feedback, and unwavering support throughout the development of this thesis. His expertise and dedication have been crucial to the successful completion of this research. I also wish to thank Ing. Petr Boháč for his assistance and helpful advice, which significantly contributed to the depth and quality of this work. This thesis would not have been possible without their expert guidance and support.

TABLE OF CONTENTS

INTRODUCTION

Throughout history, man always looked for ways to produce energy. The need for energy production these days is a more serious problem than in the past. At the beginning of the 21st century, humanity had to face the problem of global warming leading to recognition of the importance of the sustainability mindset. This green mindset affected the energy industry which resulted in the emergence of new research areas. The quest is to produce energy more efficiently while remaining carbon neutral.

One of these innovative approaches is the energy harvesting from the hydrokinetic energy of the vortex-induced vibrations. The principle behind this device lies in the formation of the Kármán vortex streets behind a cylinder placed into fluid flow which phenomenon induces the displacement of the body. Despite that in general this is an unwanted effect, which causes a lot of difficulties in the building structure design process, using a VIVACE converter the hydrokinetic energy of the flow can be transferred into mechanical energy which is later converted into electricity. The energy production of the system is closely related to the choice of the bluff body cross-section shape.

The goal of this thesis is to understand boundary layer separation and the formation of the Kármán vortex street to be able to perform CFD analysis on various cross-sections of the bluff body used for the VIVACE converter. The main point of the examination is to observe the static parameters of each shape immersed in flowing fluid with a 0 degree of freedom while changing the velocity of the medium. For all the simulations the lift and drag force, and frequency are evaluated.

The theoretical part of the thesis provides an overview of green energy sources and summarizes the existing hydropower and hydrokinetic energy harvesting technologies. It further investigates the physical background of a fluid passing through a cylinder, boundary layer separation, and formation of the Kármán vortex street. The last section of this part introduces the VIVACE converter while providing data about the lab model realized at the University of Michigan and provides an overview of the mathematical model that represents the dynamics of the system.

The practical part mainly focuses on the simulations realized with the software Ansys Fluent. It's important to mention, that the simulations were carried out in the most simplified configurations by neglecting multiple factors. The goal of this part is to understand the basics of CFD, become familiar with the process of realizing a CFD analysis and based on the gained experience perform an investigation about which cross-section would be optimal to fulfill the requirements of a VIVACE converter.

This thesis should provide an overview of the behavior of various geometrical shapes placed in fluid flow and summarize its different parameters.

1 RENEWABLE ENERGY SOURCES

1.1 INCREASE OF ENERGY NEEDS AND ITS WAYS AND DIFFICULTIES TO FULFILL THEM

Our energy demand varies and changes due to multiple factors in each household. In general, energy usage grows with the growth of the population, global warming, the development of the efficiency of production technologies, etc. Nowadays major part of energy is produced with fossil fuels however, these energy sources are not at our disposal in infinite quantities.

Fossil fuels, including coal, crude oil, and natural gas, fall under this category. The reason behind their notable carbon-rich composition is the way of their formation: from the fossilized, buried remnants of ancient plants and animals that thrived millions of years ago [1].

Using and producing fossil fuels has its advantages and disadvantages. One significant benefit of fossil fuels is their ability to produce substantial electricity at a single site. This source of energy is available in many areas. Coal, when utilized in power plants, offers a cost-effective solution and is available in abundance. Additionally, the transportation of oil and gas to power stations is simplified by using pipelines, making the process straightforward.

On the other hand, their production is responsible for land degradation, major water pollution, and emissions, not talking about burning them which drives global warming as well. The combustion of fossil fuels results in the significant release of carbon dioxide. Carbon emissions create a greenhouse effect in the atmosphere, contributing to changes in the climate. In the United States, fossil fuel combustion, especially within the power and transportation sectors, is responsible for approximately three-fourths of our carbon emissions [2]. Also, fossil fuels are highly influenced by geopolitics. Russia‘s invasion of Ukraine put Europe under pressure geopolitically. It forced the European Union to evaluate the risks of using these types of energy sources because of the lack of resources [3].

The energy sector in the EU contributes to over 75% of the region's greenhouse gas emissions. Therefore, elevating the proportion of renewable energy in various sectors of the economy is a fundamental element in achieving the EU's energy and climate goals and transforming into a carbon-neutral continent by 2050. The Commission unveiled the REPowerEU strategy on May 18, 2022, presenting a range of actions to swiftly diminish the EU's reliance on Russian fossil fuels well in advance of 2030. This strategy aims to expedite the transition to clean energy sources. On 30 March 2023, the European Parliament and the Council reached a provisional agreement to elevate the mandatory renewable energy objective to a minimum of 42.5% by 2030. [4]

1.2 FORMS OF RENEWABLE ENERGY

The law of conservation of energy states that energy can neither be created nor destroyed; rather, it can only be transformed or transferred from one form to another. Renewable energy refers to energy harnessed from natural sources that are replenished more quickly than they are used up. Although we often consider renewable energy as a modern technology, the utilization of nature's energy has a rich history in applications like heating, transportation, lighting, and more.

Presently, the renewable energy sector is a well-established and expanding industry, offering a variety of technologies. We can differentiate forms of renewable energy based on their sources such as biofuel, biomass, geothermal, hydro, solar, tidal, and wave power.

The most mainstream of all the energy sources is solar energy. It's popular because power plants can be built not only in rural areas but also in urban areas. Solar technologies convert sunlight energy to electricity through photovoltaic panels or mirrors concentrating solar radiation. The manufacturing costs of solar panels decreased through the years which makes this technology more accessible for households. [5]

The kinetic energy of moving air is harnessed by large wind turbines. The advantage of this powerplant is that it can be located onshore and offshore too. The amount of electric energy production depends on the wind velocity and the diameter of the turbines. Because of the high flow velocity, there is a high potential for offshore wind power. [5]

Countries all around the world implement renewable energy sources based on their locational availability and efficiency in their energy production. Figure 1.2-1 represents the maximum net generating capacity of power plants and other installations that use renewable energy sources to produce electricity in the Czech Republic in the past decade. As we can see the leading R.E.S. is bioenergy followed by hydropower.

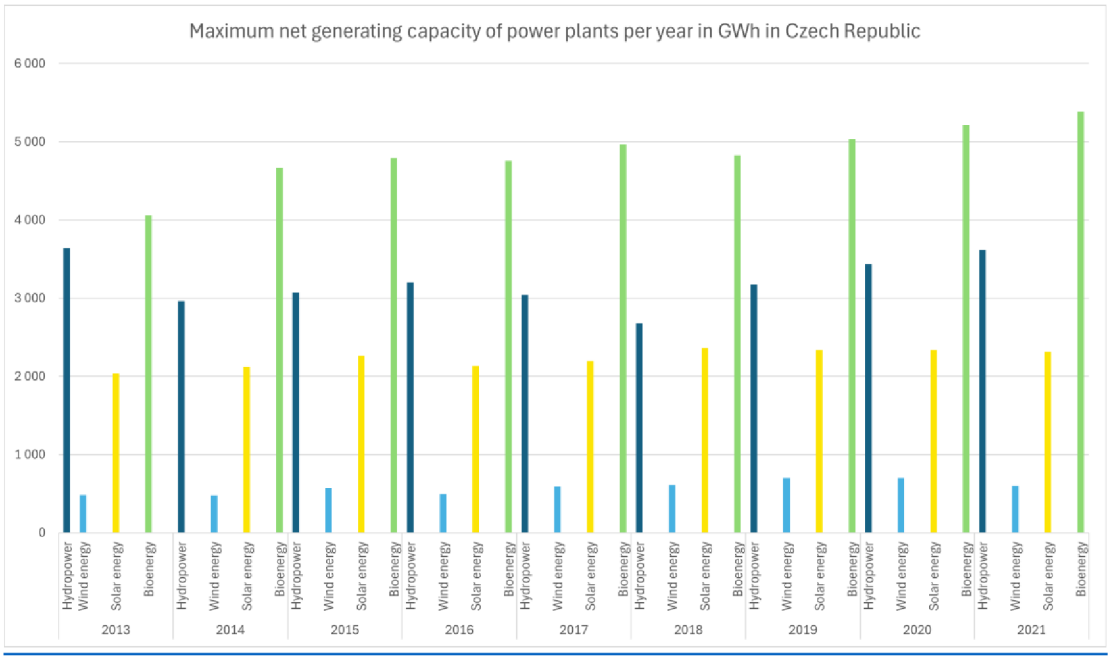

Figure 1.2-1 *Maximum net generating capacity of power plants per year in GWh in Czech Republic, chart made based on data adapted from [6]*

1.3 PAST AND PRESENT OF HYDROPOWER

Harnessing the energy of water for work has been a practice among humans for millennia. More than two millennia ago, the Greeks used water mills to do various tasks, and during the third century B.C., the Egyptians utilized Archimedes water screws for irrigation [7].

Figure 1.3-1 *Water wheel in Pamplemousses rum distillatory from the 18th century*

During the late 18th century, hydraulic power became the essential energy source that fueled the commencement of the Industrial Revolution (Figure 1.3-1). Bernard Forest de Bélidor, a French hydraulic and military engineer, authored "Architecture Hydraulique," a comprehensive four-volume publication detailing machines with vertical and horizontal axes. Without electrical generators (which were invented at the end of the 19th century), knowledge about hydraulics was essential to the development of the hydroelectrical industry. This made a lot of inventors think about the problem and the time of new inventions in this field of study began. Around the same time, a Hungarian engineer and inventor Johann Segner invented the Segner Wheel, which was a version of a reactive water turbine having a vertical axis. This served as a prototype for a lot of the modern water turbines. [8]

In 1878 the first hydroelectric project made its debut. In Northumberland (England), water was used to power a single lamp. This was a private project, so the Schoelkopf Power Station in Niagara (Figure 1.3-2) is considered the first major step in this industry. The powerplant collapsed on July 7th, 1956, which exact cause is still a mystery. Two of the station generators were destroyed and the third was severely damaged. The collapse served as a great motivation for the construction of the Robert Moses Niagara Power Plant, to replace the old power station. It was opened in 1961 and still runs today. [9][10][11]

In 1913 Viktor Kaplan invented his type of water turbine, the Kaplan turbine. It was a water turbine with adjustable blades that helped with achieving the required efficiency in a wide range of flow. The turbine is still the most widely used propeller-type water turbine in the world [10][12].

Figure 1.3-2 *Schoelkopf Power Station in Niagara, Sept. 21, 1925, adapted from [13]*

Since then, the field of the hydroelectric industry has gone through a lot of innovations. Time by time engineers all around the world started to invent new forms of harvesting energy from the kinetic energy of the water. The goal remained the same, only the devices went through a major evolution. Nowadays the most popular form of this type of energy harvesting is the hydropower facilities. An estimated 62 500 power plants are operating in the world. The largest one is located in China on the Yangtze River, which is called as Three Gorges Dam. With its installed capacity of 22 500 MW, it's not only the largest hydroelectric powerplant but overall, the largest powerplant in the world. [14]

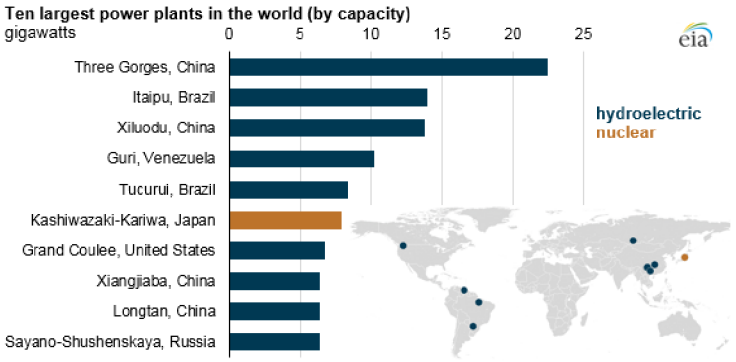

Figure 1.3-3 *Largest power plants in the world by capacity, adapted from [14]*

Hydropower facilities vary in size and ways of functioning. There are three main types of this powerplants: impoundment, diversion, and pumped storage. [15]

An impoundment facility (Figure 1.3-4) is the most common type of hydroelectric power plant. It uses a dam to control the water flow. In the reservoir, the potential energy of the water grows. As the water spills over the top of a dam or flows down a hill, this potential energy is converted into kinetic energy The water flows through a turbine which starts to spin, generating. With the regulation of the flowthrough, electricity production can be managed to match the needs of customers. [16]

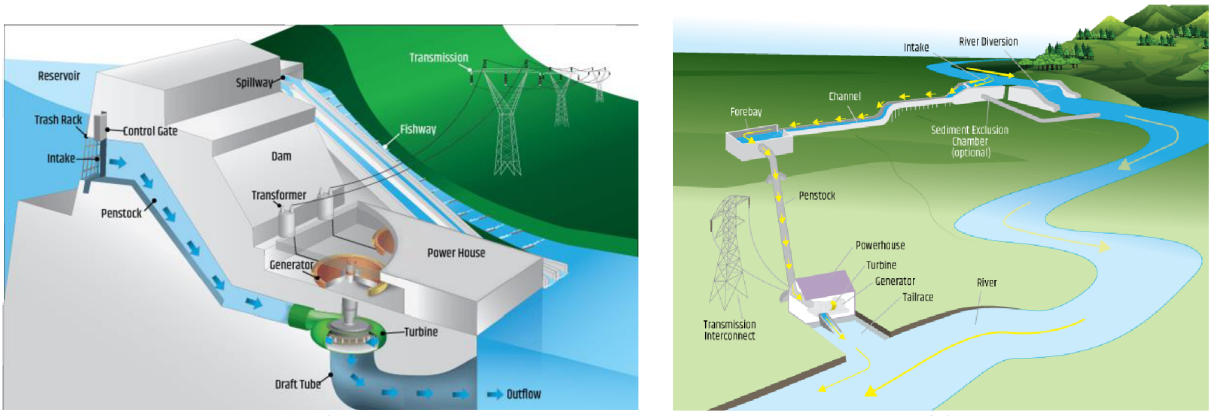

a) b)

Figure 1.3-4 a) *Impoundment facility functioning scheme, adapted from [17],* ***b)*** *Diversion facility functioning scheme, adapted from [17]*

The diversion (often called „run-of-river“) facilities (Figure 1.3-5) do not need a reservoir or a dam to function. It uses canals to redirect the flow to the generator. The disadvantage of these types of facilities is that they can't work as flood control. [17]

The third type is a pumped storage facility (Figure 1.3-6) which works as a giant battery. It stores the electricity generated by another source in the form of the potential energy of water by pumping the water from a lower-elevation reservoir to a higher elevation. Based on the current electricity demands, the water can be released back to the lower elevation reservoir, flowing through a turbine and generating more electricity. [17]

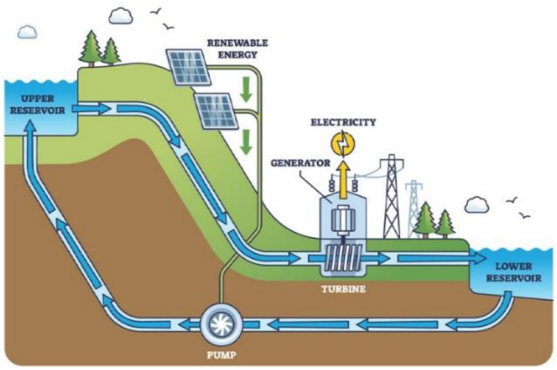

Figure 1.3-5 *Pumped hydropower facility functioning scheme, adapted from [18]*

In the past few paragraphs, we discussed the energy harvesting facilities used on a river, but these unfortunately can't be applied on the ocean or seas. Marine energy technologies use the kinetic energy of waves, currents, and tides. Wave energy technologies harness the motion of ocean and sea waves to generate electricity. The quantity of energy produced is contingent on factors such as the velocity, height, and frequency of the waves, along with the density of the water. There are seven main types of these devices: attenuators, point absorbers, pressure differentials, oscillating water columns, overtopping, and oscillating wave surge converters (Figure 1.3-7). [19]

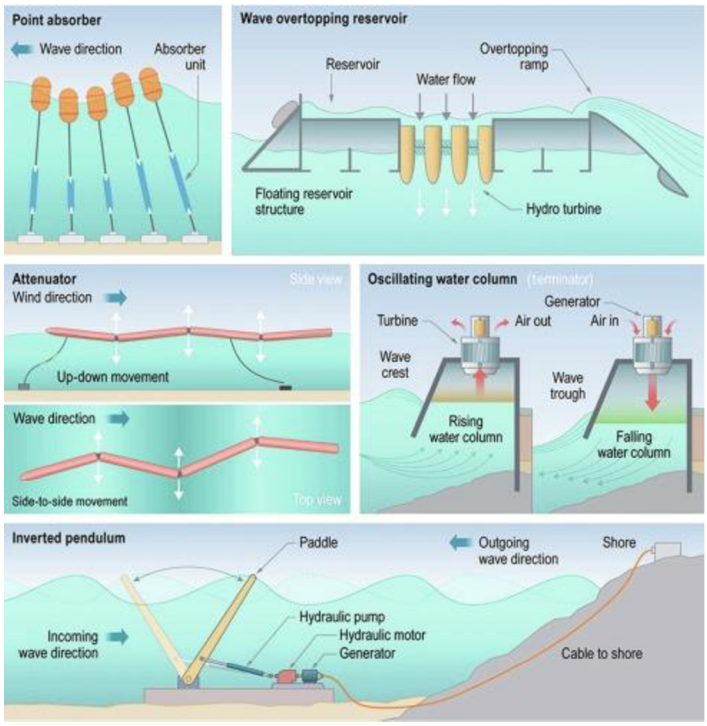

Figure 1.3-6 *Types of wave energy converters, adapted from [20]*

Energy from flowing currents can be harnessed in tidal channels, ocean currents, or rivers. Strong ocean currents arise from the interplay of temperature, wind, salinity, bathymetry, and the Earth's rotation. The most common types of current energy converters are axial flow turbines, cross-flow turbines, reciprocating devices, tidal kites, Archimedes screws, and vortex-induced vibration. [21]

Another form to extract the kinetic energy of the flowing water is hydrokinetic turbines (Figure 1.3-8). The technology is similar to wind turbines, on the contrary, they are placed into free-stream rivers. Unlike hydropower facilities, the system does not require a dam or reservoir, which allows their placement in areas where building a dam is unfeasible. Their simple design leads to low-cost installation. The turbine can be classified into two categories based on how its rotational axis aligns with the direction of water flow: axial flow and cross flow. [22]

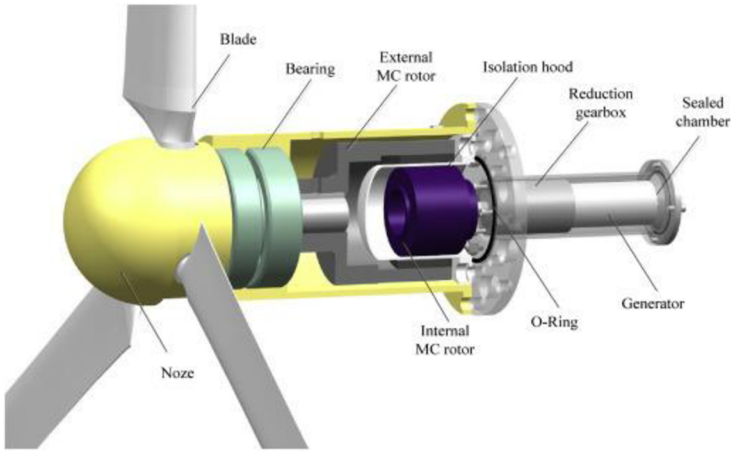

Figure 1.3-7 *Design parts of a hydrokinetic turbine [23]*

1.4 ENERGY HARVESTING FROM VORTEX-INDUCED VIBRATIONS – VIVACE SYSTEMS

Vortex-induced vibration aquatic clean energy (later referred to as VIVACE) is an energy converter that harvests energy from ocean or river current, often referred to as slow water current converter, and still fulfills the environmental requirements. This technology can't be compared to regular hydroelectric power plants, as it doesn't use turbines or dams. It was invented by Bernitsas and Raghavan and patented through the University of Michigan. [24]

Vortex-induced vibrations normally cause enormous damage to different engineering structures causing engineers a lot of struggles (Figure 1.4-1 a). When a bluff body is placed in a fluid stream, the flow lines deviate from the body's contours and disengage from it. Depending on the body's geometry and the flow velocity, periodic vortices, referred to as Strouhal vortices, develop and detach from the low-pressure wake of the body, resulting in the phenomenon known as vortex shedding. If the frequency of this periodic shedding matches the natural frequency of the object, due to resonance it can cause large amplitude oscillations. This repeating pattern of vortices is called Kármán vortex street.

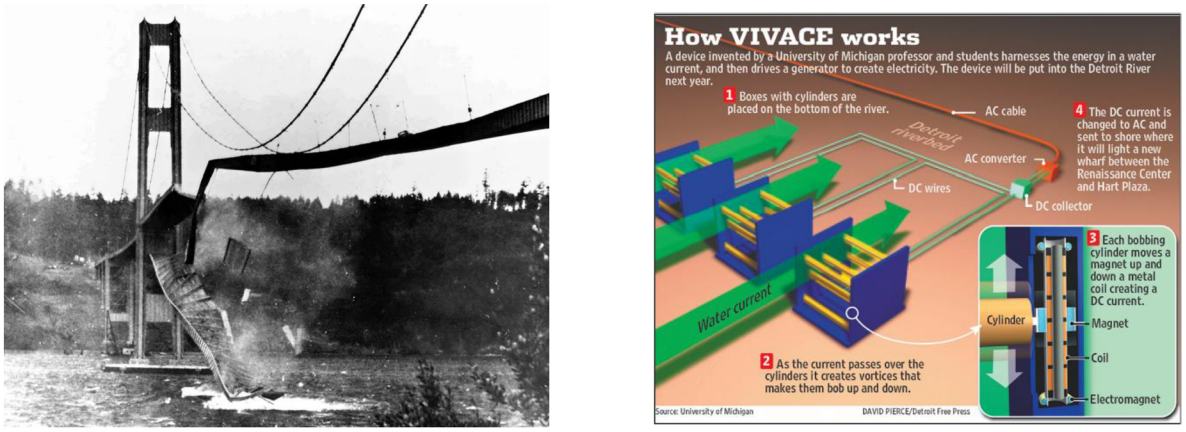

a) b)

Figure 1.4-1 a) *Tacoma Narrows Bridge collapse in 1940, adapted from [25],* ***b)*** *VIVACE technology, adapted from [26]*

The VIVACE (Figure 1.4-1b) instead of minimalizing the vortex shedding maximizes it. The device itself consists of cylinders placed between two „railroads", which are attached to the seabed. As the water current flows through the powerplants it creates vortices behind the cylinders and makes them move up and down. This movement is captured inside the railroad where a magnet moves with the cylinder around a coil, generating DC. For more efficient transport the DC is transferred to AC [26].

The goal is to create a profile generating optimal vibration as a result of its interaction with water flow. The vibrations increase as the flow becomes more turbulent [21].

2 PHYSICS BEHIND VIVACE SYSTEMS

2.1 BLUFF BODY FLOWS

If an ideal fluid flows past a body (viscosity is zero), the streamlines follow the shape of the body, the flow field is symmetrical around the vertical and horizontal axes and therefore the drag is zero. However, if the flowing fluid is real, total drag is caused by skin friction drag and pressure drag, which is caused by the asymmetric distribution of pressure on the surface of the body and contributes to the formation of the drag force. Drag force was defined by Newton as it's found to be proportional to the square of the velocity of the object [27][28]:

$$F_D = \frac{1}{2} C \rho S v^2 \tag{2.1.1}$$

Where v is the flow velocity
C is the drag coefficient
ρ is the density of the fluid
S is the projected frontal area of the body.

However, due to the forces acting, the surface of the solid body also tries to bind the fluid to itself, which leads to the fluid adhering to the surface (no-slip condition). Because of intermolecular attraction and pressure forces acting between the layers, the layer above this adherent fluid layer will not be able to simply tear itself away from it, resulting in any flow flowing around a body being tempted to follow the profile of the surface [29].

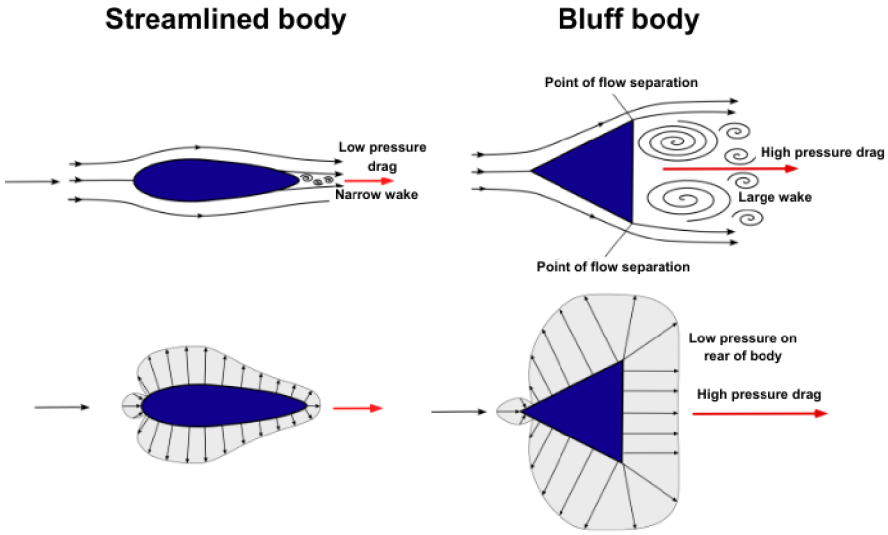

Figure 2.1-1 *Streamlined and bluff body comparison, adapted from [30]*

From an aerodynamic point of view, we distinguish between two body types (Figure 2.2-1): streamlined shapes and non-streamlined shapes (called bluff bodies). The characteristic of a streamlined shape is that the streamlines follow the surface of the body so the drag from the pressure distribution is negligible, its main source is wall shear stress, so the resulting drag coefficient is small. A typical hydrodynamic boundary layer developing around the body is largely influenced by the viscosity [29]. However, the total drag on bluff bodies is typically dominated by the pressure drag component. It's caused by the large low-pressure zone produced in the wake at the

rear of the body. For bluff bodies is typical that the boundary layer or flow begins to detach itself from the body surface. This is referred to as a boundary layer separation [30].

The value of the drag coefficient is determined with experiments provided in a wind tunnel. Drag coefficients for standard two-dimensional and three-dimensional bluff body shapes serve as valuable tools for engineers. These shapes can be further classified into two main sub-categories: bluff bodies with sharp angular shapes and bluff bodies with smooth contours. Those with sharp angular shapes tend to have fixed points of flow separation and drag coefficients that are less sensitive to the Reynolds number, while those with smooth contours (Figure 2.1-2) have variable points of flow separation that rely more on the Reynolds number [30].

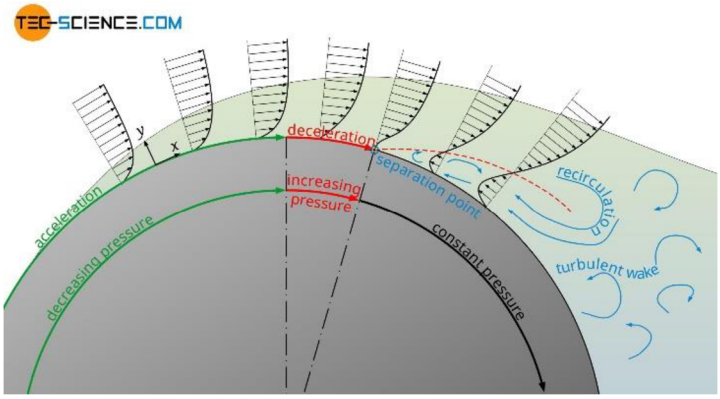

Figure 2.1-2 *Boundary layer separation of the bluff body with smooth contours, adapted from [29]*

After the separation point, we can conclude that the flow is no longer attached to the body resulting in the skin friction drag being almost zero (because wall shear stress is zero). However, the turbulent wake dissipates energy leading to pressure drop causing a substantial increase in pressure drag.

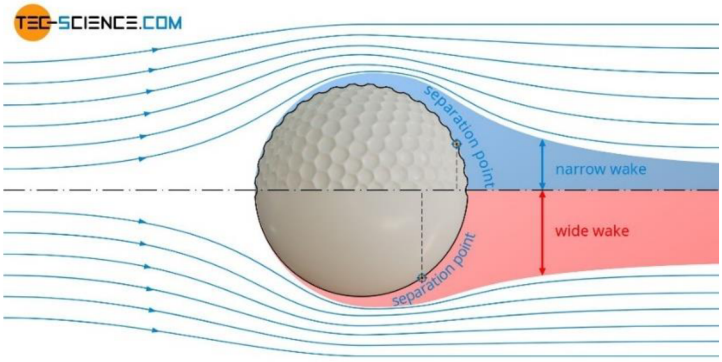

Figure 2.1-3 *Boundary layer separation comparison of a smooth and textured surface on a golf ball, adapted from [29]*

Generally, laminar flow reduces flow losses around the body, but only in case there is no boundary layer separation. However, if this effect occurs, turbulent boundary layers should be targeted. Increased momentum transfer among fluid layers leads to a steeper velocity gradient within the boundary layer resulting in the turbulent boundary layer following longer the body profile. In this case, the separation point shifts downstream causing the turbulent wake to be narrower, which reduces the flow losses

and the pressure drag. A great example of this is a golf ball (Figure 2.1-3). The dimples cause vortices generating a turbulent flow which makes the ball fly further [29].

2.2 FLOW PAST A CIRCULAR CYLINDER

A well-studied example of a two-dimensional bluff body is a circular cylinder. In the previous chapter was discussed how the value of the drag coefficient is influenced by the Reynolds number (2.2.1) in the case of a smooth body.

$$Re = \frac{D_{ch} v}{\nu} \tag{2.2.1}$$

Where D_{ch} is the characteristic length of the bluff body
v is the velocity of the flow
ν is the kinematic viscosity of the flow

The flow about the cylinder and the resulting wake structure and drag coefficient are sensitive to the value of the Reynolds number which is represented in Figure 2.2-1 [30].

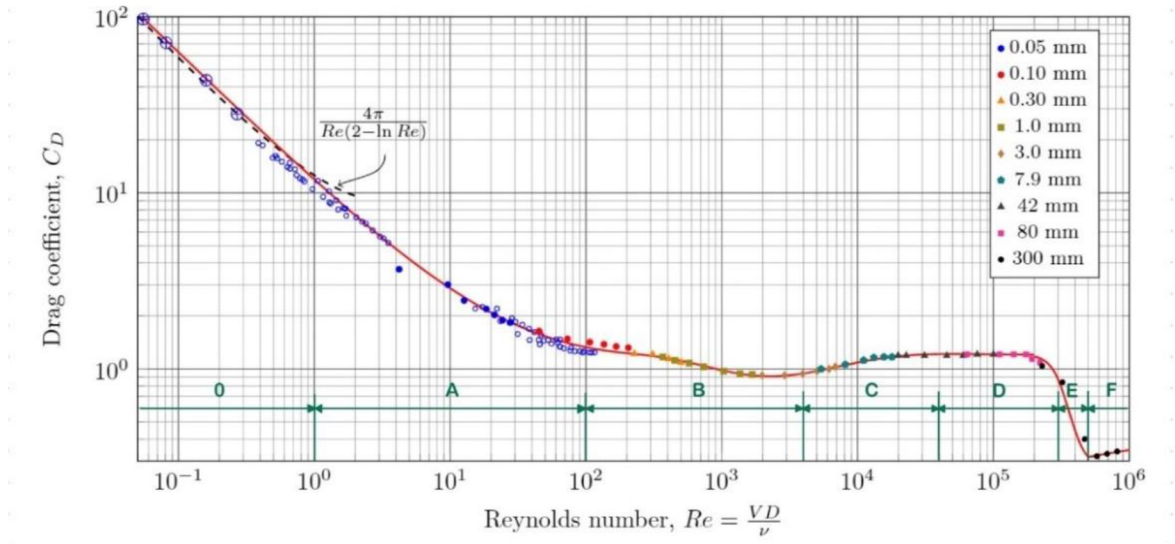

Figure 2.2-1 *Variation in the coefficient of drag with various Reynolds numbers for circular cylinder, adapted from [32], modified based on the graph from [27]*

In the graph referred to as area „0“ is a flow with a low Reynolds number, which is often called a „creeping flow“ or Stokes flow. At this stage, the behavior of the flow is more influenced by viscosity effects than the effects of inertia. [27]

Area A represents flow conditions by Reynolds number being 1<Re<100, where the value of the drag coefficient with increasing Reynolds number rapidly decreases. For Re>1 the flow starts to behave more asymmetrically. For Re=6,26 symmetrically to the horizontal axis of the cylinder fixed pair of vortices start to formulate after the body. With an increased Reynolds number the size of the vortices and the angle characterizing the point of separation „S“ also shows an increasing character. At Re=40 the character of the vortices starts to show asymmetry. At Re>60 the wake vortices move further downstream of the body in the form of alternative vortex shedding called a Von Kármán vortex street (the phenomenon is discussed in more detail in the next chapter). For Re<100 the flow is laminar, and the vortices dissipate due to viscous diffusion. [27]

At area B the drag coefficient drops due to the separation of these vortices from the body. The point of separation „S“ with (Figure 2.2-2a) increasing Reynolds number moves against the direction of the flow. For Re=500 vortices behave turbulently. [27]

Area C is the interval for a moderate increase in drag coefficient which can be explained by the increase of vortices after the cylinder. On the frontal area is the laminar boundary layer which ends at the point of separation „S“. The Kármán vortex street is still observable. [27]

The value of the drag coefficient is practically constant for area D. The laminar boundary layer at point „T“ transforms into turbulent, while with increased Reynolds number the point of transition „T“ is approaching the point of separation „S“ (Figure 2.2-2b). [27]

At area E for $Re=Re_{cr}=5.10^5$ point of transition „T“ reaches the point of separation „S“ (Figure 2.2-2c). As we discussed before the turbulent boundary layer extends farther along the surface, leading to a narrower wake. This narrower downstream wake results in a reduced area of low pressure on the downstream side, thereby contributing to lower drag. [27][30]

For area F a non-stationary transition from laminar- to turbulent boundary layer occurs. [27]

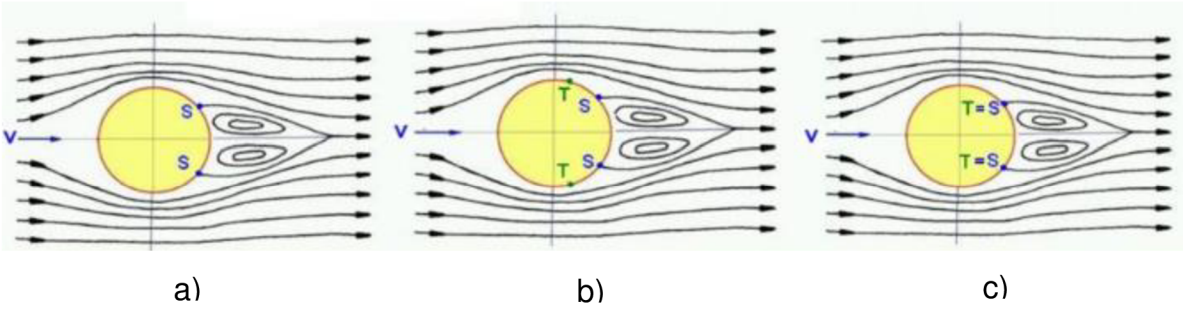

Figure 2.2-2 *Stages of boundary layer separation in a variation of different Reynolds number scenarios adapted from [27], modified:* ***a)*** *point of separation „S“.,* ***b)*** *point of separation „S“. and point of transition„T“,* ***c)*** *aligning of „T“.„S“,*

2.3 KÁRMÁN VORTEX STREET

If a bluff body is placed into a flowing fluid - under certain conditions - it undergoes vortex shedding, forming a regular pattern of alternating vortices called Kármán vortex street (Figure 2.3-1), which leads to periodic boundary layer separation with frequency f [27][33]. As the flow velocity rises, the frequency of vortex formation also increases, demonstrating a direct correlation between the two variables. This empirical relationship was discovered by Czech physicist Vincenc Strouhal in 1878 [34]. Strouhal defined a formula for a dimensionless constant called as Strouhal number, to characterize oscillatory flows:

$$St = \frac{f D_{ch}}{v} \tag{2.3.1}$$

Where f is the frequency of vortex shedding
D_{ch} is the characteristic length of the bluff body
v is the velocity of the flow

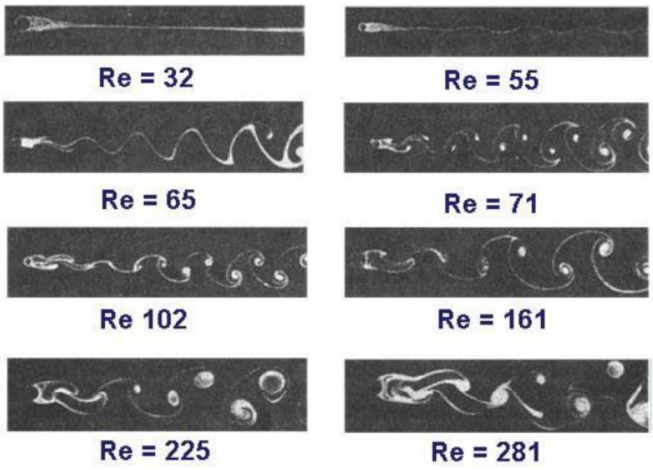

Figure 2.3-1 *Kármán vortex street around a circular cylinder based on the value of Reynolds number, adapted from [27]*

The Strouhal number has great use in the prediction of oscillatory behaviors [35]. It emerges as a function of the Reynolds number (Figure 2.3-2) and it closely approximates 0.2 across a wide range of Reynolds numbers [34]. Strouhal number is influenced by the shape of the body placed in the flow, in general, bluff bodies have a higher value of Strouhal number than streamlined bodies.

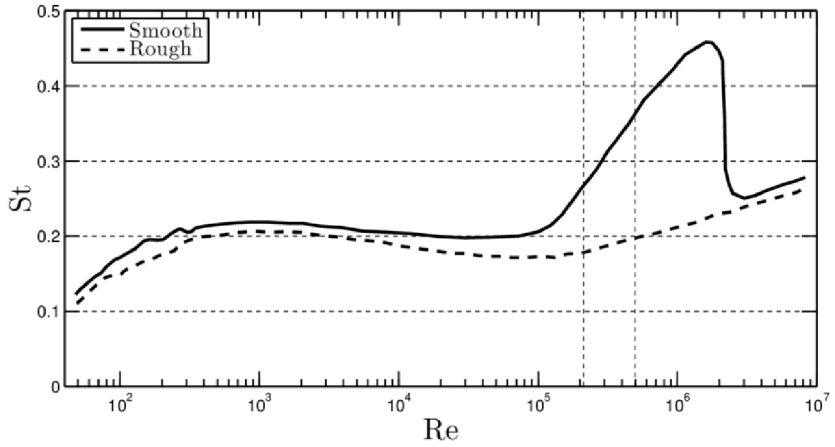

Figure 2.3-2 *Variation in the Strouhal number with various Reynolds numbers for circular cylinder, adapted from [36]*

If the natural vibration frequency of the body f_w is defined as:

$$f_w = \frac{1}{2\pi}\sqrt{\frac{k_b}{m}} \tag{2.3.2}$$

Where k_b is the stiffness of the body
m is the mass of the body

Then it is necessary to ensure, that the natural vibration frequency differs from the frequency of the vortex shedding, otherwise, it would cause resonance which could lead to oscillation or even flutter. This is a requirement while designing structures such as towers, chimneys, skyscrapers, etc. [27]

3 VIVACE CONVERTER

The VIVACE converter is composed of a rigid and elastically mounted bluff body, placed in fluid flow. The cylinder undergoes Vortex-Induced Vibrations (VIV) which cause the body to oscillate in the vertical direction and transmit the kinetic energy through a transmission system – which can be found in the supporting piles - to a generator for conversion to electricity. [24]

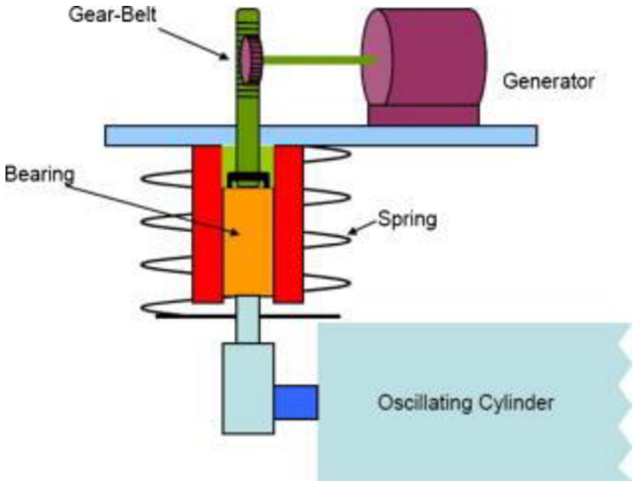

Figure 3-1 *Parts of VIVACE converter [24]*

3.1 LAB MODEL

The place to be selected for the VIVACE converter to be tested first was The University of Michigan LTFSW Channel. Two compression coil springs are attached to the end plates of the aluminum-made cylinder, suspending it. The body is constrained to vibrate freely in a vertical direction by linear bearings. A low-RPM, rotary generator is used to convert the vibrations into electricity. To transmit the linear oscillatory motion to rotational oscillatory motion a gear-belt transmission system is needed. The parameters of the VIVACE system to be tested are shown in Table 3.1-1 [37]

Table 3.1-1 *Parameters of the VIVACE converter*

Diameter	[mm]	127
Length	[mm]	914,4
K_{spring} of each spring	[N/m]	518
Mass of the system	[kg]	16,8
Mass ratio	[-]	1,45
$f_{n,\ water}$	[Hz]	0,96
Velocity of current	[m/s]	0,4-1,2
Reynolds number	[-]	$0{,}44\text{-}1{,}34 \times 10^5$
Generator resistance	[Ohm]	7

The goal of the test was to confirm the remaining nonlinear resonance through different velocity ranges without having to adjust the spring stiffness. The results showed that the amplitude of VIV is highly impacted by the Reynolds number. [24]

3.2 MATHEMATICAL MODEL

The functioning of VIVACE can be presented mathematically by a system of dynamics and fluid forces. To describe the motion of the cylinder in the vertical (y) direction we can use Lagrange's equations of the second kind to define the governing equation of the vibration as the following [37]:

$$m_{osc}\ddot{y} + c_{total}\dot{y} + k_{spring}y = F_{fluid}\hat{y} \tag{3.2.1}$$

Where m_{osc} is the mass of the oscillating system (in this model including a third of the spring-mass)
c_{total} is the total damping coefficient
k_{spring} is the spring stiffness
F_{fluid} is the force exerted by the fluid (in this model is separated into viscous and inviscid components meaning $F_{fluid} = F_{viscous} + F_{inviscid}$)
$\hat{y}$ is the unit normal vector in the y-direction

The inviscid force (3.2.2) can be defined as a function of the inviscid added mass m_a which is the given impulse to the fluid during an incremental change of body velocity divided by that incremental velocity. By introducing the mass of displaced fluid $m_d = \frac{\pi}{4}\rho_w D^2 L$ the equation of the viscous force (3.2.3) can be reduced as follows [37]:

$$F_{inviscid}\hat{y} = -m_a\ddot{y} \tag{3.2.2}$$

$$F_{viscous}\hat{y} = \frac{1}{2}c_y(t)\rho_w v^2 DL = c_y(t)m_d v^2 \frac{2}{\pi D} \tag{3.2.3}$$

Where $c_y(t)$ is the fluctuating transverse force coefficient
ρ_w is the density of the fluid
v is the velocity of the flow

Substitution of equations (3.2.2) and (3.2.3) leads to the final form of the equation of motion (3.2.4):

$$(m_{osc} + m_a)\ddot{y} + c_{total}\dot{y} + k_{spring}y = \frac{2}{\pi D}c_y(t)m_d v^2 \tag{3.2.4}$$

When the VIVACE is in resonance, an almost sinusoidal motion appears on the cylinder which allows to application of the linear oscillator model on the vortex-induced vibrations, otherwise, the model has to be nonlinear. To approximate the resonant behavior of the system without experiment, a sinusoidal form of the fluctuating transverse force coefficient and amplitude needs to be assumed as [37]:

$$y = y_{max}\sin\left(2\pi f_{fluid}t\right) \tag{3.2.5}$$

$$c_y = C_y\sin\left(2\pi f_{fluid}t + \phi\right) \tag{3.2.6}$$

Where f_{fluid} is the dominant fluid forcing frequency, which is assumed to be equal to f_{osc}, which defines that the system is in resonance

ϕ is the phase difference between the fluid forcing and the displacement, which is near $\frac{\pi}{2}$ for linear systems at resonance.

3.3 POWER AND EFFICIENCY OF THE SYSTEM

The fluid power of the system averaged over one cycle period can be calculated as: [37]

$$P_{VIVACE-fluid} = \frac{W_{VIVACE-fluid}}{T_{osc}} \tag{3.3.1}$$

Work generally can be defined as displacement caused by force acting on the object. This theory can be applied also in this case as the fluid force causes displacement of the cylinder. With this knowledge, the work done on the body during one vibration cycle is:

$$W_{VIVACE-fluid} = \int_{y_0}^{y_1} F_{fluid} dy = \int_0^{T_{osc}} F_{fluid}\, \dot{y} dt \tag{3.3.2}$$

In synchronization - as it was discussed - $f_{fluid} = f_{osc} = \frac{1}{T_{osc}}$. Substitution of the right hand side of (3.2.4) and the derived form of (3.2.5) to (3.3.2) and after to (3.3.1) leads to the following equation:

$$P_{VIVACE-fluid} = \frac{1}{2}\rho\pi C_y v^2 f_{osc} y_{max} DL \sin(\phi) \tag{3.3.3}$$

Where ϕ is the phase angle between the fluid force and the body displacement

The actual energy harnessed from a VIVACE system can be determined only by lab tests, but an upper limit is calculatable by dividing the fluid power in VIVACE by the power in fluid – which can be calculated as follows. The dynamic pressure based on the „pressure“ form of Bernoulli equation is:

$$p_{dynamic} = \frac{1}{2}\rho v^2 \tag{3.3.4}$$

Pressure is defined as the force acting on a projected area which is in our case DL. Based on this the acting force can be calculated as:

$$F_{kinetic} = \frac{1}{2}\rho v^2 DL \tag{3.3.5}$$

Using the general equation of work, the power in the fluid can be defined as:

$$P_{fluid} = \frac{1}{2}\rho v^3 DL \tag{3.3.6}$$

Equations (3.3.3.) and (3.3.6.) lead to the upper limit of the energy that could be harnessed from the VIVACE system, formulating the following formula:

$$\eta_{UL} = \frac{P_{VIVACE-fluid}}{P_{fluid}} = \frac{\frac{1}{2}\rho\pi C_y v^2 f_{osc} y_{max} DL \sin(\phi)}{\frac{1}{2}\rho v^3 DL} \tag{3.3.7}$$

4 CFD ANALYSIS OF VORTEX INDUCED VIBRATIONS

In the practical part of this thesis, a 2D CFD analysis of vortex-shedding around a bluff body with different cross sections with zero degrees of freedom will be discussed. Five different shapes were chosen to be investigated: triangle (one corner facing against the flow), ellipse, circle, rectangle, and square. Lift force, drag force, velocity, static pressure, Strouhal number and frequency were examined for each of the profiles without considering the spring or the body's mass, i.e. the body was firmly fixed and no motion was allowed. The cross-sections were analyzed for 6 different velocity boundary conditions in a range of $v = 0{,}1 - 0{,}6$ ms^{-1}. The results for each shape will be compared and evaluated based on these parameters. It‘s important to state, that this analysis is significantly simplified, and the results may not align with reality.

4.1 GOVERNING EQUATIONS FOR CFD

Governing equations of CFD represent mathematical interpretations of the conservation laws of physics, respecting the following laws [38]:

- Conservation of mass – Mass can neither be created nor destroyed.
- Conservation of momentum -The sum of forces exerted on the fluid is equal to the rate of change of momentum.
- Conservation of energy – Energy can’t be created nor destroyed.

Based on these laws can be formulated equation of continuity, the Navier-Stokes equation, and equations describing heat transfer in a flowing liquid [33]. With the introduction of general variable, all the flow equations in the conservative incompressible form can be formulated using the following relation:

$$\frac{\partial \phi}{\partial t} + \frac{\partial (u\phi)}{\partial x} + \frac{\partial (v\phi)}{\partial y} + \frac{\partial (w\phi)}{\partial z} = \frac{\partial}{\partial x}\left[\Gamma \frac{\partial \phi}{\partial x}\right] + \frac{\partial}{\partial y}\left[\Gamma \frac{\partial \phi}{\partial y}\right] + \frac{\partial}{\partial z}\left[\Gamma \frac{\partial \phi}{\partial z}\right] + S_\phi \qquad (4.1.1)$$

This formula is the transport equation for the property ϕ, illustrating the occurring transport processes in a fluid flow. The left side of the relation stands for the local acceleration and advection terms which correspond to the diffusion term (diffusion coefficient Γ) and the source term (S_ϕ) found on the right side. The flow equations are reached by substitutions listed in Table 4.1-1 to the previously mentioned terms.

Table 4.1-1 *Substitutions to the general form of governing equations for incompressible flow*

	ϕ	Γ	S_ϕ
Continuity equation	1	0	0
Navier-Stokes equations			
x-Momentum	u	$\nu + \nu_T$	$-\frac{1}{\rho}\frac{\partial p}{\partial x} + S_u^I$
y-Momentum	v	$\nu + \nu_T$	$-\frac{1}{\rho}\frac{\partial p}{\partial y} + S_v^I$

z-Momentum	w	$\nu + \nu_T$	$-\frac{1}{\rho}\frac{\partial p}{\partial z} + S_w^I$
Energy equation	T	$\frac{\nu}{Pr} + \frac{\nu_T}{Pr_T}$	S_T

Where u, v, w is the velocity of the flow in each coordinates
ν is the kinematic viscosity
ν_T is the turbulent kinematic viscosity
S_u^I, S_v^I, S_w^I is the source term from momentum equations including the pressure and non-pressure gradient terms and different additional sources
S_T is the source term of energy equations comprising heat sources within the flow field
Pr is the Prandtl number

For laminar flow, the turbulent kinematic viscosity is zero, while for turbulent flow the value depends on the simulation model. The most popular viscous models are k-ε and k-ω where both ε and ω represent the dissipation of turbulent kinetic energy [39]. The biggest difference between them is that the standard k-ω model shows more accuracy while modeling near-wall interactions than the simple k-ε, which is typically used to model external flows with complex geometry [40]. Table 4.1-2 shows the formulations of turbulence model equations for compressible flow and the strength of each model

Table 4.1-2 *Navier -Stokes equations for "k-ω" and "k-ε" turbulent models, adapted from [41]*

$k-\omega$	$\frac{\partial(\rho k)}{\partial t} + \frac{\partial(\rho k u)}{\partial x} + \frac{\partial(\rho k v)}{\partial y} = P_k + \frac{\partial}{\partial x}\left((\mu + \sigma^* \mu_T)\frac{\partial k}{\partial x}\right) + \frac{\partial}{\partial y}\left((\mu + \sigma^* \mu_T)\frac{\partial k}{\partial y}\right) - \beta^* \rho k \omega$	(4.1.2)
	$\frac{\partial(\rho \omega)}{\partial t} + \frac{\partial(\rho \omega u)}{\partial x} + \frac{\partial(\rho \omega v)}{\partial y} = \alpha \frac{\omega}{k} P_k + \frac{\partial}{\partial x}\left((\mu + \sigma \mu_T)\frac{\partial \omega}{\partial x}\right) + \frac{\partial}{\partial y}\left((\mu + \sigma \mu_T)\frac{\partial \omega}{\partial y}\right) - \beta \rho \omega^2$	(4.1.3)
	$\mu_T = \frac{\rho k}{\omega}$	(4.1.4)
	Good accuracy in near-wall boundary layer region	
$k-\varepsilon$	$\frac{\partial(\rho k)}{\partial t} + \frac{\partial(\rho k u)}{\partial x} + \frac{\partial(\rho k v)}{\partial y} = P_k + \frac{\partial}{\partial x}\left((\mu + \sigma^* \mu_T)\frac{\partial k}{\partial x}\right) + \frac{\partial}{\partial y}\left((\mu + \sigma^* \mu_T)\frac{\partial k}{\partial y}\right) - \beta^* \rho \varepsilon$	(4.1.5)
	$\frac{\partial(\rho \varepsilon)}{\partial t} + \frac{\partial(\rho \varepsilon u)}{\partial x} + \frac{\partial(\rho \varepsilon v)}{\partial y} = C_1 \frac{\varepsilon}{k} P_k + \frac{\partial}{\partial x}\left((\mu + \sigma \mu_T)\frac{\partial \varepsilon}{\partial x}\right) + \frac{\partial}{\partial y}\left((\mu + \sigma \mu_T)\frac{\partial \varepsilon}{\partial y}\right) - C_2 \rho \frac{\varepsilon^2}{k}$	(4.1.6)
	$\mu_T = C_\mu \frac{\rho k^2}{\varepsilon}$	(4.1.7)
	Good results for free-shear region	

Where ρ is the density of the fluid
k is the kinetic turbulent energy
ω is the specific dissipation
ε is the dissipation of turbulent energy

P_k is the production of turbulent kinetic energy due to mean velocity shear
μ is the molecular viscosity
μ_T is the turbulent viscosity
$\alpha, \beta, \beta^*, \sigma^*, \sigma, C_1, C_2$ are constants
C_μ is the turbulence model constant

The importance of choosing the right turbulence model for specific flow features is undeniable. This decision affects the accuracy of the results, the computational time, and the costs of the simulation.

4.2 GEOMETRY

The geometry of the bluff bodies was transformed into 2D to simplify the simulations. Geometries were made in Ansys SpaceClaim. The disadvantage of this software is that the user needs to be consistent during the design process because the program does not leave much space for further modifications of the design. Dimensions of the cross sections were chosen so the characteristic length of the profiles was 100 mm, which is for the circle its diameter, for the square and triangle its sides, for the rectangle its longer side, and for the ellipse its semi-major axis. For structured mesh, it was needed to split the domain considering which parts of the domain needed to be more precisely meshed. It was decided to use more refined mesh around and right behind the shape, based on this preference was the domain sliced up. To get more accurate results area around the profile was chosen to follow the main shape of the body. Dimensions of the profiles and the domain are shown in Figure 4.2-1.

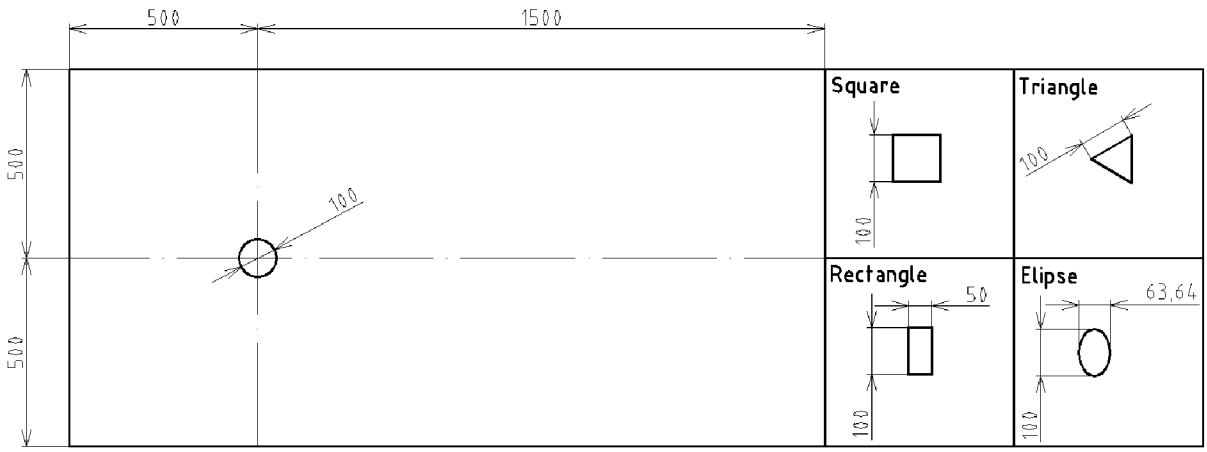

Figure 4.2-1 *Dimensions of each geometry and domain*

4.3 GRID GENERATION AND WALL FUNCTIONS

In CFD the meshing process is essential to be considered carefully to ensure the accuracy of the simulation results. In this case, a structured mesh appeared to be the best option due to its stability, simplicity, efficient memory usage, and lower simulation time. It was chosen to use quadrilateral elements for every area of the domain which allowed for adhered refinement of the above-mentioned areas.

When creating a mesh certain values need to be investigated to decide if the grid is proper for simulation. One of these values is the characteristic wall coordinated, so-called y+ which is the function of the Reynolds number. When the Reynolds number is high, the viscous sublayer of a boundary layer becomes so thin that effectively resolving it with an adequate number of grid points becomes challenging [42]. The universal law of the wall, on which wall functions are based, essentially suggests that the velocity distribution near a wall remains similar across nearly all turbulent flows[43]. This dimensionless wall distance can be calculated as:

$$y^+ = \frac{y_w v_\tau}{\upsilon} \tag{4.3.1}$$

Where y_w is the absolute distance from the wall
v_τ is friction velocity
υ is kinematic viscosity

By knowing that the value of y+ must be around 1, using this formula the requested distance between the first mesh layer and the wall can be calculated from equation (4.3.1) by defining the following formulas:

$$v_\tau = \sqrt{\frac{\tau_w}{\rho}} \tag{4.3.2}$$

Where τ_w is the wall shear stress, which can be defined as:

$$\tau_w = \frac{1}{2} C_f \rho v_\infty^2 \tag{4.3.3}$$

Where v_∞ is the freestream velocity
$C_f = 0{,}0576 Re^{-\frac{1}{5}}$ is the skin friction coefficient

For each situation, the absolute distance from the wall was calculated, and based on it a structured mesh was generated, which led to a y^+=1-2 through the simulations. From equation (4.3.3) it follows, that y^+ also depends on the roughness of the wall. For the wall of the profile, a non-slip boundary condition (Figure 4.3-1) with a roughness height of 0 m and roughness constant of 0,5.

On the upper and bottom sides of the domain, where is the transition between the media (in other words free surface areas), it was assumed that no deformation of the surface would happen nor would be expected flow from the surface, the definition of a free-slip boundary condition, called as “symmetry” (Figure 4.3-1), was the best option to avoid using a multiphase model. It was also important to be defined so it wouldn’t affect in any way the flow around the shape of the cross-section.

The area behind the profile was also considered to be more refined because this area is where the Kármán vortex street formulates (Figure 4.3-1).

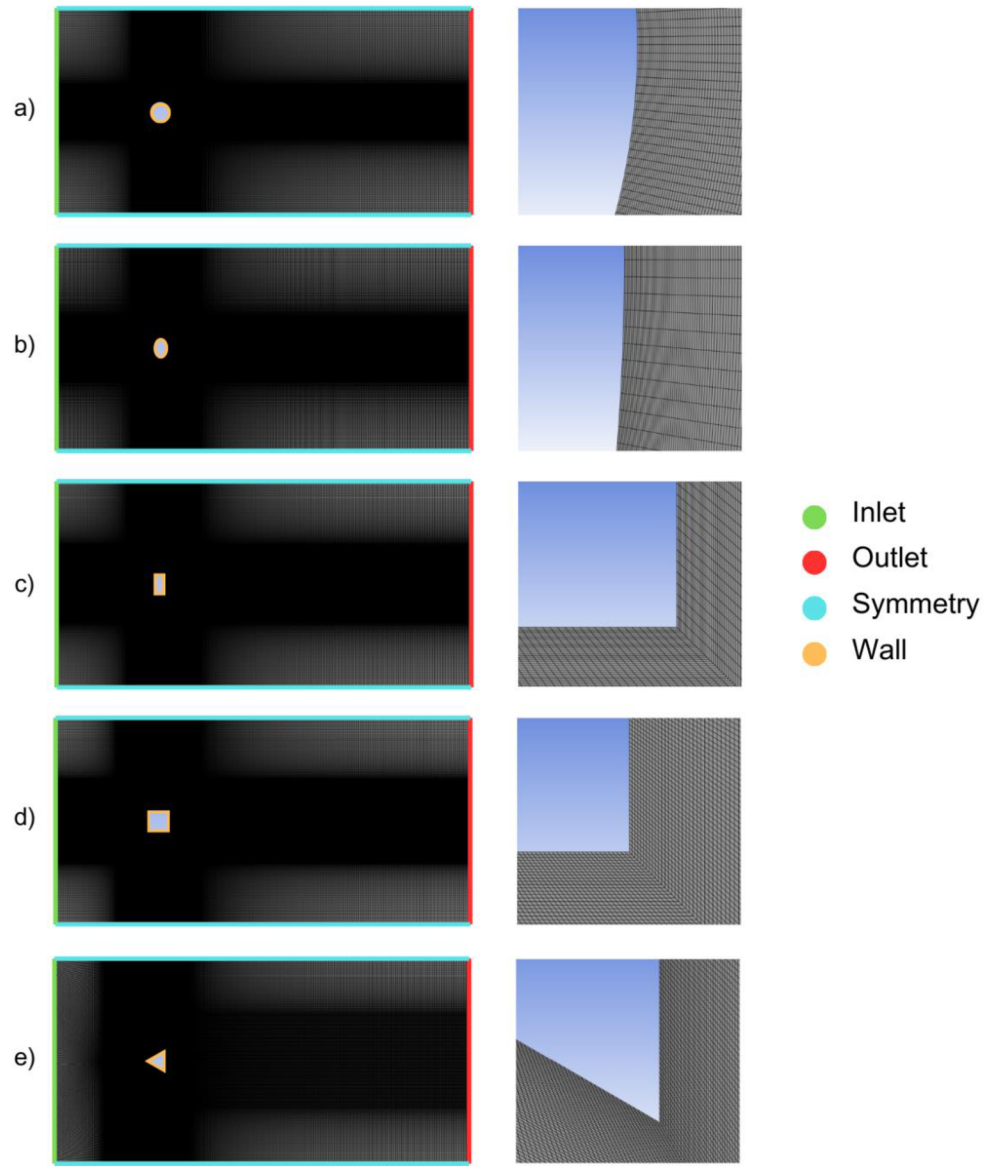

Figure 4.3-1 *Preview of the mesh and wall boundary conditions for different cross-section geometries:* ***a)*** *circle,* ***b)*** *ellipse,* ***c)*** *rectangle,* ***d)*** *square,* ***e)*** *triangle*

4.4 CALCULATION SETTINGS

As it was discussed, for the observation of vortex-induced vibrations a CFD method was chosen. To accomplish this, for all of the simulations, the student license of Ansys Fluent 2023 R2 was used. This phenomenon varies over time so the calculations were provided as transient. For accurate results, it was necessary to choose a viscous model that meets the requirements. Because a boundary layer separation was assumed to be observed, the SST (shear stress transport) k-ω seemed to be the best decision which combines the strengths of the k-ω model in near-wall sections and the great performance of the k-ε model in the free-stream areas [38]. This model calculates based on RANS equations. For Cell zone conditions was used water with its default characteristics from the database of Ansys Fluent.

The boundary conditions for different types of domain boundaries were discussed in Chapter 4.3 and shown in Figure 4.3-1. The inlet was placed on the left-hand side and

the outlet on the right-hand side of the calculation domain. The inlet flow exact values of velocity were chosen based on the velocities realizable in the lab of the Victor Kaplan Department of Fluid Engineering, varying in an interval of 0,1-0,6 ms^{-1}., defined by turbulence intensity of 5% and hydraulic diameter of 0,1 m. The outlet was defined as a pressure outlet with 0 Pa.

For the pressure-velocity coupling was chosen scheme SIMPLE. As gradient method the default setting was used, which is the least squares cell based method. The further settings of spatial discretization are shown in Table 4.4-1.

Table 4.4-1 *Settings of spatial discretization*

	Settings
Pressure	*Second order*
Momentum	*Second order upwind*
Turbulent kinetic energy	*Second order upwind*
Specific dissipation rate	*Second order upwind*
Transient formulation	*Second order implicit*

To determine the ideal time-step size a more practical approach was followed, using the defining equation of the Strouhal number (2.3.1). From this formula, the estimated frequency and the period of the oscillations can be predicted. In all of the simulations, the Strouhal number was approximated to be 0,2. Using the calculated period value the time-step size equals to $T_{osc}/100$, as shown in equation (4.4.1).

$$\Delta t = \frac{T_{osc}}{100} = \frac{1}{100.f_{osc}} = \frac{D_{ch}}{100.St.v} \tag{4.4.1}$$

5 RESULTS

In the next chapter, the results of the CFD simulations will be discussed. All analyses were carried out under the same wall boundary conditions, program settings, geometry, domain, and medium, only the time step varied and the mesh was improved for the need of y+ always being around 1 to get accurate results. The simulations were provided for each cross-section using six inlet boundary conditions. The reached results were analyzed in time intervals, where the vortex shedding was fully developed. During the investigation, all profiles were examined for lift force, drag force, oscillation frequency, pressure, and Strouhal number. To determine the frequency and the magnitude of the lift- and drag forces a Fast Fourier Transformation (later FFT) was used. In the upcoming chapters, the various chapters are discussed and the shown figures apply to inlet boundary conditions with a velocity of $v = 0{,}5\ ms^{-1}$ and for 20 seconds of flow time, results for the remaining inlet BC and for same flow time are shown in Appendix 1. The dimension of the forces is N/m („Newton per meter depth“).

5.1 CIRCULAR CYLINDER

The first cross-section to be investigated was a circular cylinder. While examining the course of the lift force after the vortex shedding fully developed (Figure 5.1-1 a)) a sinusoidal function is observable. It shows that the boundary layer separation tends to be stable and predictable. The drag force also shows periodic behavior while being in phase difference with the lift force.

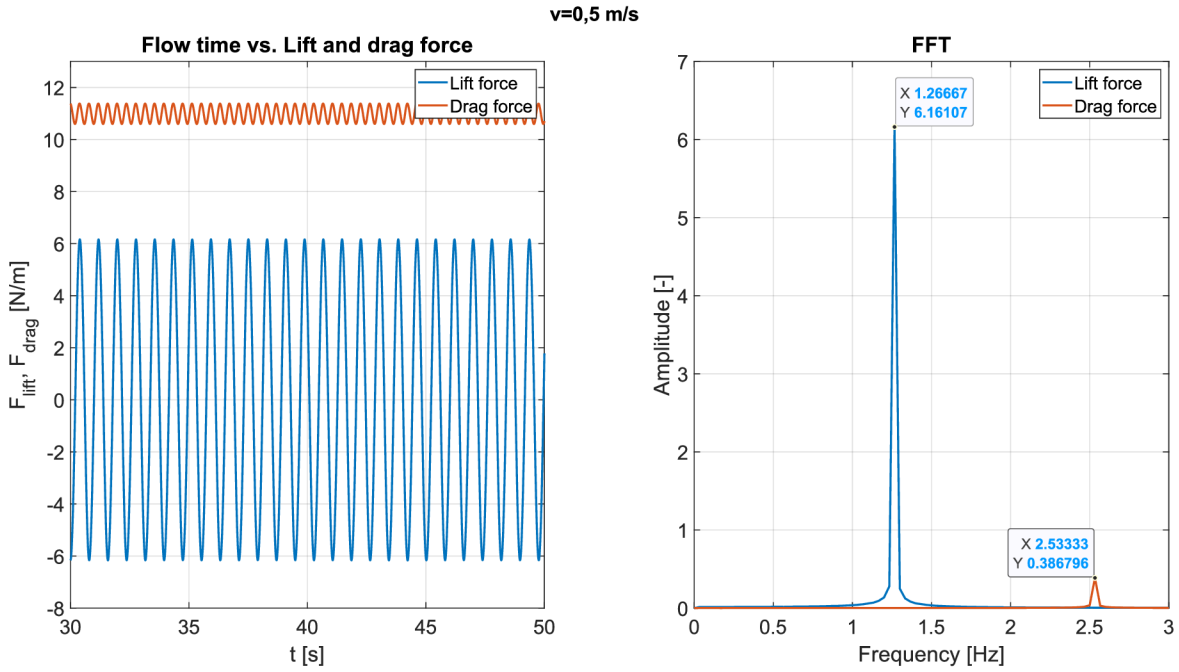

Figure 5.1-1 *The course of lift and drag forces and its FFT analysis for Re=50 000*

The FFT analysis (Figure 5.1-1) shows that the drag force has a double value of frequency than the lift force.

Moving forward with the observation of the flow around a circular cylinder, the next things to be discussed are the velocity and pressure changes through the domain. As we can see in Figure 5.1-2 a) the lowest velocity is at the area where the flow first attaches to the body and at the area right behind the profile, while in these areas, we can notice a pressure increase (Figure 5.1-2 b)). The highest velocity appears on the boundary of the boundary layer, resulting in a pressure drop. A uniform pressure distribution can be observed along the body surface which decreases the chance of instability caused by pressure differentials.

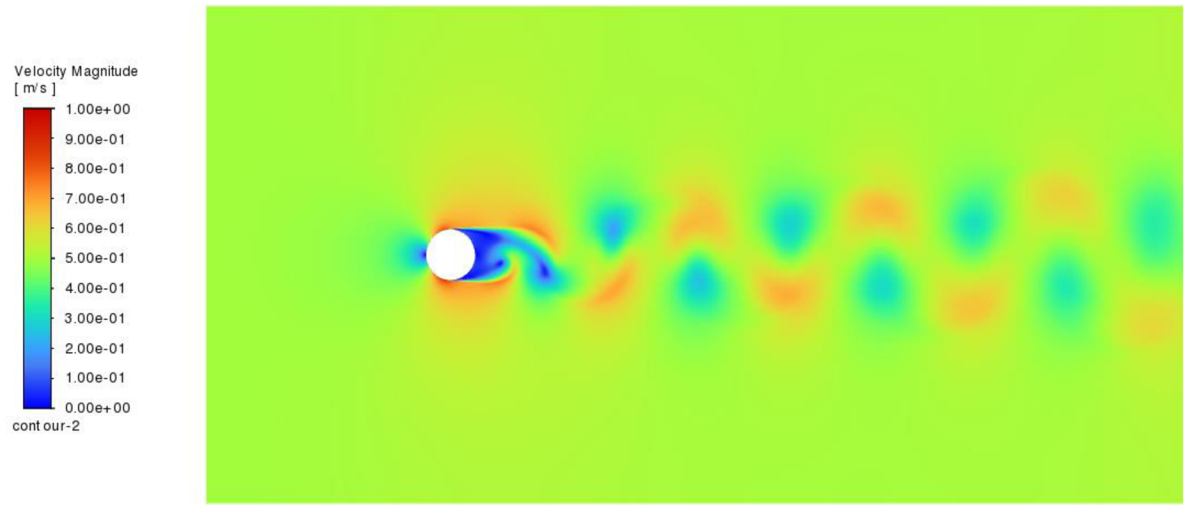

a)

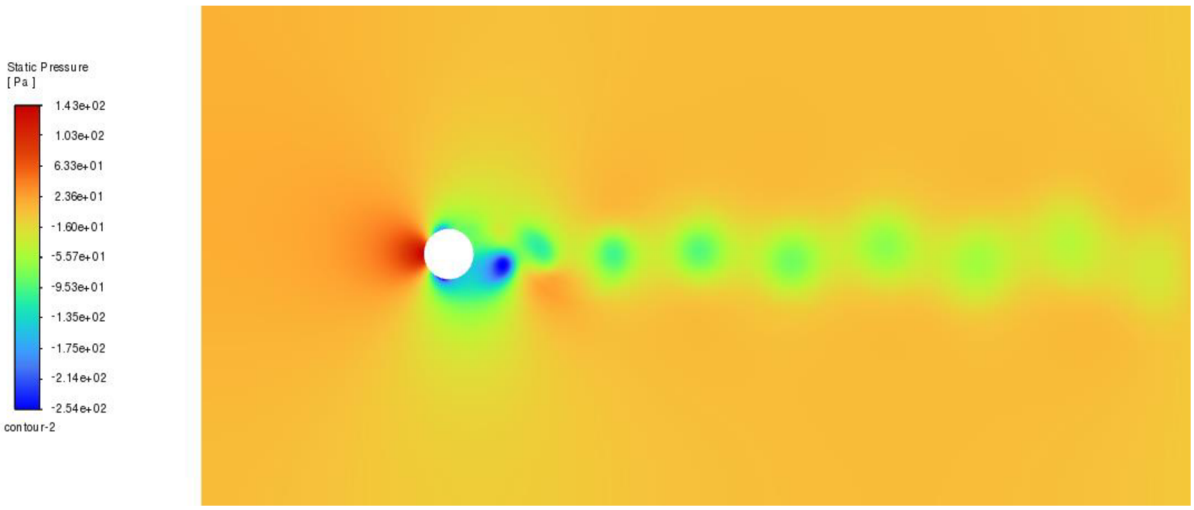

b)

Figure 5.1-2 a) *Velocity magnitude changes through the domain,* ***b)*** *Static pressure changes through the domain*

The smooth, continuous curvature of the circular cylinder leads to a consistent vortex-shedding behavior. The boundary layer separation is visible by analyzing the vorticity magnitude which describes the tendency for elements of the flow to rotate. Vorticity has non-zero values where the derivation of velocity is non-zero which is why it reaches its maximum at the boundary layer. By setting up a limit of plotting scale for the vorticity magnitude, the boundary layer can be easily differentiated visually from the freestream flow which also contributes to identifying the separation point. It's noticeable that the

separation point is close to where the vertical center line crosses the profile boundary. As mentioned in Chapter 2.1 the point of separation is not fixed on bluff bodies with rounded shapes and relies more on the Reynolds number which is visible in Figure 5.1-3 a) and Figure 5.1-3 b). It can be concluded that with the increase of the Reynolds number, the separation point moves more to the right-hand side from the vertical center line.

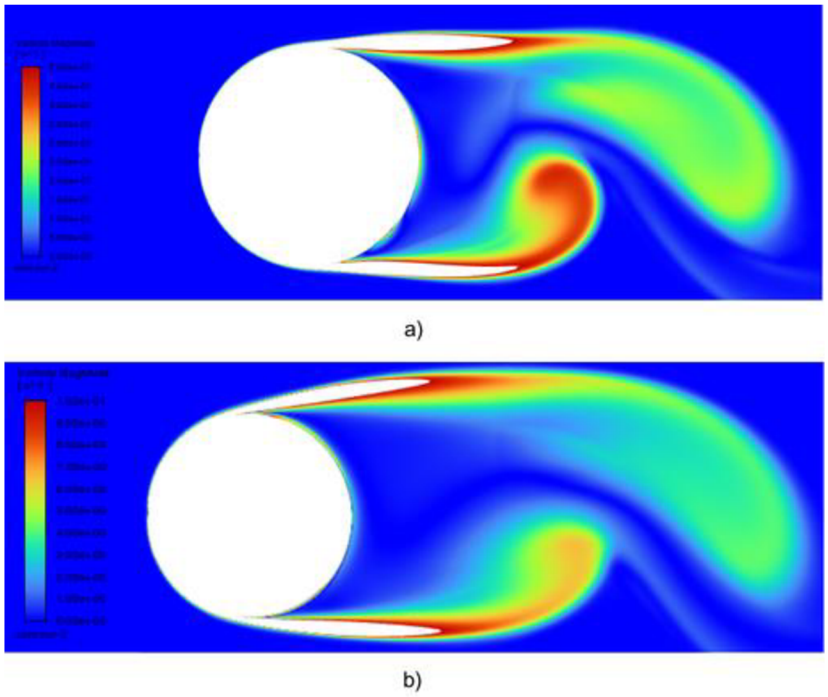

Figure 5.1-3 *Boundary layer separation shown by vorticity magnitude for:* ***a)*** *v=0,5 ms^{-1} and Re= 50 000,* ***b)*** *v=0,1 ms^{-1} and Re= 10 000*

Observing the Strouhal number (Figure 5.1-4) it slightly increases with the increment of the Reynolds number. Its value can be averaged to 0,22. The frequency of the vortex shedding also increases with velocity laying in an interval of 0,2-0,6

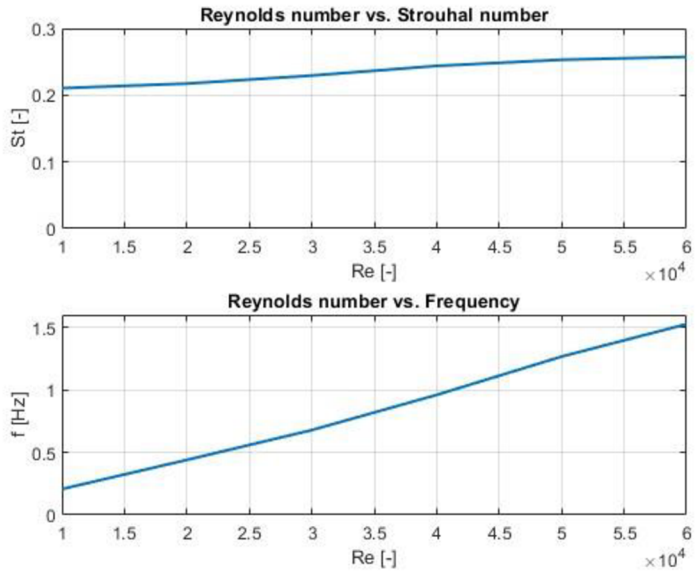

Figure 5.1-4 *Functions of Strouhal number and frequency based on the Reynolds number*

5.2 ELLIPTIC CYLINDER

Ellipse was the second profile with a rounded surface. The lift force, similarly, to the circle, shows a periodic tendency (Figure 5.2-1 a)), however, it's less stable. The period and the current amplitude vary over time. It can be concluded that where the actual period is higher, a lower force amplitude can be expected. The drag force has a less periodic behavior, but a repeating pattern is noticeable.

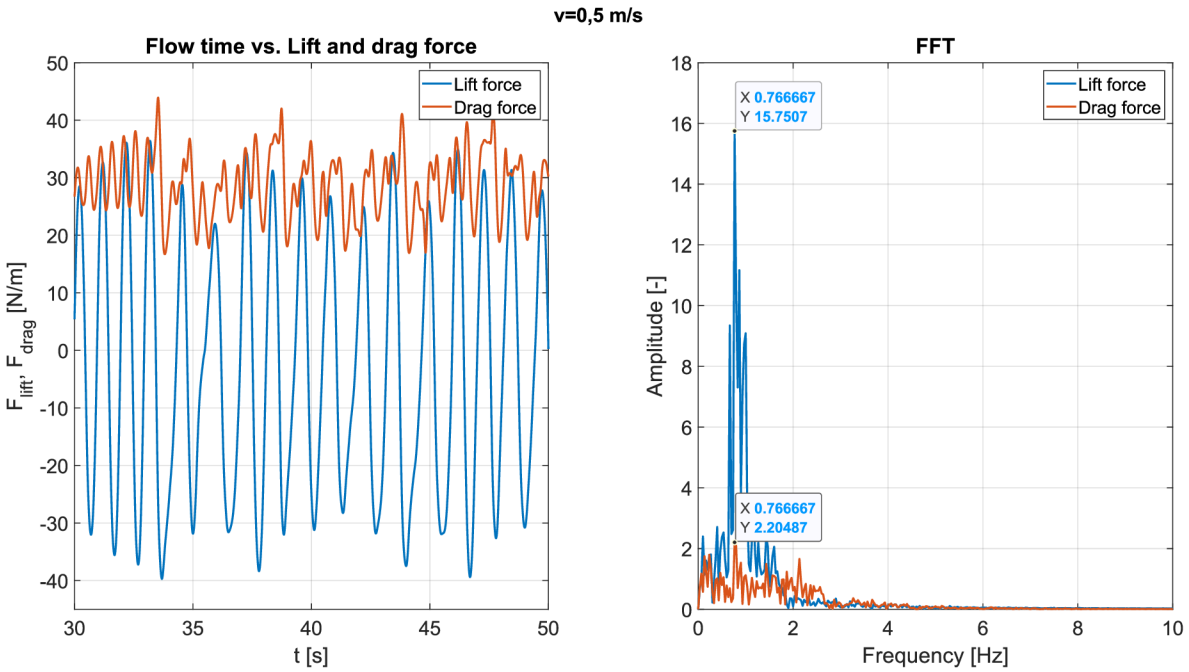

Figure 5.2-1 *The course of lift and drag forces and its FFT analysis for Re=50 000*

The FFT analysis (Figure 5.2-1 b)) shows controversial results. The frequency of the drag force is double the frequency of the lift force until it reaches Re=40 000. From that point, the frequency of the drag force varies around the value of the frequency of the lift force. It's noticeable that the FFT analysis shows multiple amplitude values, especially for the drag force. This proves what is observable in Figure 5.2-1 a), that the amplitude of the drag force changes over time.

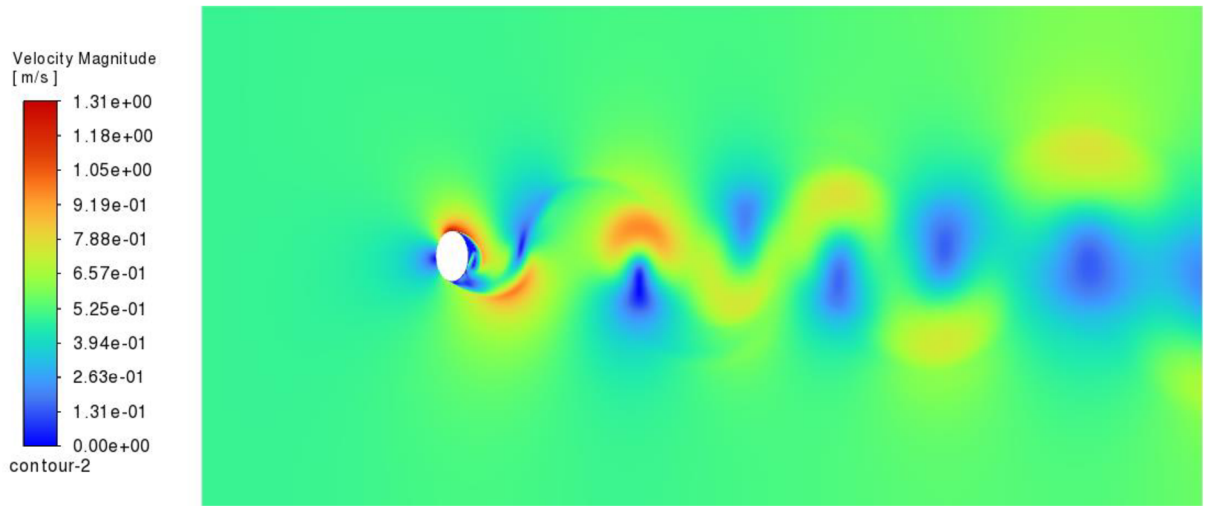

a)

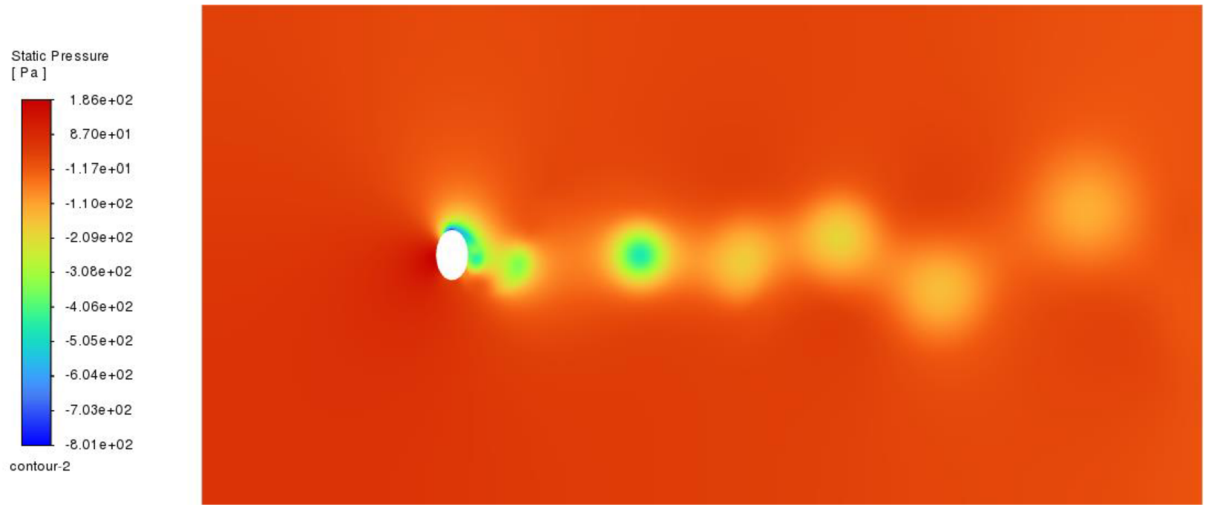

b)

Figure 5.2-2 a) *Velocity magnitude changes through the domain,* ***b)*** *Static pressure changes through the domain*

The lowest velocity appears on the part of the surface where the flow attaches to the profile and behind the body where the wake formulates (Figure 5.2-2 a)). It's visible that the pressure distribution (Figure 5.2-2 b)) around the surface is less even. The lowest pressure appears where the velocity reaches its highest value. At this stage, it's at the point where the flow detaches the body.

The boundary layer separation (Figure 5.2-3) is less consistent and predictable. The wake is less narrow than it was at the circular cylinder. The wake bubble formulates closer to the cross section which causes interaction with the body at the wake area. It's observable that a vortex bubble forms on the surface.

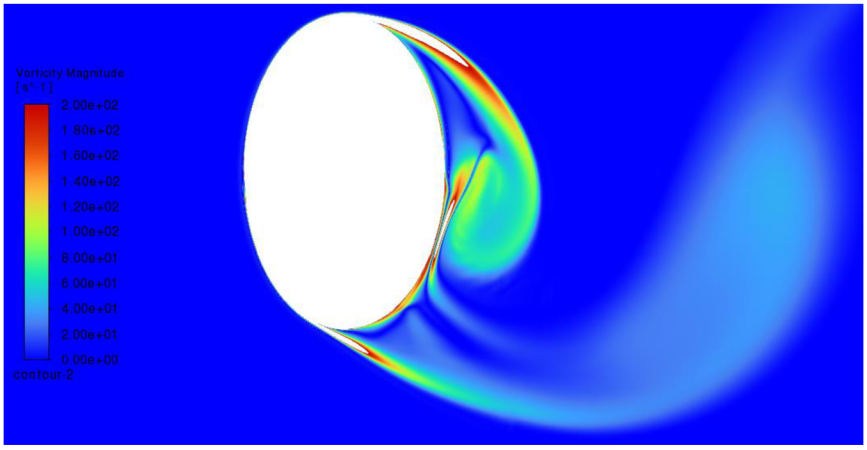

Figure 5.2-3 *Boundary layer separation shown by vorticity magnitude for Re=50 000*

Figure 5.2-4 shows the Strouhal number and the frequency as the function of the Reynolds number. The Strouhal number decreases with the increment of the Reynolds number. Despite that at Re=40 000 a slight increase is noticeable, its value is an average of 0,17. The frequency shows a growing tendency with the Reynolds number. From Re=40 000 the incline of the function decreases.

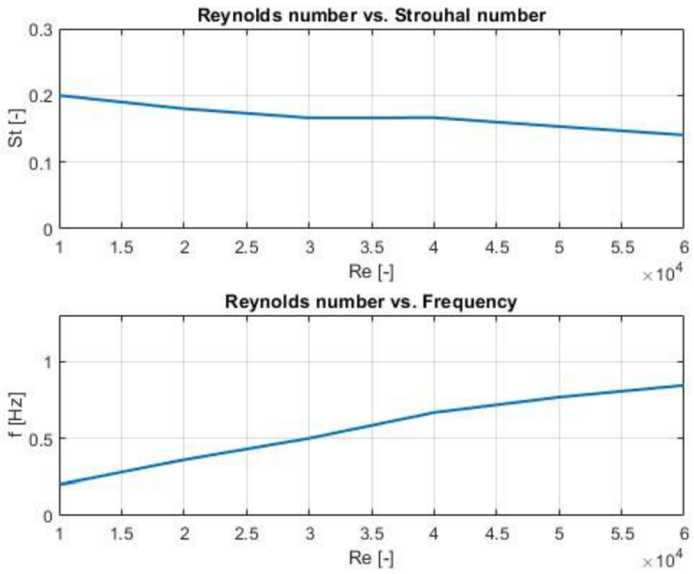

Figure 5.2-4 Functions of Strouhal number and frequency based on the Reynolds number

5.3 SQUARE SHAPED CYLINDER

Moving forward to the sharp-edged shapes, the first analyzed cross-section was the square. The course of both lift and drag forces shows a periodic pattern, although the secondary amplitude varies (Figure 5.3-1). The FFT analysis shows some differences from the previous rounded-shape graphs. Both drag and lift forces have multiple significant frequencies and their values are identical (Figure 5.3-1).

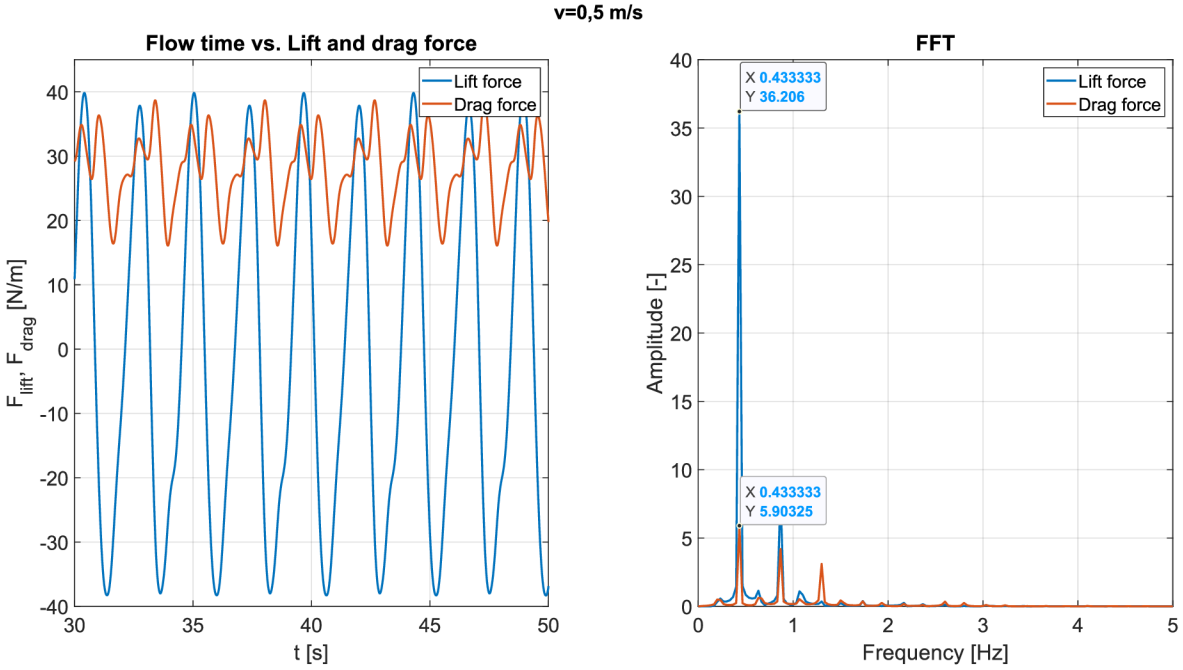

Figure 5.3-1 The course of lift and drag forces and its FFT analysis for Re=50 000

Flow separation in contrast to the rounded bodies is more abrupt (Figure 5.3-2 a)). The shedding pattern is more asymmetric and the formulated vortices are irregular and vary

in size. The highest velocity appears on the boundary of the separation layer. The lowest value is at the area near the stagnation point, where the static pressure reaches its minimum (Figure 5.3-2 b)). Following the separation zone, pressure is gradually reestablished as the flow reattaches to the surface and the wake undergoes dissipation. Nonetheless, the pressure distribution within the wake may continue to fluctuate due to the persistence of shed vortices.

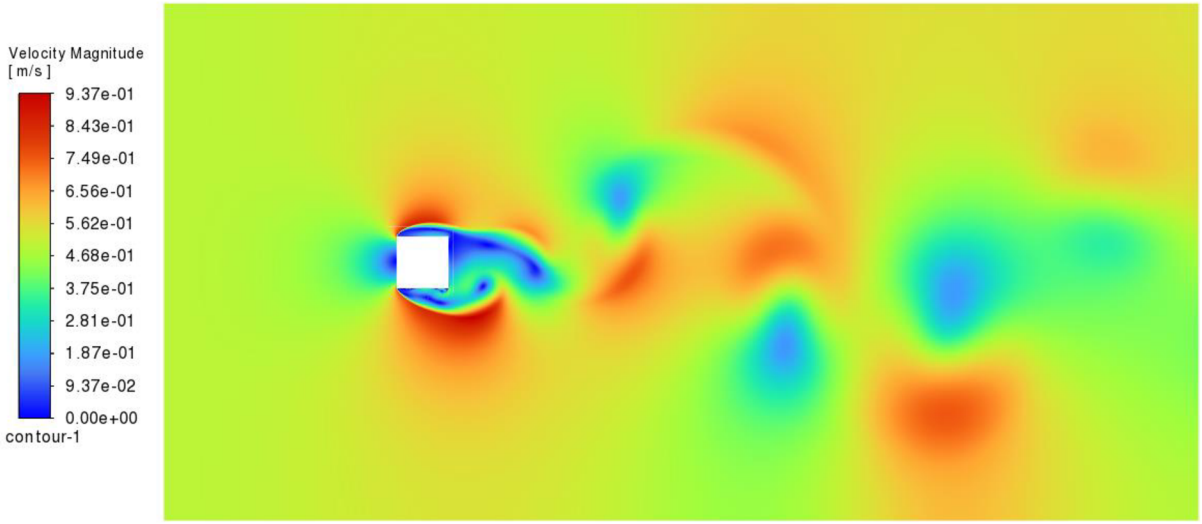

a)

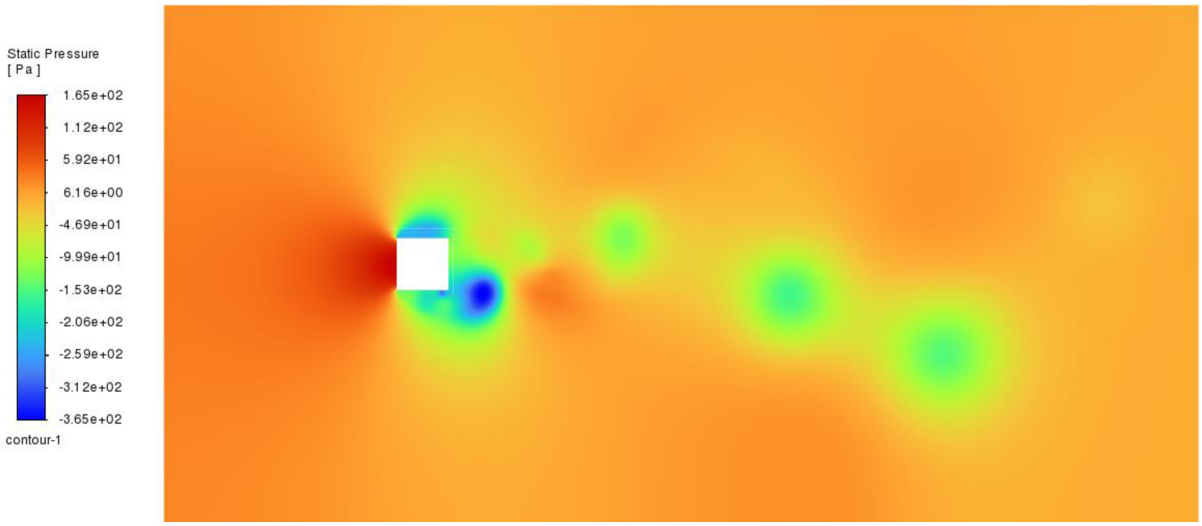

b)

Figure 5.3-2 a) *Velocity magnitude changes through the domain,* ***b)*** *Static pressure changes through the domain*

Boundary layer separation occurs prominently at the sharp corners of the profile (Figure 5.3-3). This separation phenomenon is characterized by a precise and stationary separation point, which remains consistent regardless of flow conditions. Due to the subsequent flow reattachment process, multiple separation points can be observed. Notably, on the surface and the right-hand corner, distinct instances of separation and reattachment occur. A notable and substantial vortex emerges at this specific corner, contributing to the overall flow dynamics.

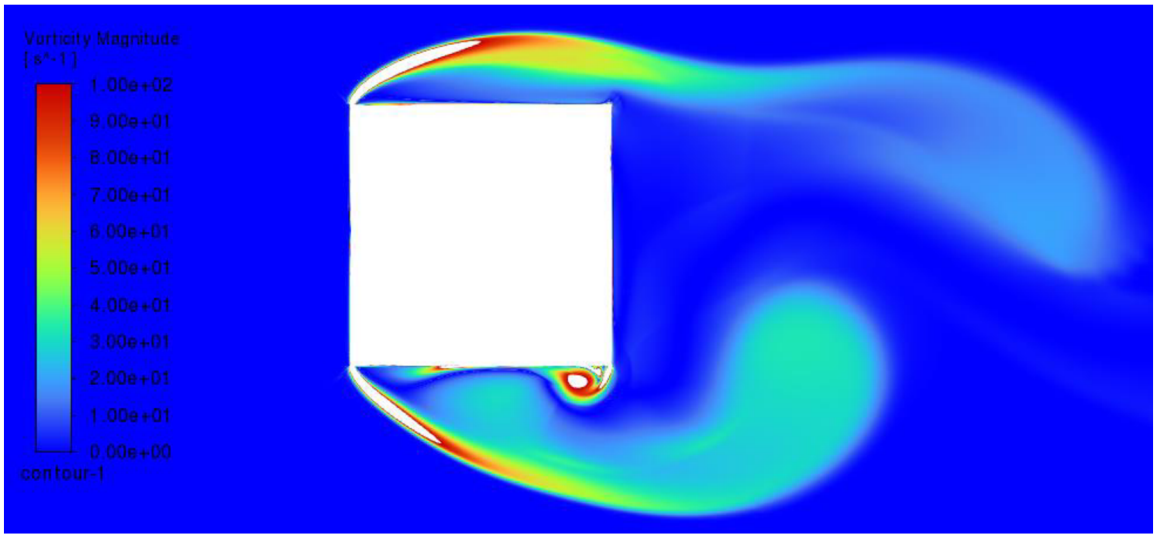

Figure 5.3-3 *Boundary layer separation shown by vorticity magnitude for Re=50 000*

The Strouhal number shows lower variations with growing Reynolds number than the circular or the elliptic cylinder did (Figure 5.3-4). The frequency shows an increasing tendency with a higher value of Reynolds number (Figure 5.3-4).

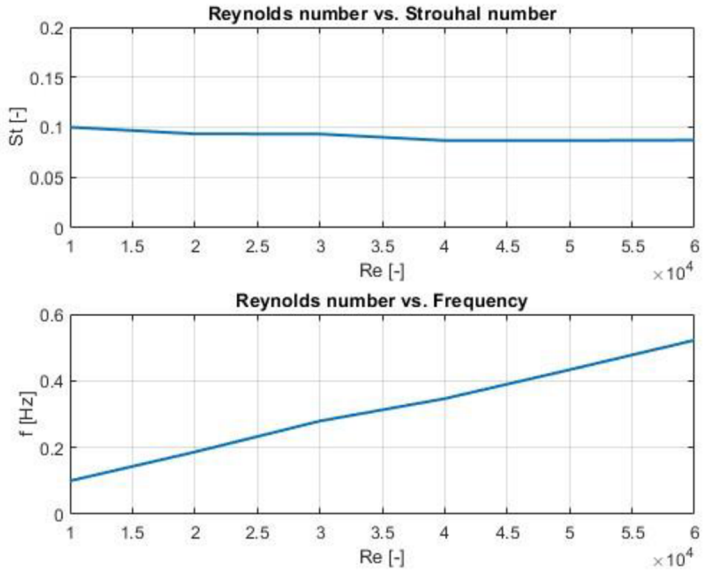

Figure 5.3-4 *Functions of Strouhal number and frequency based on the Reynolds number*

5.4 RECTANGULAR CYLINDER

The rectangle is the second observed body with sharp edges. Although the lift force (Figure 5.4-1) is alternating, it shows some irregularities and asymmetric patterns. The drag force (Figure 5.4-1) isn't in phase with the lift force and disturbance in the course is noticeable.

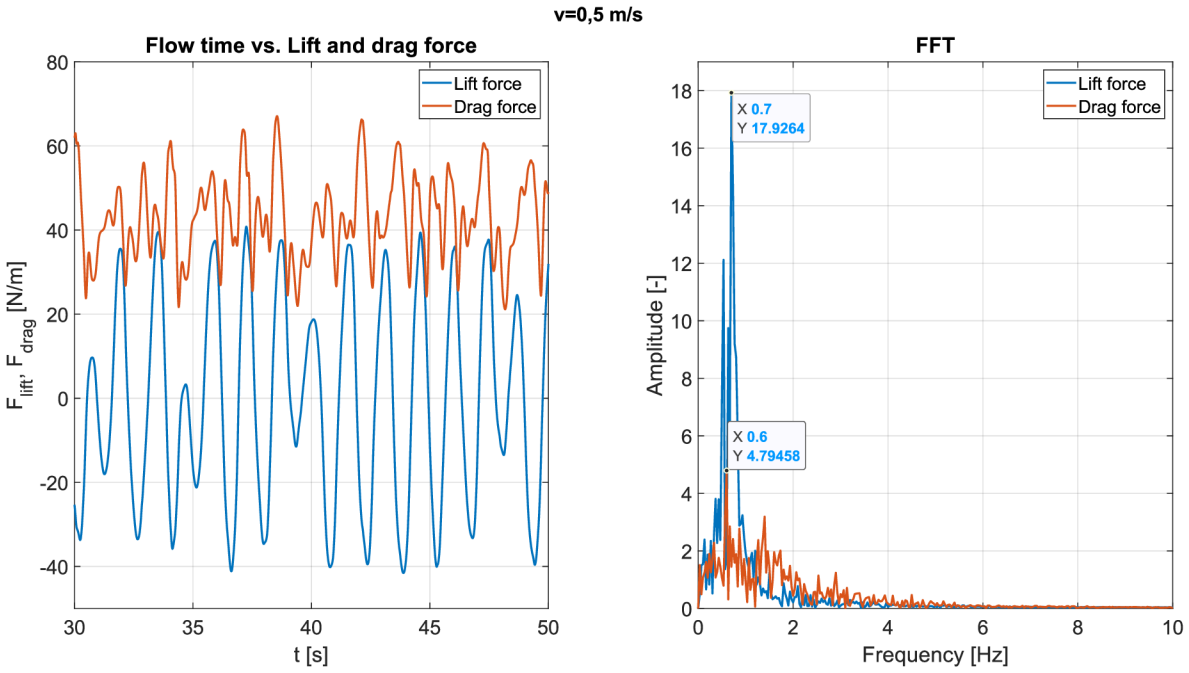

Figure 5.4-1 *The course of lift and drag forces and its FFT analysis for Re=50 000*

Both lift and drag forces oscillate on multiple frequencies (Figure 5.4-1 b)). Two significant maximal values appear in the FFT of the drag force. The one with the lower frequency (0.6 Hz) shows the highest value of the amplitude which pairs with a frequency lower than the frequency of the lift force. The lower amplitude appears with a frequency double the frequency of the lift force which phenomenon was typical at the circular cylinder.

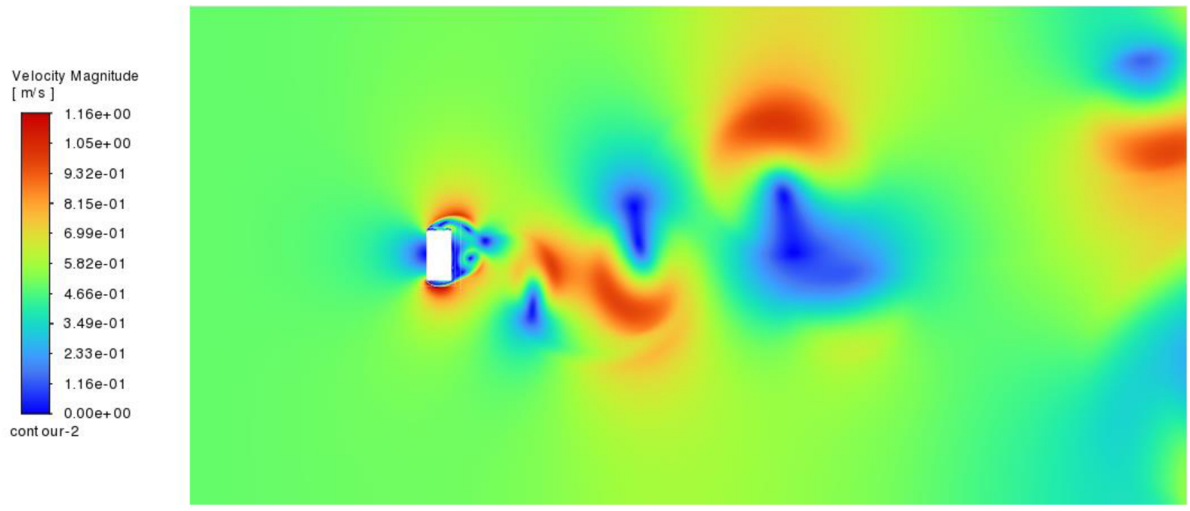

a)

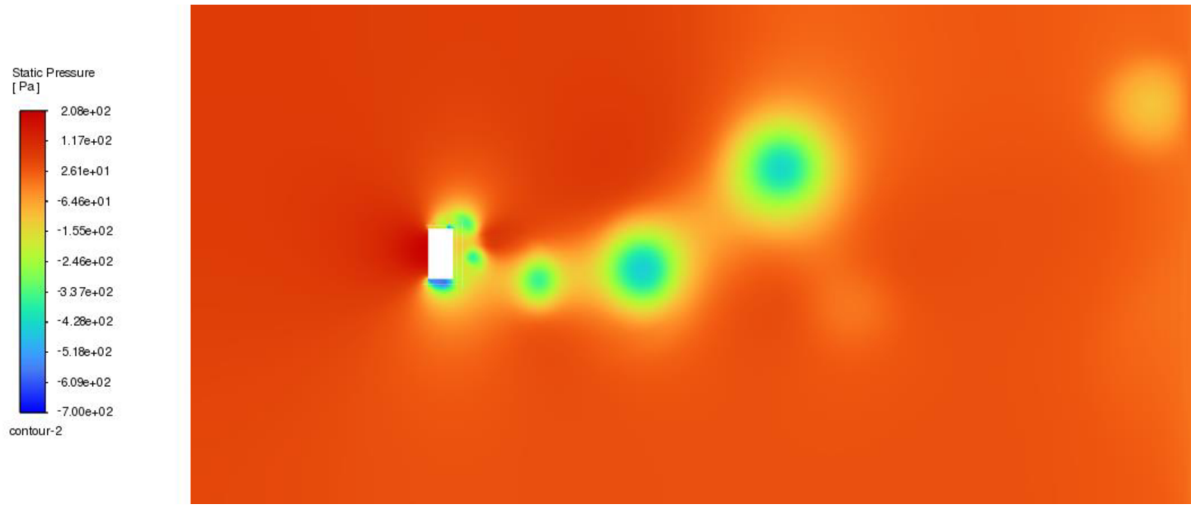

b)

Figure 5.4-2 a) *Velocity magnitude changes through the domain,* ***b)*** *Static pressure changes through the domain*

The shedding pattern is more complex and less consistent than it was at the rounded bodies (Figure 5.4-2 a)). This, and the multiple appearing amplitudes can be caused by the detachment of vortex structures on the leading edge of the flowed body and the subsequent influence of these vortices on the side edges.

The static pressure varies across the surface of a rectangle, displaying a non-uniform distribution (Figure 5.4-2 b)). Regions where the flow remains undisturbed, like the upstream face, exhibit higher static pressure. Low-pressure zones emerge in regions where the flow detaches from the surface or transitions into turbulence, such as in the wake behind the rectangle or in proximity to the edges where vortices form.

The boundary layer separation happens on the sharp corners of the profile (Figure 5.4-3). The separation point is exact and does not change its place. Multiple separation points are observable due to the flow reattachment. In this case, it's visible on the surface and the corner on the right-hand side. At this corner a significant vortex forms.

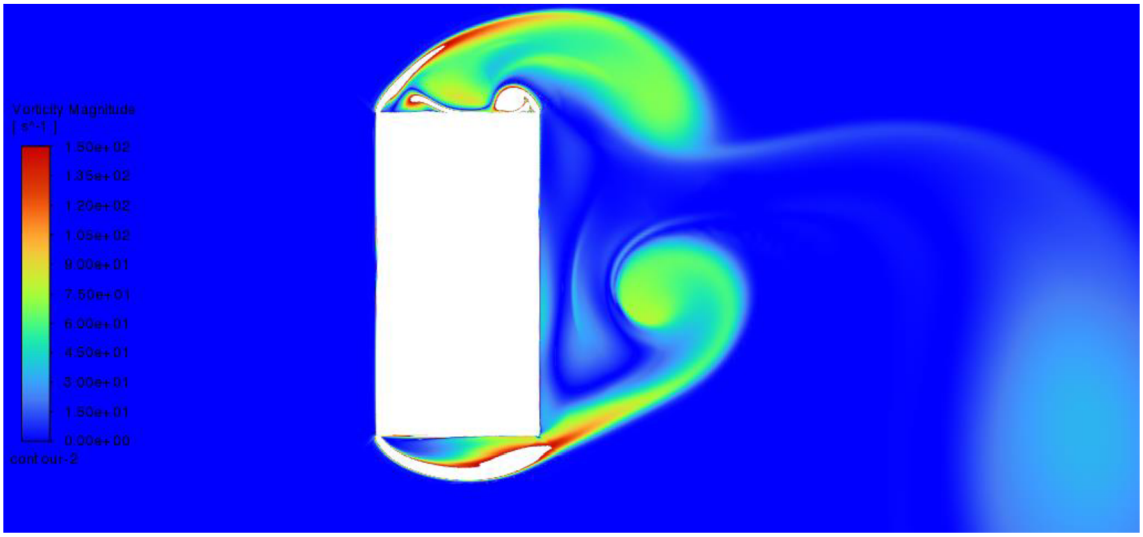

Figure 5.4-3 *Boundary layer separation shown by vorticity magnitude for Re=50 000*

The Strouhal number varies in values higher than the square cylinder (Figure 5.4-4). It can be averaged to 0,14. The frequency (Figure 5.4-4) shows a growing tendency by the increment of the Reynolds number.

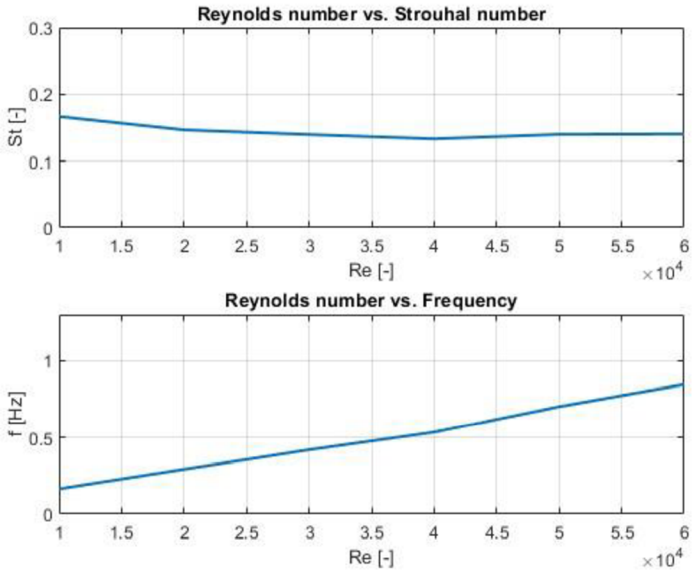

Figure 5.4-4 *Functions of Strouhal number and frequency based on the Reynolds number*

5.5 TRIANGULAR CYLINDER

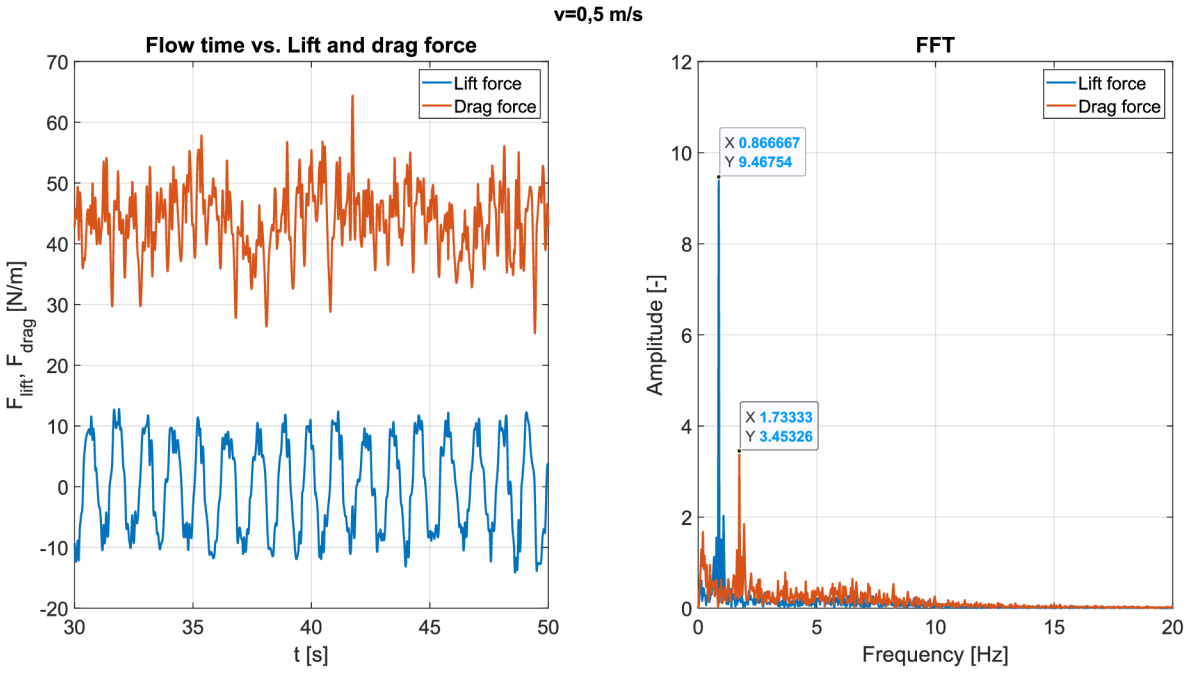

Figure 5.5-1 *The course of lift and drag forces and its FFT analysis for Re=50 000*

The triangle was the last cross-section to be analyzed. This profile, due to its three corners and placement in the domain, was the hardest to be meshed. It required multiple approaches to find the correct division of the domain to avoid an error message. The most common message, which resulted immediate abortion of the simulation, was the 'Floating point exception', which means, that a division by zero

occurs during the calculation process. This error is often caused by the mesh quality or by the boundary conditions and calculation model. In this situation, the quality of the mesh seemed to be the root cause, which originated from the division of the domain.

The course of the lift force shows a periodic pattern (Figure 5.5-1 a)). Some disturbance is noticeable which causes the lift force to oscillate on multiple frequencies, however, only one amplitude is significant. The drag force, as shown in Figure 5.5-1 a), on the other hand, is more noisy and also oscillates on multiple frequencies. Figure 5.5-1 b) shows the FFT analysis which is observable, that the value of the drag forces' frequency with the highest amplitude (1,73 Hz) is double the frequency of the lift force, which phenomenon appeared at the circular cylinder.

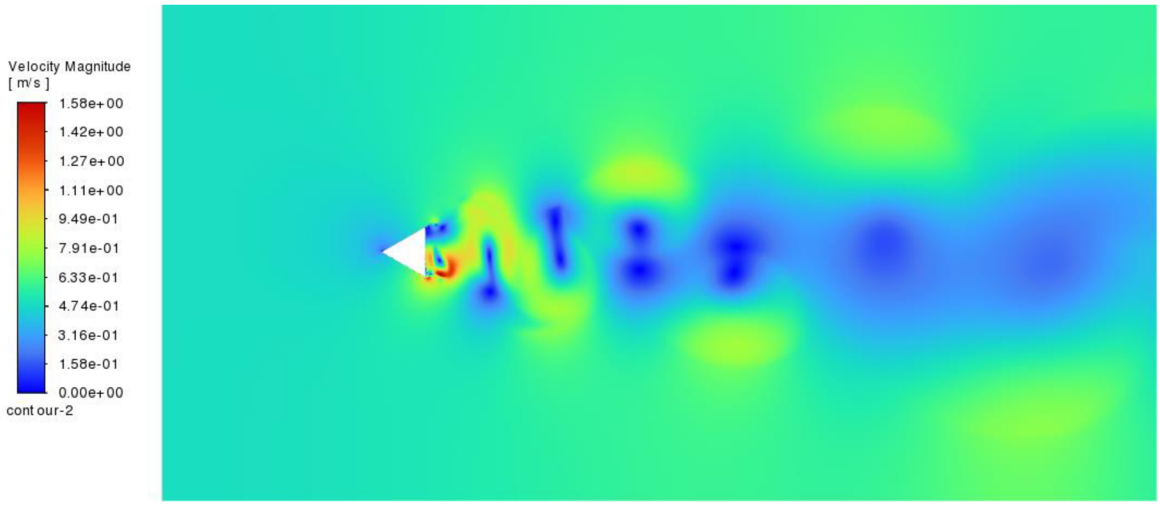

a)

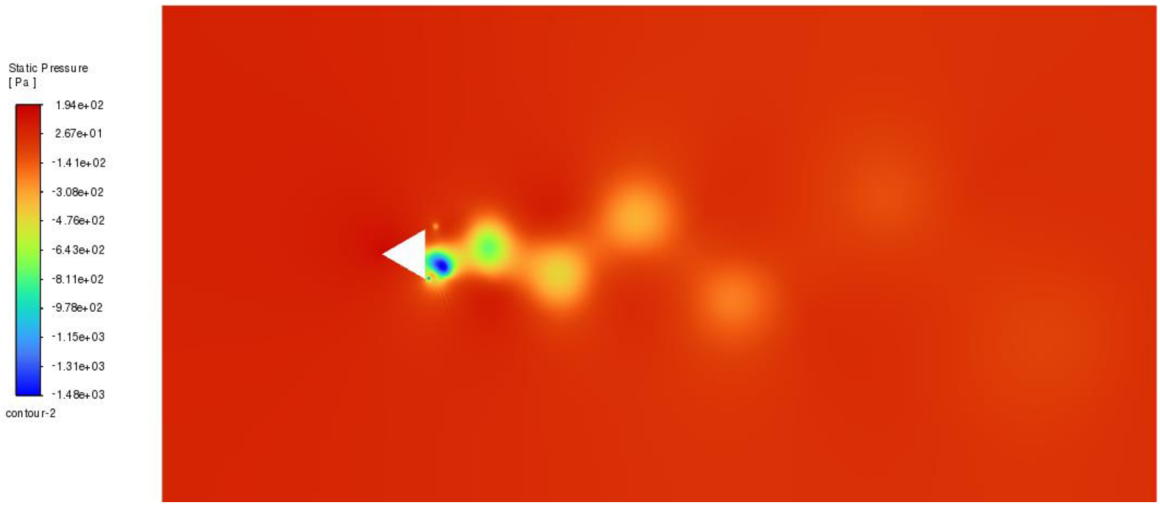

b)

Figure 5.5-2 a) *Velocity magnitude changes through the domain,* ***b)*** *Static pressure changes through the domain*

Examining the vortex shedding of the flow passing through a triangular cylinder, vortex pairs are observable (Figure 5.5-2 a)). The regular Kármán vortex street appears but with different vortex formation structures. It can be noticed, that a low-velocity vortex pattern surrounded by high-velocity vortices formulates a symmetric shedding pattern behind the body. Despite the other bluff bodies, the lowest velocity value does not

appear at the area, where the flow attaches the profile (Figure 5.5-2 a)). The pressure distribution around the body is not uniform. The lowest static pressure is observable where the flow detaches the cross-section.

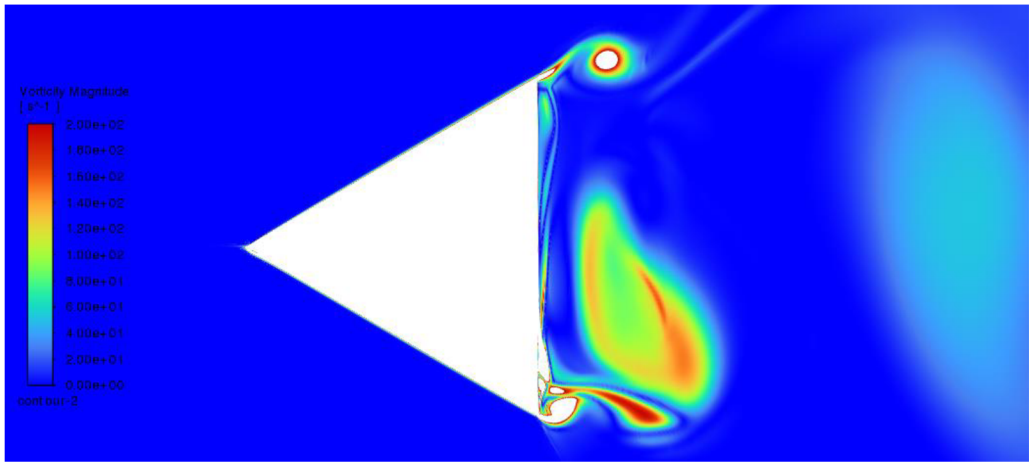

Figure 5.5-3 *Boundary layer separation shown by vorticity magnitude for Re=50 000*

The point of separation is exact, boundary layer separation happens on the corners on the right-hand side of the cross-section. Flow reattachments happen only on the side which does not face the inlet flow. Vortices do not formulate on the other two sides. Vortex shedding from the corners of the triangle can result in fluctuations in the lift force, which causes the course to differ from the sinusoidal pattern.

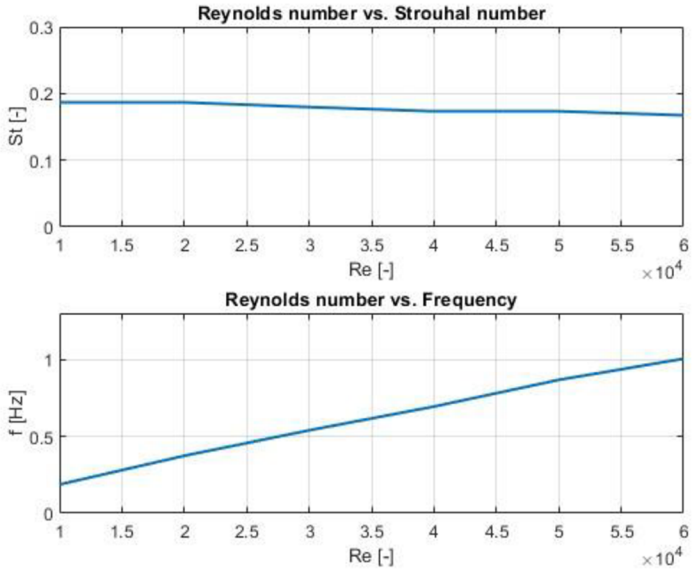

Figure 5.5-4 *Functions of Strouhal number and frequency based on the Reynolds number*

The Strouhal number decreases with increased Reynolds number and it can be averaged as 0,18. The frequency increases with the Reynolds number.

6 DISCUSSION

6.1 DISCUSSION OF SIMULATION RESULTS

This chapter provides a discussion of the results mentioned in the previous chapters. The cross shapes were analyzed for five different velocity inputs. The results were compared by values of lift and drag forces, vortex shedding frequency, and Strouhal number.

The lift force came out to be the highest for the square-shaped cylinder and the lowest for the circular cylinder (Figure 6.1-1). This can be caused by the shape and sharpness of edges, wake structure, separation- and reattachment points, etc. The square is a sharp-edged shape, which leads to fixed separation points at the frontal corners. This causes early vortex separation creating a more turbulent and complex wake, resulting in symmetric and predictable vortex shedding with more intensive lift force. On the contrary, the circular cylinder has a smooth curvature leading to a non-fixed separation point, which delays the separation. This smooth geometry leads to a more uniform pressure distribution around the body resulting in smoother flow and reduced lift fluctuations. It's observable how the geometry aspect ratio affects the resulting lift force. The elliptic-cross shape produces a much higher lift than the circle and the rectangle has a lower lift than the square.

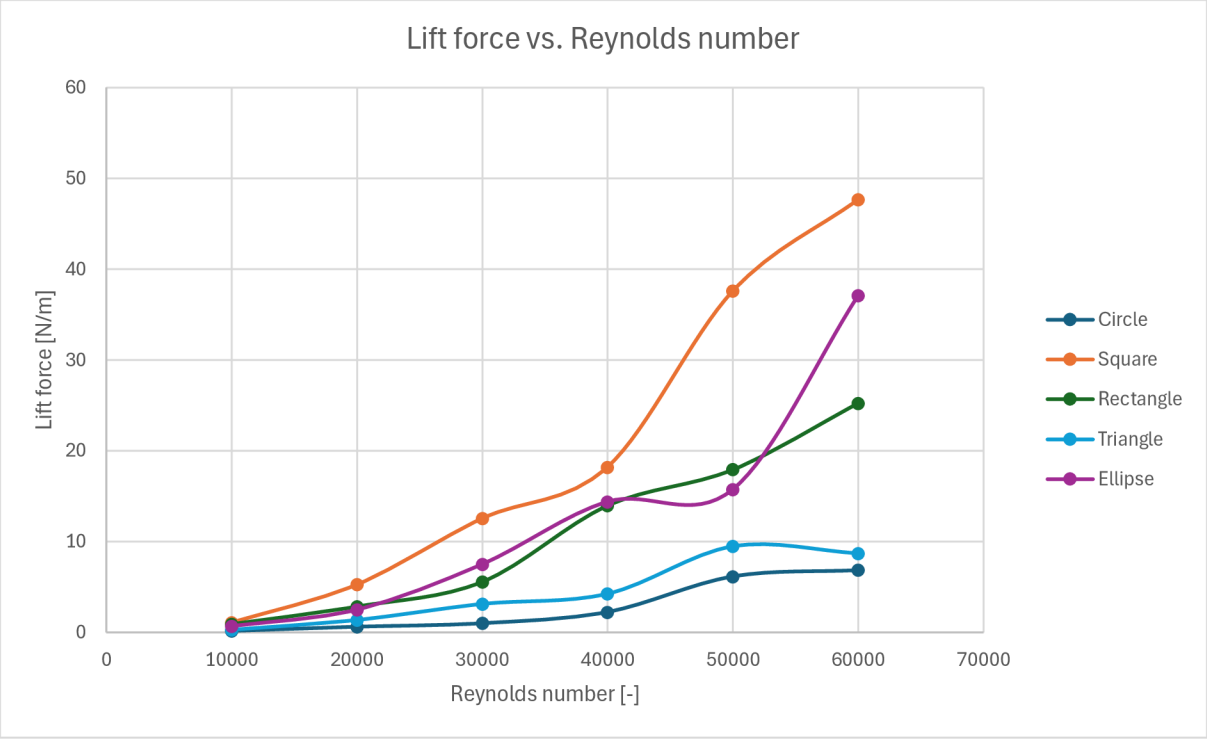

Figure 6.1-1 *Comparison of lift forces for different cross shapes and Reynolds numbers*

Moving forward to the drag force the square shape seemed to produce the highest drag and the circular cylinder the lowest (Figure 6.1-2). Due to the non-fixed separation point cross shapes with smooth curves tend to generate a narrower wake than the

geometries with sharp edges, generating overall lower drag. In Figure 6.1-2 is noticeable, that the rectangular shape produced lower values than the square. Their frontal length matches while the horizontal sides of the rectangle are half the size of the edges of the square which leads to the decrease of skin friction drag on the rectangle. Comparing the ellipse with the circle, the asymmetry of the ellipse leads to a less even pressure distribution, resulting in higher drag than the symmetrical circular shape.

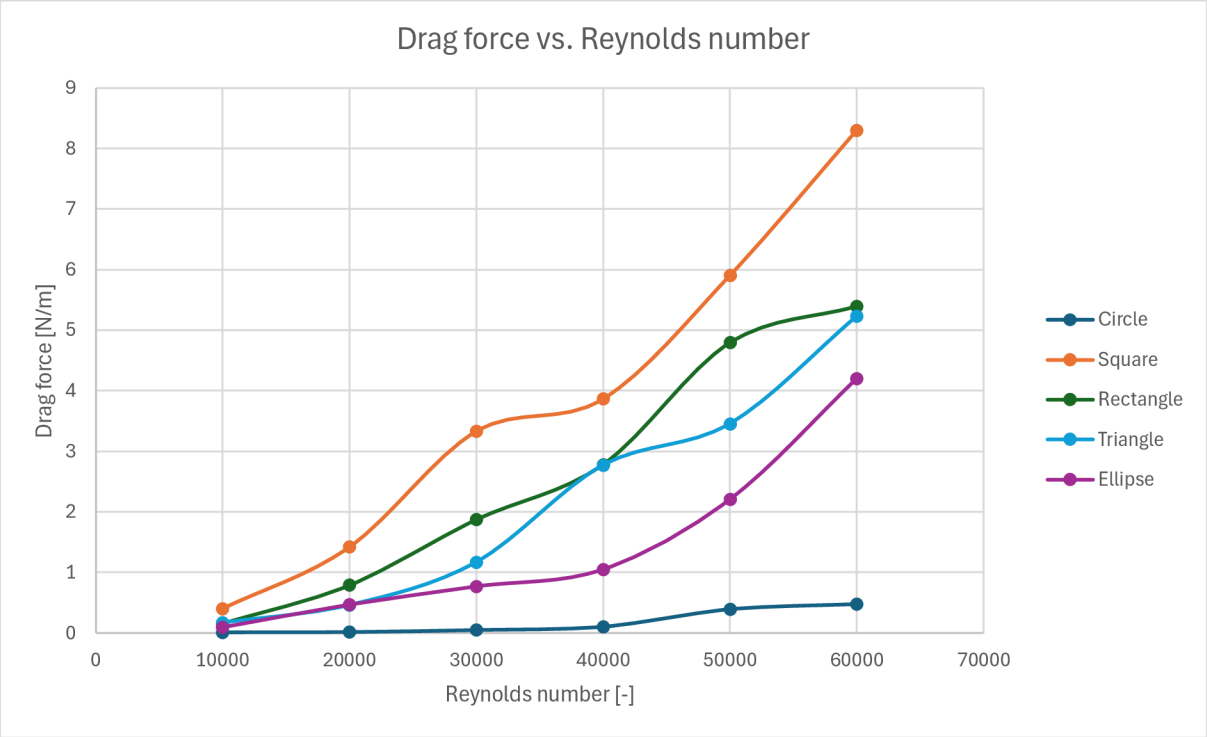

Figure 6.1-2 *Comparison of drag forces for different cross shapes and Reynolds numbers*

Comparing the frequencies, Figure 6.1-3 shows, that the circular cylinder has the highest frequency while the square-shaped cylinder has the lowest. In general shapes with sharp edges result in a significant wake compared to the curvy shapes. The more turbulence in the wake region leads to more disturbance and a less uniform vortex shedding. Figure 6.1-3 also shows that rectangles with a higher aspect ratio (in this case the rectangle has AR=0,5 and the square has AR=1) tend to have a lower frequency of vortex shedding. This also applies to the circle and the ellipse. Circle due to its symmetry and continuous curvature has a more uniform and delayed flow separation which leads to a narrower and more stable wake resulting in a more frequent and stable vortex shedding.

The previous chapter mentioned that the lift force's frequency has double the drag force's value for the circular cylinder. This phenomenon was examined by Dahl. Dahl states in his publication that the cylinder response is described as ‘dual resonance’ is a condition where the lift force is resonant with the crossflow natural frequency and the drag force is in resonance with the effective in-line natural frequency. It’s a phenomenon occurring through a wide range of Reynolds numbers. He stated that if

the nominal frequency ratio of these two frequencies moves around 2, the phenomenon is guaranteed to occur. [44]

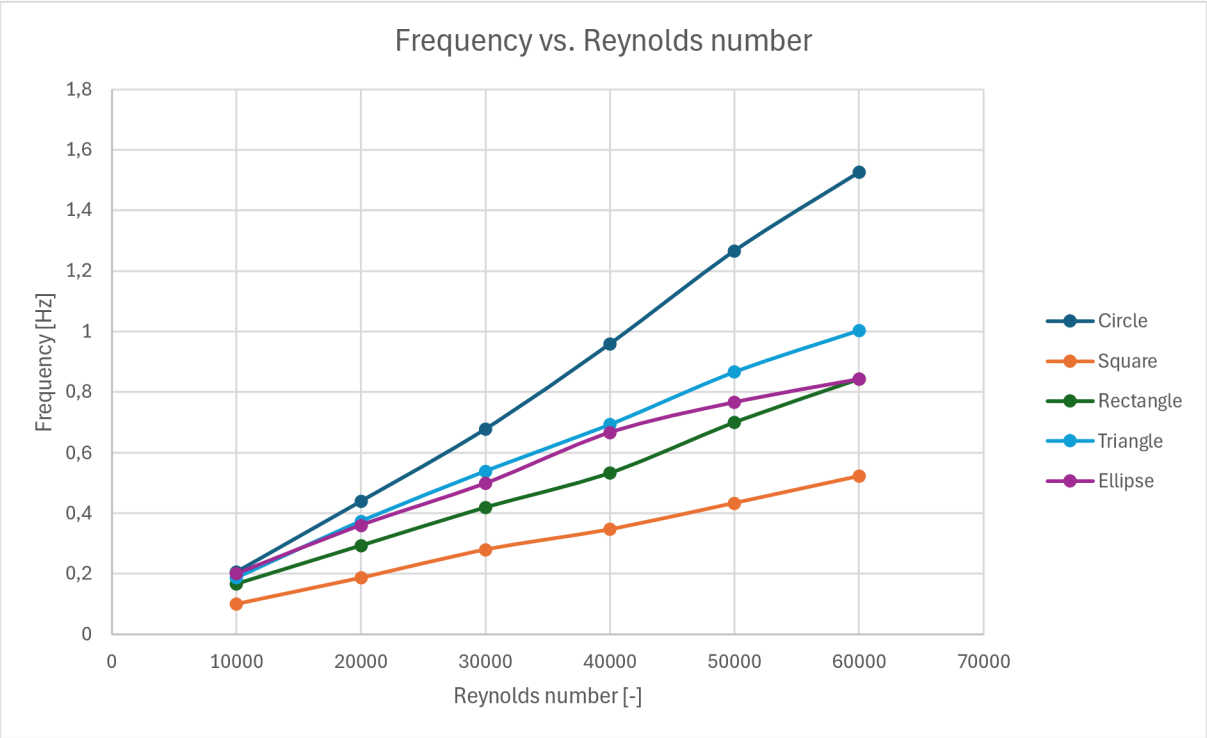

Figure 6.1-3 *Comparison of vortex shedding frequencies for different cross shapes and Reynolds numbers*

The last parameter to be discussed was the Strouhal number. Figure 6.1-4 shows, that the circular cylinder has the highest frequency while the square-shaped cylinder has the lowest, showing similar results as it was seen at the frequency. These results correspond to the definition equation (2.3.1) of the Strouhal number which shows that the frequency of the vortex shedding highly influences the Strouhal number. It‘s hard to compare the results with experimental or calculation data from the literature because there is no publication representing cases with similar boundary conditions for every cross-section. There is a large amount of data from experimental and numerical studies about the circular cylinder. Norberg provided wind tunnel experiments for a wide range of Reynolds numbers with similar construction dimensions as has the domain presented in this thesis, where for Re=21 400 the Strouhal number came out to be 0,189 [45]. Kashiyama, Tamai, Inomata, and Yamaguchi provided a high Reynolds number numerical study about a fixed, three-dimensional circular cylinder for different mesh refinements [46]. The coarse mesh resulted in the Strouhal number being 0,22 with an increasing course for higher Re values, while for the fine mesh, it came out to be around 0,19 with a decreasing course [46]. This study shows, how the discretization of the mesh affects the Strouhal number. The above-mentioned values align with the values presented in this thesis, where the Strouhal number shows an increasing tendency of values from 0,20667 up to 0,25435.

For the elliptic cross shape with AR<1 was not found a relevant publication about the Strouhal number. Johnson, Thompson, and Hourigan provided a study about a low Re flow passing through an elliptical cylinder examined by 2D spectral-element method.

The highest value of Re to be tested was 200, which is not even close to the Reynolds numbers shown in the present study. For this inlet condition and an aspect ratio of 0,625, the Strouhal number came out to be 0,205 [47]. Figure 6.1-4 shows, that the Strouhal number varies between 0,14 and 0,2 showing a decreasing course with higher Reynolds numbers.

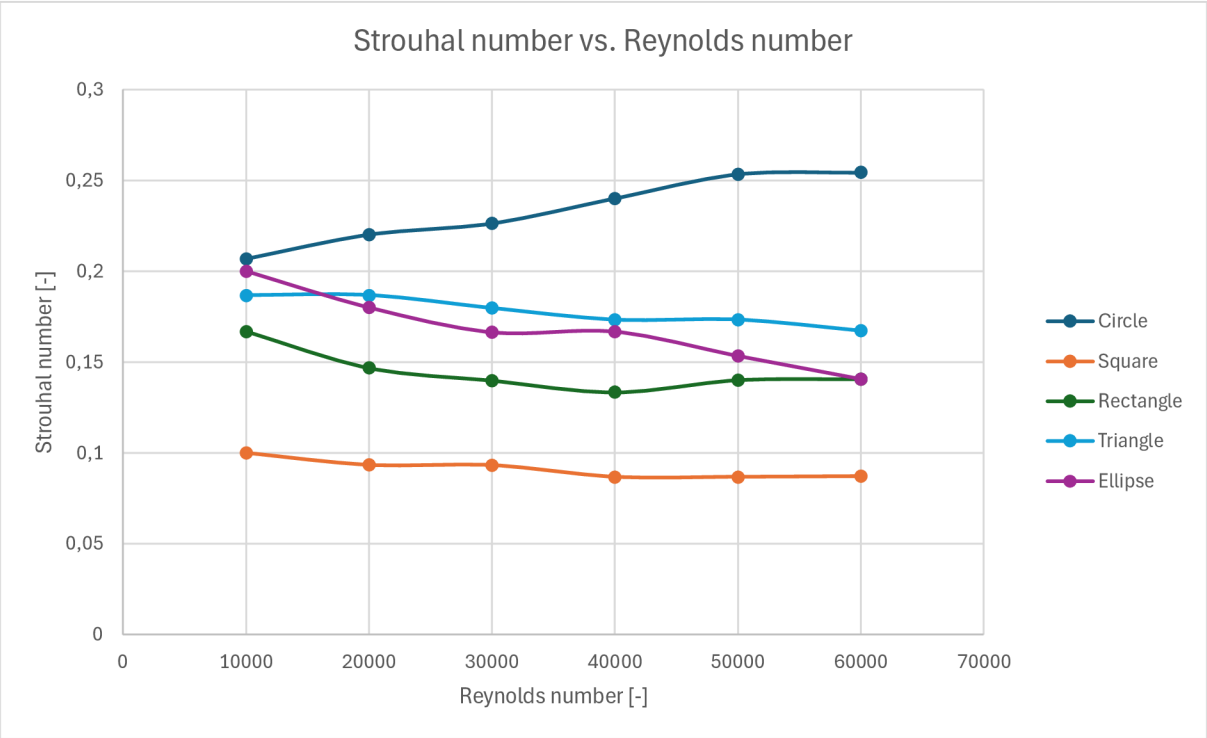

Figure 6.1-4 *Comparison of Strouhal numbers for different cross shapes and Reynolds numbers*

Choi and Kwan carried out experiments with an Eiffel-type wind tunnel, measuring the aerodynamic response on flexible-mounted rectangular cylinders with different aspect ratios and angles of attack. The study showed, that for Re=40 000, AR=1 (square shape), and an angle of attack 0° the Strouhal number came out to be around 0,12 [48]. This value slightly differs from the values reached in the present study. Figure 6.1-4 shows values of Strouhal number to be between 0,1 and 0,087 with a decreasing course. Verstappen and Veldman performed a fourth-order finite-volume method DNS analysis of an incompressible fluid flow past a square cylinder at Re=22 000 reaching a Strouhal number of 0,133 [49]. This value is also higher than the values measured in this thesis. The difference can be caused by multiple factors. The most likely causes of the discrepancies are the boundary conditions. In this study, the velocity distribution was assumed to be uniform which does not represent a real case. For the boundaries of the geometry, a non-slip boundary condition was set which does not apply in reality. This BC predicts the same velocity in the near-wall region as the wall itself, which can result in a significant difference.

Knisely carried out multiple experiments in wind tunnel and water channel for rectangular cylinders with different aspect ratios and angles of attack at Re=23 000. For AR=0,5 (which aligns with the aspect ratio of the rectangle analyzed in the present

study) both the water channel and wind tunnel resulted in St=0,14, matching with the results in this thesis (Figure 6.1-4) [50].

For the triangular cross shape came out much lower Strouhal numbers, than for the cases found in literature. Yagmur et. al provided CFD simulations for an equilateral triangle with the same boundary conditions as were set in the present study resulting a Strouhal number of 0,22-0,23 at Re=10 000-60 000 [51]. The only differences between the two cases are the sizes of the domain and the number of mesh elements, which means that these parameters also highly influence the simulation results. Another cause could be the number of time steps and the time step size.

In general, it can be concluded, that boundary conditions play big role in the final results which proves why is important to be consistent and thoughtful while choosing them. It's important to state, that the results presented in this thesis are accurate for the present cases which were carried out in the most simplified way.

6.2 DISCUSSION ABOUT THE IDEAL SHAPE FOR A VIVACE CONVERTER

To choose the ideal cross-section for a VIV energy harvester there are multiple factors to be considered: diameter, length, material properties, surface characteristics, structural stiffness and flexibility, mass ratio, etc. For a 2D problem, we can only decide based on the vortex shedding frequency, flow separation, lift- and drag forces. Selecting the optimal cross-sectional shape involves balancing these characteristics to match the specific flow conditions and structural requirements of the VIV energy harvester. Based on the simulation results and the production difficulties only two cross-sections can be considered to be the ideal cross shape: the circular- and the square-shaped cylinder.

From the tested geometries the square-shaped cylinder resulted in the highest values of lift and drag forces and the lowest values of vortex shedding frequencies. The high lift force is a big advantage of this shape, on the other hand, the high values and irregular course of the drag force could be problematic from a structural point of view. These cylinders most of the time are allowed to to move only in the vertical direction, so the fatigue load is significant and unpredictable. The square has four apexes which all are concentrators of stress resulting in a lower safety factor against limit states of strength and fatigue.

The circular cylinder in comparison with the square-shaped cylinder produced much lower values of lift and drag forces but also resulted in the highest value of vortex shedding frequency. To increase the produced power – and therefore also the efficiency – is essential to produce as high lift as possible, which is not one of the strengths of the circular cross-section, on the other hand, its high and regular vortex shedding frequency means a great advantage. The moderate and predictable course of drag force lowers the fatigue load which in combination with the curvy shape leads to higher resistance against limited states of strength and fatigue. From a production point of view, the circular cross-shape is the easiest geometry to manufacture.

In conclusion, although the square shape produces higher values of the drag and lift forces, the circular cylinder due to its regular and predictable vortex shedding pattern,

higher strength, and fatigue resistance, manufacturing efficiency is a greater candidate for this purpose. It also needs to be mentioned, that due to its insignificant VIV production may be less optimal at extremely low Reynolds number flows.

CONCLUSION

The thesis starts with a brief description of the problems of the energy industry and the current approaches to producing energy as efficiently and as environmentally friendly as possible. The attention was focused mainly on hydro energy powerplants and the hydrokinetic energy harvesting methods therefore introducing the VIVACE converter. The system uses a generally unwanted phenomenon, vortex-induced vibrations of a cylinder undergoing vortex shedding, to produce energy. An extensive chapter was devoted directly to understanding the physics behind the vortex shedding and the formulation of the Kármán vortex street. Another chapter of the theoretical part provides an overview of the VIVACE converter itself, including a description of the lab model and presenting the governing equations describing the motion of the cylinder.

The practical part starts with the definitions of the governing equations of CFD which is essential to understand how the calculation itself works and presents the details of the analysis settings. The simulations were provided for five different cross-section shapes and six different inlet boundary conditions. The geometries of the shapes (circle, ellipse, square, rectangle, triangle) were created so that their characteristic diameter was the same for their easier and more accurate further comparison. An extensive part of this chapter was devoted to the detailed description of the mesh generation process, the chosen boundary conditions, the used turbulence model, and the simulation settings. The calculations were provided using an SST k-ω model for transient flow.

The cross shapes were examined by the drag and lift forces they produced. Post-processing also included evaluation of the vortex shedding frequency by performing FFT analysis. The shedding patterns were also investigated, where the circular cylinder performed well. Except for the circular cross-shape, the other shapes showed irregularities in vortex shedding which proves them to be less predictable than the circle. This cross shape was also the only one with uniform pressure distribution around the boundaries of its geometry. The boundary layer separation was examined by plotting the vorticity magnitude. It showed, that the curvy cross-shapes don't have a fixed separation point on the contrary with the shapes with sharp edges. It also showed the flow reattachment to the wall of the angular shapes.

The last chapter discusses the results of the investigated parameters and compares the cross-sections based on them. The square-shaped cylinder produced the highest values of drag and lift forces but frequency-wise performed badly. On the other hand, looking at the produced drag and lift the circular cylinder produced the lowest values, however, it presented the best results of vortex shedding frequency. This chapter also included a comparison of Strouhal numbers calculated in the present study and the experimental and simulation data obtained from the literature available. For the Strouhal number of square- and triangular shapes came out slightly different values than what can be found in the previous publications. These differences can be caused by the various boundary conditions (e.g. 2d vs 3d, unknown turbulence boundary conditions, etc.), but the choice of turbulence modeling can also significantly change the results.

The last section of the final chapter discusses the optimal choice of cross-shape for the VIV energy harvestor. Based on the above-mentioned parameters, it was concluded that although the circular cylinder produces the lowest values of drag and lift forces, it has the most predictable vortex shedding behavior, making this shape the ideal choice for this type of energy harvestion. The square shape also seemed to be a great candidate for this purpose, but it failed from a structural point of view.

To conclude energy harvesting from vortex-induced vibrations is an actual field of study with infinite possibilities. Although the simulations presented in this thesis were significantly simplified (especially by confining to fixed body), this study could be useful in providing a general overview of how the geometrical parameters affect the vortex shedding behavior. The present study did not answer all the questions about this topic, leaving space for further investigation.

BIBLIOGRAPHY

[1] DENCHAK, Melissa. *Fossil Fuels: The Dirty Facts*. Online. Natural Resources Defense Council. 2022. Dostupné z: https://www.nrdc.org/stories/fossil-fuels-dirty-facts#sec-whatis. [cit. 2024-01-28].

[2] DENCHAK, Melissa. *Fossil Fuels: The Dirty Facts - Burning Fossil Fuels*. Online. Natural Resources Defense Council. 2022. Dostupné z: https://www.nrdc.org/stories/fossil-fuels-dirty-facts#sec-burning. [cit. 2024-01-28].

[3] INTERNATIONAL ENERGY AGENCY. *World Energy Outlook 2023*. 2023.

[4] *Renewable energy targets*. Online. European Commission. 2023. Dostupné z: https://energy.ec.europa.eu/topics/renewable-energy/renewable-energy-directive-targets-and-rules/renewable-energy-targets_en. [cit. 2024-01-28].

[5] *What is renewable energy?* Online. United Nations. Dostupné z: https://www.un.org/en/climatechange/what-is-renewable-energy. [cit. 2024-01-29].

[6] IRENA (2023). *Renewable energy statistics 2023*. Abu Dhabi: International Renewable Energy Agency, 2023. ISBN 978-92-9260-537-7.

[7] *History of Hydropower*. Online. U.S. Department of Energy. Dostupné z: https://www.energy.gov/eere/water/history-hydropower. [cit. 2024-01-29].

[8] SAFARIK, Branislav. *The Early History of Water Power*. Online. FUERGY. 2019. Dostupné z: https://www.fuergy.com/blog/the-early-history-of-water-power. [cit. 2024-01-29].

[9] RICHARDSON, Janet. *A brief history of Hydroelectricity*. Online. The Renewable Energy Hub UK. 2023. Dostupné z: https://www.renewableenergyhub.co.uk/main/hydroelectricity-information/history-of-hydroelectricity. [cit. 2024-01-29].

[10] *The History of Hydropower & Hydroelectric Energy*. Online. TRVST. 2019. Dostupné z: https://www.trvst.world/renewable-energy/the-history-of-hydroelectric-energy/. [cit. 2024-01-29].

[11] ESCHNER, Kat. *When the Niagara River Crushed a Power Plant*. Online. Smithsonian Magazine. 2017. Dostupné z: https://www.smithsonianmag.com/smart-news/when-niagara-crushed-power-plant-180963549/. [cit. 2024-01-29].

[12] *Kaplan turbine*. Online. In: Wikipedia: the free encyclopedia. San Francisco (CA): Wikimedia Foundation, 2022. Dostupné z: https://en.wikipedia.org/wiki/Kaplan_turbine. [cit. 2024-01-29].

[13] *Collapse of Schoellkopf power plant*. Online. The Buffalo News. Dostupné z: https://buffalonews.com/multimedia/june-7-1956-collapse-of-schoellkopf-power-plant/collection_e31a6291-7f40-5bdd-86b5-05e9d177e5e4.html#1. [cit. 2024-01-29].

[14] *The world's nine largest operating power plants are hydroelectric facilities*. Online. U.S. Energy Information Administration. 2016. Dostupné z: https://www.eia.gov/todayinenergy/detail.php?id=28392. [cit. 2024-01-29].

[15] *Hydroelectricity: Generating methods*. Online. In: Wikipedia: the free encyclopedia. San Francisco (CA): Wikimedia Foundation, 2024. Dostupné z: https://en.wikipedia.org/wiki/Hydroelectricity#Generating_methods. [cit. 2024-01-29].

[16] BROWN, Tyson. *Hydroelectric Energy*. Online. National Geographc Education. 2023. Dostupné z: https://education.nationalgeographic.org/resource/hydroelectric-energy/. [cit. 2024-01-29].

[17] *Types of Hydropower Plants*. Online. U.S. Department of Energy. Dostupné z: https://www.energy.gov/eere/water/types-hydropower-plants. [cit. 2024-01-29].

[18] CROPLEY, John. *Closed-Loop Hydro's Climate Impact Found Less Than Batteries*. Online. RTO Insider. 2023. Dostupné z: https://www.rtoinsider.com/53822-closed-loop-hydro-climate-impact-less-batteries/. [cit. 2024-01-29].

[19] *Wave energy*. Online. Open energy information, data and resources. Dostupné z: https://openei.org/wiki/PRIMRE/Basics/Wave_Energy. [cit. 2024-01-29].

[20] NEILL, Simon P. a HASHEMI, M. Reza. *Fundamentals of Ocean Renewable Energy*. Online. Academic Press, 2018. ISBN 978-0-12-810448-4. Dostupné z: https://doi.org/10.1016/C2016-0-00230-9. [cit. 2024-01-29].

[21] *Current Energy*. Online. Open energy information, data and resources. Dostupné z: https://openei.org/wiki/PRIMRE/Basics/Current_Energy. [cit. 2024-01-29].

[22] NIEBUHR, C. M.; VAN DIJK, M.; NEARY, V.S. a BHAGWAN, J.N. A review of hydrokinetic turbines and enhancement techniques for canal installations: Technology, applicability and potential. Online. *Renewable and Sustainable Energy Reviews*. 2019, roč. 113. Dostupné z: https://doi.org/10.1016/j.rser.2019.06.047. [cit. 2024-04-10].

[23] TIAN, Wenlong; MAO, Zhaoyong a DING, Hao. Design, test and numerical simulation of a low-speed horizontal axis hydrokinetic turbine. Online. *International Journal of Naval Architecture and Ocean Engineering*. 2018, roč. 10, č. 6, s. 782-793. Dostupné z: https://doi.org/10.1016/j.ijnaoe.2017.10.006. [cit. 2024-04-10].

[24] BERNITAS, M.M.; RAGHAVAN, K.; BEN-SIMONS, Y. a GARCIA, E.M.H. VIVACE „Vortex Induced Vibration Aquatic Clean Energy…: A New Concept in Generation of Clean and Renewable Energy From Fluid Flow. *Journal of Offshore Mechanics and Arctic Engineering*. 2008, roč. 130, č. 4.

[25] BUSH, Evan. *75 years ago: Famous clip of 'Galloping Gertie' not accurate, study says*. Online. The Seattle Times. 2015. Dostupné z: https://www.seattletimes.com/seattle-news/75-years-ago-famous-clip-of-galloping-gertie-not-accurate-study-says/. [cit. 2024-01-29].

[26] *How it works*. Online. Vortex Hydro Energy. Dostupné z: https://www.vortexhydroenergy.com/technology/how-it-works/. [cit. 2024-01-29].

[27] JANALÍK, Jaroslav. *Obtékání a odpor těles*. Online. Vysoká škola báňská – Technická univerzita Ostrava, 2008. [cit. 2024-01-06].

[28] OPENSTAX. *College Physics*. Online. OpenStax CNX, 2016. Dostupné z: https://cnx.org/contents/Ax2o07Ul@9.73:HR_VN3f7@3/Introduction-to-Science-and-th. [cit. 2024-01-06].

[29] *Flow separation (boundary layer separation)*. Online. TEC Science. 2020. Dostupné z: https://www.tec-science.com/mechanics/gases-and-liquids/flow-separation-boundary-layer-separation/. [cit. 2024-01-29].

[30] LEISHMAN, J. Gordon. *Introduction to Aerospace Flight Vehicles*. Online. Embry-Riddle Aeronautical University, 2023. ISBN 979-8-9852614-0-0. [cit. 2024-01-06].

[31] JONES, Alva Marle. *Drag coefficients for flat plates, spheres, and cylinders moving at low reynolds numbers in a viscous fluid*. Master thesis. Oregon: Oregon State College, 1958.

[32] *Drag and Lift*. Online. Applied Fluid Mechanics Online Textbook. Dostupné z: https://kdusling.github.io/teaching/Applied-Fluids/Notes/DragAndLift. [cit. 2024-01-29].

[33] MATĚJKA, Jan. *Vliv Kármánových vírů na vzduchem obtékané těleso*. Diplomová práce, vedoucí Petr Skalka. Brno: . Vysoké učení technické v Brně, Fakulta strojního inženýrství, Ústav mechaniky těles, mechatroniky a biomechaniky., 2022. Dostupné také z: https://www.vutbr.cz/studenti/zav-prace/detail/140358.

[34] *Vortex Shedding in Water*. Online. Harvard Natural Sciences Lecture Demonstrations. Dostupné z: https://sciencedemonstrations.fas.harvard.edu/presentations/vortex-shedding. [cit. 2024-01-29].

[35] *Strouhal Number*. Online. Study smarter. Dostupné z: https://www.studysmarter.co.uk/explanations/engineering/engineering-fluid-mechanics/strouhal-number/. [cit. 2024-01-29].

[36] ARDERNE, Christopher James. *Investigation of the pressure and velocity distribution around cylinders in an airstream with PIV measurements and CFD*. Bachelors thesis. Stellenbosch: Stellenbosch University Department of Mechanical and Mechatronic Engineering, 2013.

[37] RAGHAVAN, Kamaldev. *Energy extraction from a steady flow using vortex induced vibration*. 2007. ISBN 9780549183129.

[38] TU, Jiyuan; LIU, Chaoqun a YEOH, Guan Heng. *Computational fluid dynamics*. 2nd ed. Waltham, Mass: Butterworth-Heinemann, 2013. ISBN 9780080982434.

[39] *K-Omega Turbulence models*. Online. Simscale. 2023. Dostupné z: https://www.simscale.com/docs/simulation-setup/global-settings/k-omega-sst/. [cit. 2024-01-30].

[40] WASSERMAN, Shawn. *Choosing the Right Turbulence Model for Your CFD Simulation*. Online. Engineering.com. 2016. Dostupné z: https://www.engineering.com/story/choosing-the-right-turbulence-model-for-your-cfd-simulation. [cit. 2024-01-30].

[41] VOSTRUHA, Karel a PELANT, Jaroslav. Perturbation Analysis of “k—ω” and “k—ε” Turbulent Models. Wall Functions. Online. *EPJ Web of Conferences*. 2013, roč. 45, č. 01097, s. 1-2. ISSN 2100-014X. Dostupné z: https://doi.org/10.1051/epjconf/20134501097. [cit. 2024-01-31].

[42] FERZIGER, Joel H. a PERIC, M. *Computational methods for fluid dynamics*. 3rd, rev. ed. Berlin: Springer, c2002. ISBN 35-404-2074-6.

[43] SCHLICHTING (DECEASED), Hermann a GERSTEN, Klaus. *Boundary-Layer Theory*. 9th ed. 2017. Berlin, Heidelberg: Springer Berlin Heidelberg, 2017. ISBN 978-366-2529-171.

[44] DAHL, J. M.; HOVER, F. S.; TRIANTAFYLLOU, M. S. a OAKLEY, O. H. Dual resonance in vortex-induced vibrations at subcritical and supercritical Reynolds numbers. Online. *Journal of Fluid Mechanics*. 2010, roč. 643, s. 395-424. ISSN 0022-1120. Dostupné z: https://doi.org/10.1017/S0022112009992060. [cit. 2024-05-19].

[45] NORBERG, C. Fluctuating lift on a circular cylinder: review and new measurements. Online. *Journal of Fluids and Structures*. 2003, roč. 17, č. 1, s. 57-96. ISSN 08899746. Dostupné z: https://doi.org/10.1016/S0889-9746(02)00099-3. [cit. 2024-05-19].

[46] KASHIYAMA, Kazuo; TAMAI, Tsukasa; INOMATA, Wataru a YAMAGUCHI, Satoshi. A parallel finite element method for incompressible Navier–Stokes flows based on unstructured grids. Online. *Computer Methods in Applied Mechanics and Engineering*. 2000, roč. 190, č. 3-4, s. 333-344. ISSN 00457825. Dostupné z: https://doi.org/10.1016/S0045-7825(00)00205-X. [cit. 2024-05-20].

[47] JOHNSON, S.A.; THOMPSON, M.C. a HOURIGAN, K. Flow past elliptical cylinders at low Reynolds numbers. Online. *Proceedings of the Fourteenth Australasian Fluid Mechanics Conference*. 2001, roč. 1, s. 343-346. ISBN 1 876346 33 1. [cit. 2024-05-20].

[48] CHOI, C.K. a KWON, D.K. Determination of the Strouhal number based on the aerodynamic behavior of rectangular cylinders. *Wind and Structures*. 2000, roč. 3, č. 3, s. 209-220. ISSN 1598-6225.

[49] VERSTAPPEN, R.W.C.P a VELDMAN, A.E.P. Direct numerical simulation of turbulence at lower costs. *Journal of Engineering Mathematics*. 1997, roč. 32, č. 2-3, s. 143-159.

[50] KNISELY, C.W. Strouhal numbers of rectangular cylinders at incidence: A review and new data. *Journal of Fluids and Structures*. 1990, roč. 4, č. 4, s. 371-393.

[51] YAGMUR, S.; DOGAN, S.; AKSOY, M.H.; GOKTEPELI, I. a OZGOREN, M. Comparison of flow characteristics around an equilateral triangular cylinder via PIV and Large Eddy Simulation methods. *Flow Measurement and Instrumentation*. 2017, roč. 55, s. 23-36.

LIST OF SYMBOLS AND ABBREVIATIONS USED

Symbol	Name	Dimension
y_w	Absolute distance from the wall	m
$\ddot{y}$	Acceleration	$m.s^{-2}$
y_{max}	Amplitude of the displacement	m
C_y	Amplitude of the fluctuating transverse flow coefficient	-
D_{ch}	Characteristic length of the bluff body	m
$\alpha, \beta, \beta^*, \sigma^*, \sigma, C_1, C_2$	Constants	-
ρ, ρ_w	Density of the fluid	$kg.m^{-3}$
D	Diameter of the body	m
y^+	Dimensionless wall distance	-
y	Displacement	m
ε	Dissipation of turbulent energy	$m^2.s^{-3}$
f_{fluid}	Dominant flow forcing frequency	Hz
C	Drag coefficient	-
F_D	Drag force	N
u, v, w	Flow velocity	$m.s^{-1}$
$c_y(t)$	Fluctuating transverse force coefficient	-
$P_{VIVACE-fluid}$	Fluid power of the system	W
F_{fluid}	Force exerted by the fluid	N
v_∞	Freestream velocity	$m.s^{-1}$
f	Frequency of the vortex shedding	Hz
v_τ	Friction velocity	$m.s^{-1}$
m_a	Inviscid added mass	kg
$F_{inviscid}$	Inviscid component of the force exerted by the fluid	N
ν	Kinematic viscosity	$m^2.s^{-1}$
$F_{kinetic}$	Kinetic force	N
$p_{kinetic}$	Kinetic pressure	Pa
k	Kinetic turbulent energy	$m^2.s^{-2}$
L	Length of the body	m
F_L	Lift force	N
m	Mass of the body	kg
m_d	Mass of the displaced fluid	kg
m_{osc}	Mass of the oscillating system	kg
μ	Molecular viscosity	$kg.m^{-1}.s^{-1}$
f_w	Natural vibration frequency of the body	Hz
f_{osc}	Oscillating cylinder frequency	Hz
T_{osc}	Oscillation period	s
ϕ	Phase difference	-
P_{fluid}	Power in fluid	W
Pr	Prandtl number	-
P_k	Production of turbulent kinetic energy due to mean velocity shear	-
S	Projected frontal area	m^2

C_f	Skin friction coefficient	-
S_u^I, S_v^I, S_w^I	Source term form momentum equations	-
S_T	Source term of energy equations	-
ω	Specific dissipation	s^{-1}
k_{spring}	Spring stiffness	$N.m^{-1}$
k_b	Stiffness of the body	$N.m^{-1}$
St	Strouhal number	-
t	Time	s
Δt	Time-step	s
c_{total}	Total damping coefficient	$N.s.m^{-1}$
C_μ	Turbulence model constant	-
ν_T	Turbulent kinematic viscosity	$m^2.s^{-1}$
μ_T	Turbulent viscosity	$kg.m^{-1}.s^{-1}$
$\hat{y}$	Unit normal vector in the y-direction	-
η_{UL}	Upper limit of the energy harnessed from the system	-
$\dot{y}$	Velocity	$m.s^{-1}$
$F_{viscous}$	Viscous component of the force exerted by the fluid	N
τ_ω	Wall shear stress	$N.m^{-2}$
$W_{VIVACE-fluid}$	Work done on the body during one period	$kg.m^2.s^{-2}$

Abbreviation	**Name of abbrevation**
CFD	Computational fluid dynamics
FFT	Fast Fourier Transformation
R.E.S.	Renewable energy source
VIV	Vortex induced vibrations
VIVACE	Vortex-induced vibrations aquatic clean energy
RANS	Reynolds-averaged Navier-Stokes equations
DNS	Direct Numerical Simulation
BC	Boundary condition

LIST OF FIGURES AND TABLES

LIST OF APPENDICES

APPENDICES

APPENDIX 1 - COURSE OF LIFT AND DRAG FORCES FOR DIFFERENT CROSS-SECTIONS AND ITS FFT ANALYSIS FOR FLOWTIME T=20 S

Circular cylinder

v=0,1 m/s

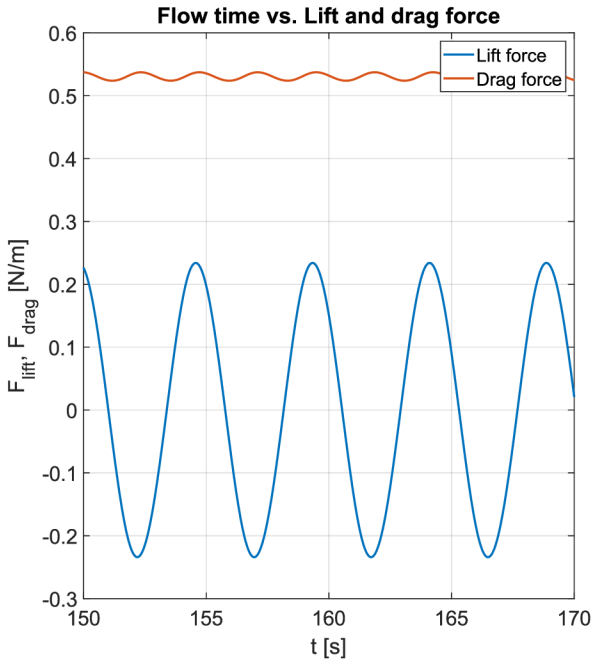

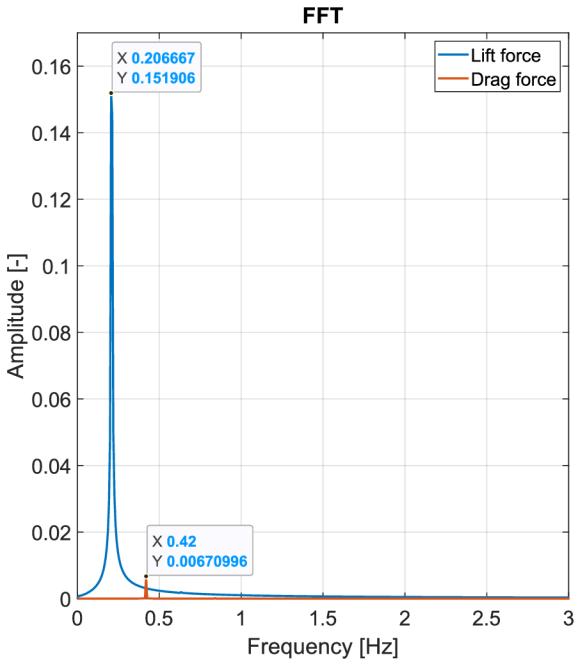

v=0,2 m/s

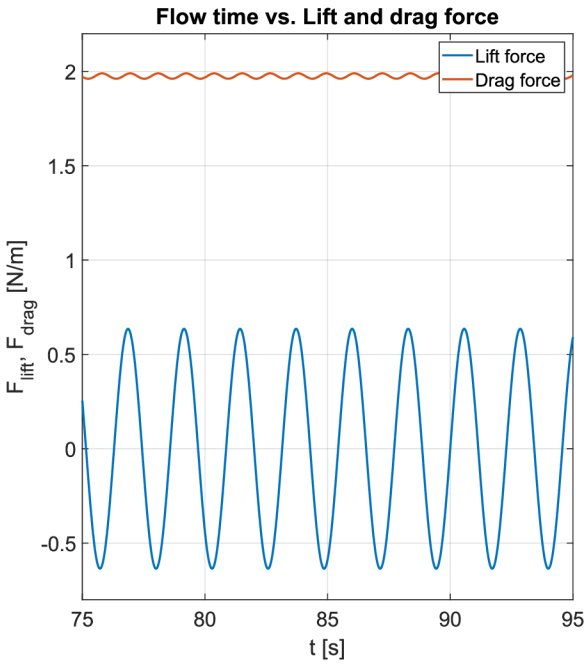

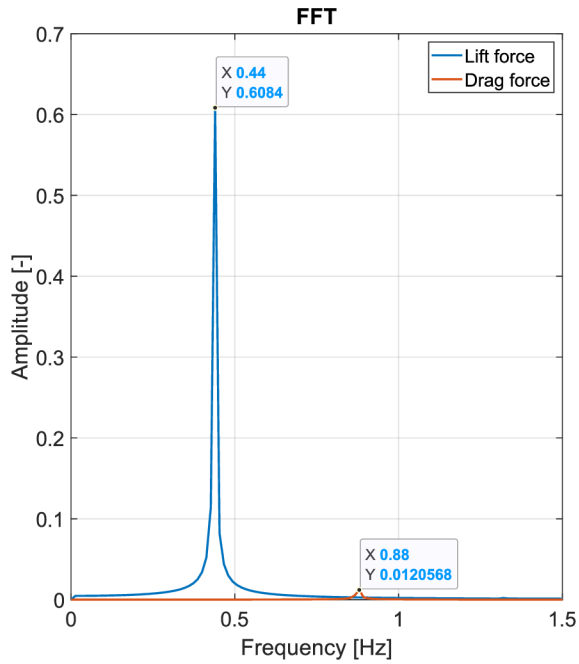

v=0,3 m/s

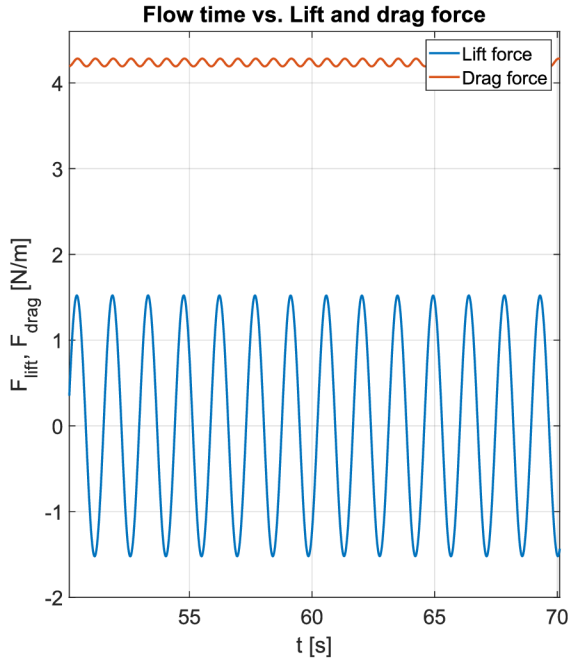
Flow time vs. Lift and drag force
Lift force
Drag force
F_lift, F_drag [N/m]
t [s]

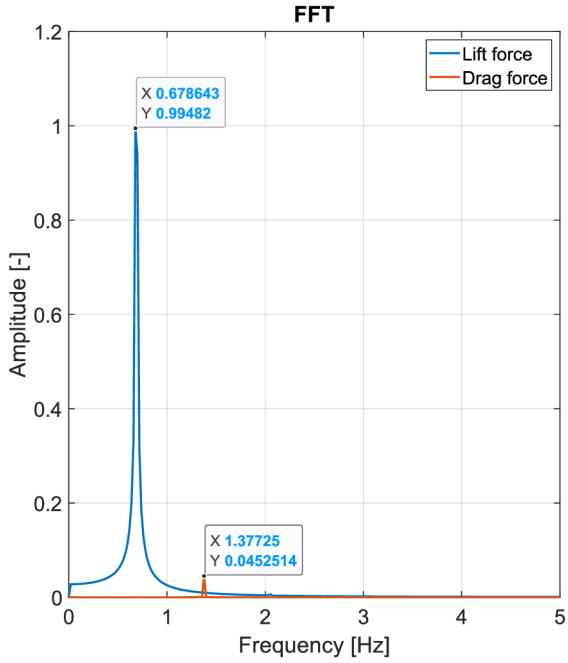
FFT
Lift force
Drag force
X 0.678643
Y 0.99482
X 1.37725
Y 0.0452514
Amplitude [-]
Frequency [Hz]

v=0,4 m/s

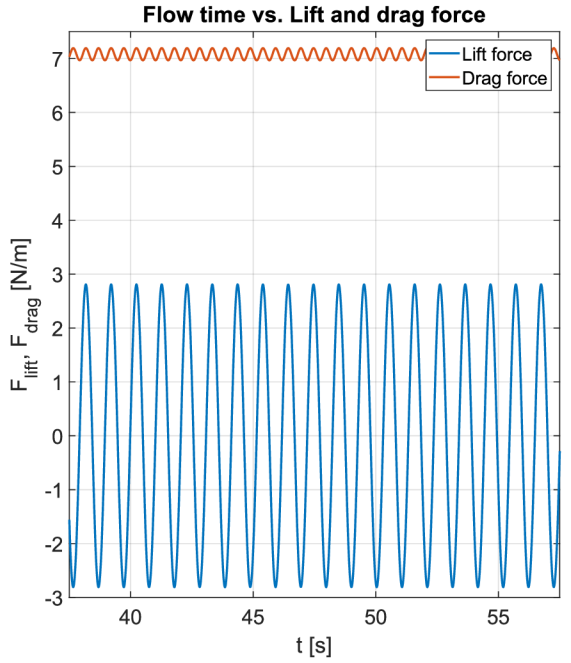
Flow time vs. Lift and drag force
Lift force
Drag force
F_lift, F_drag [N/m]
t [s]

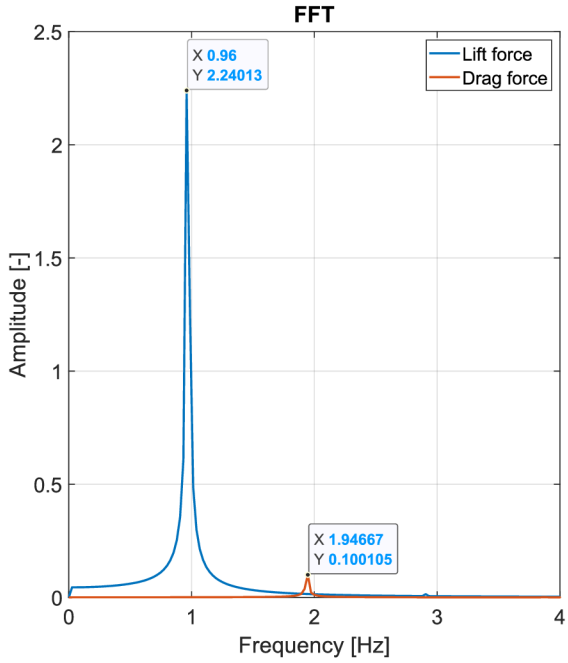
FFT
Lift force
Drag force
X 0.96
Y 2.24013
X 1.94667
Y 0.100105
Amplitude [-]
Frequency [Hz]

v=0,5 m/s

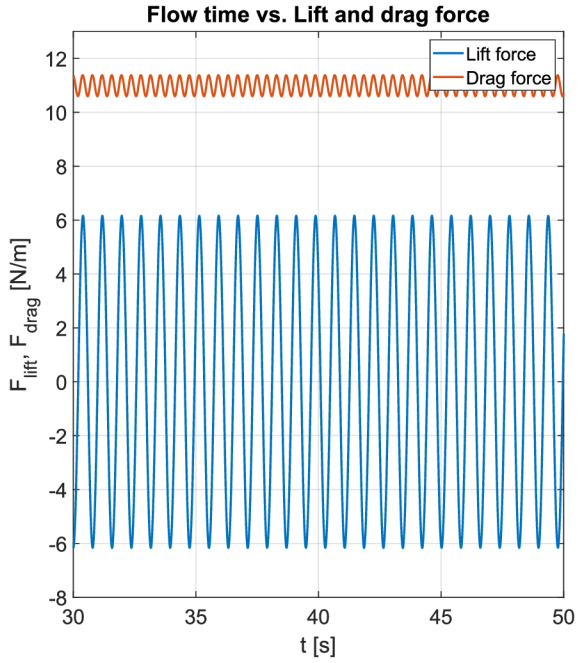
Flow time vs. Lift and drag force
Lift force
Drag force
F_lift, F_drag [N/m]
t [s]

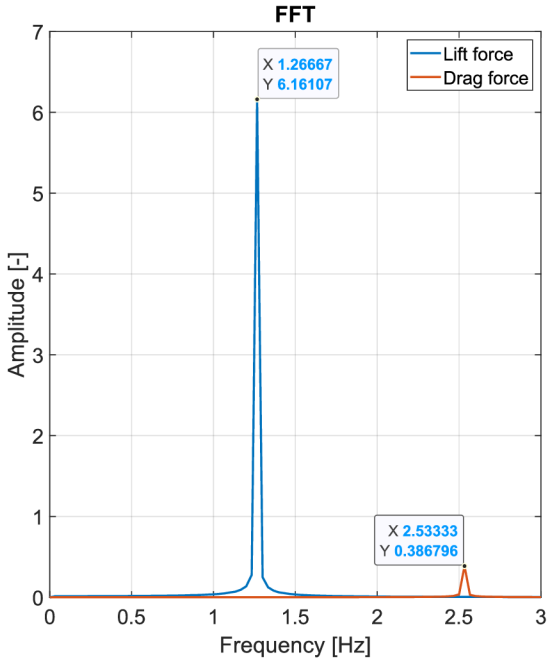
FFT
X 1.26667
Y 6.16107
X 2.53333
Y 0.386796
Lift force
Drag force
Amplitude [-]
Frequency [Hz]

v=0,6 m/s

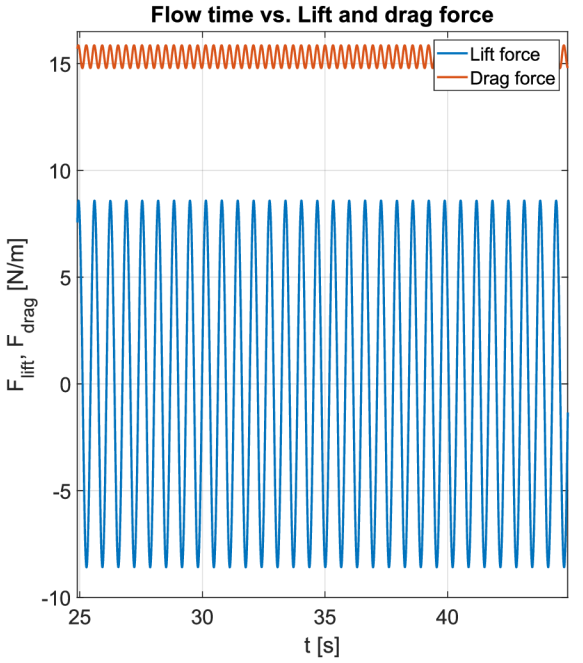
Flow time vs. Lift and drag force
Lift force
Drag force
F_lift, F_drag [N/m]
t [s]

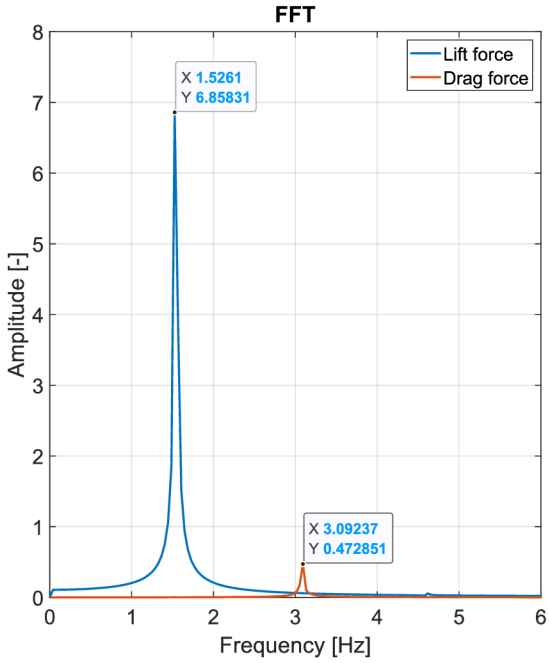
FFT
X 1.5261
Y 6.85831
X 3.09237
Y 0.472851
Lift force
Drag force
Amplitude [-]
Frequency [Hz]

Elliptic cylinder

v=0,1 m/s

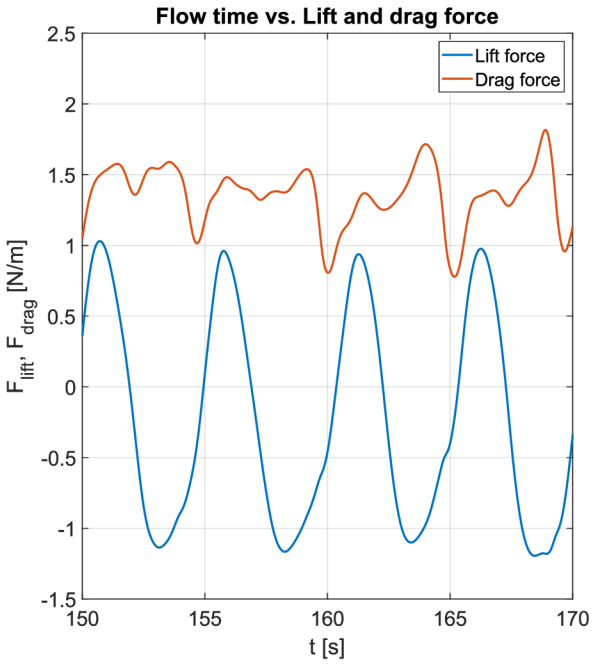

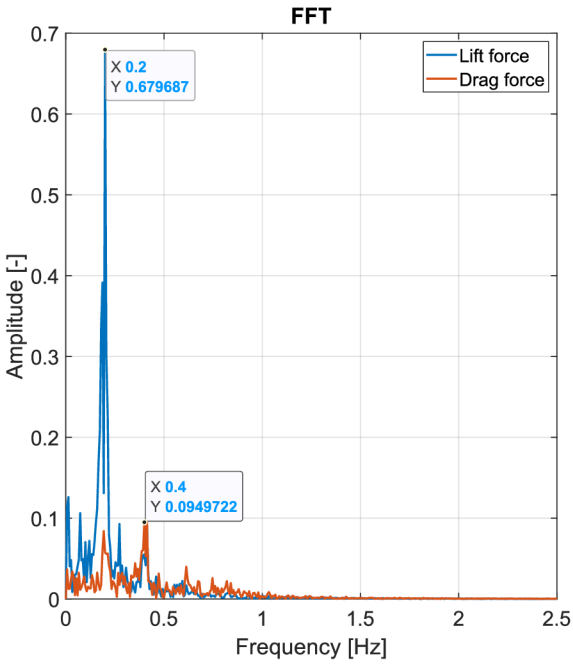

v=0,2 m/s

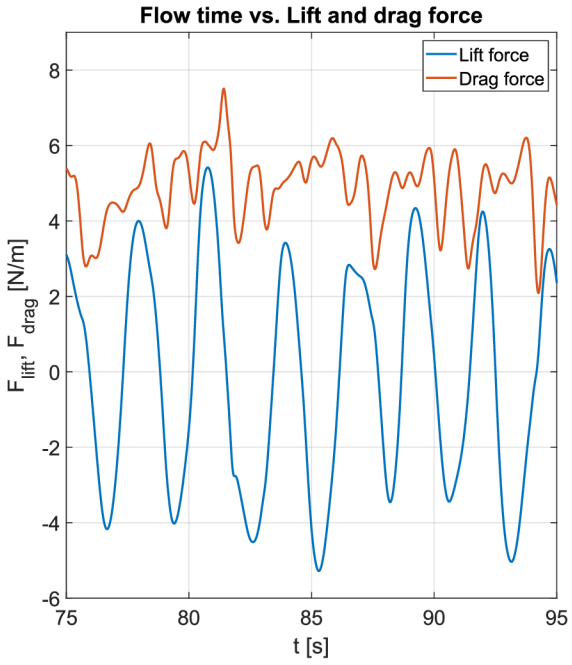

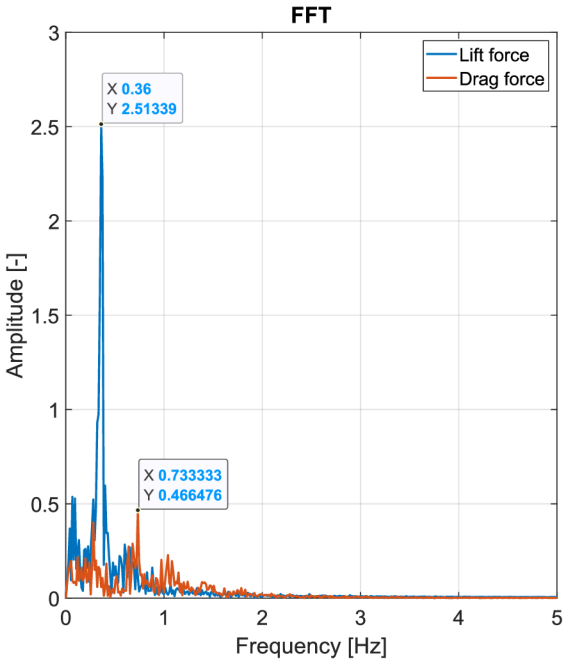

v=0,3 m/s

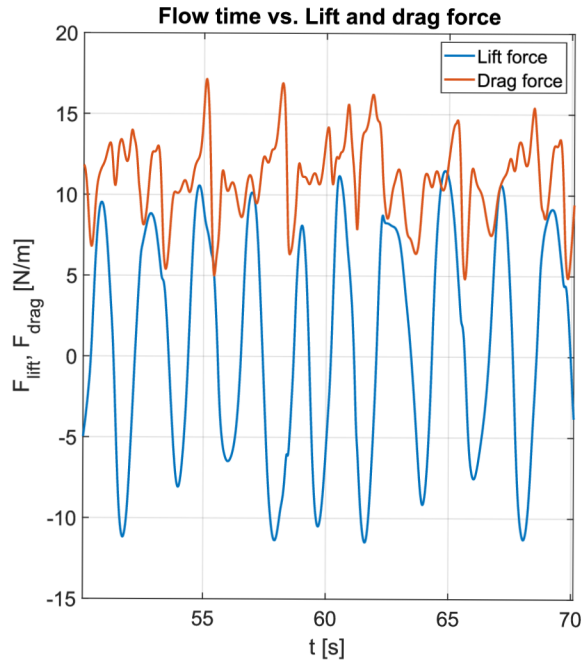
Flow time vs. Lift and drag force
Lift force
Drag force
F_lift, F_drag [N/m]
t [s]

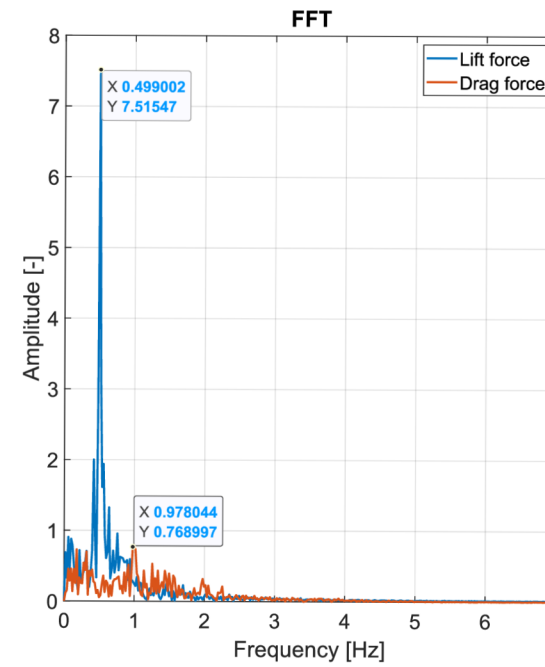
FFT
Lift force
Drag force
X 0.499002
Y 7.51547
X 0.978044
Y 0.768997
Amplitude [-]
Frequency [Hz]

v=0,4 m/s

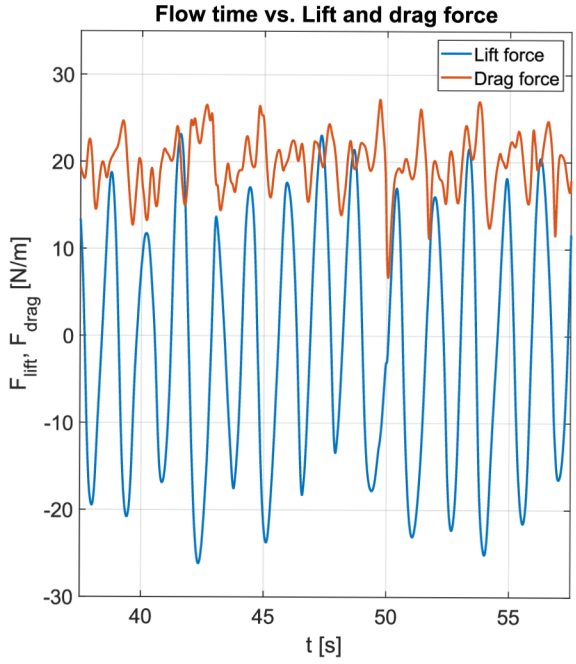
Flow time vs. Lift and drag force
Lift force
Drag force
F_lift, F_drag [N/m]
t [s]

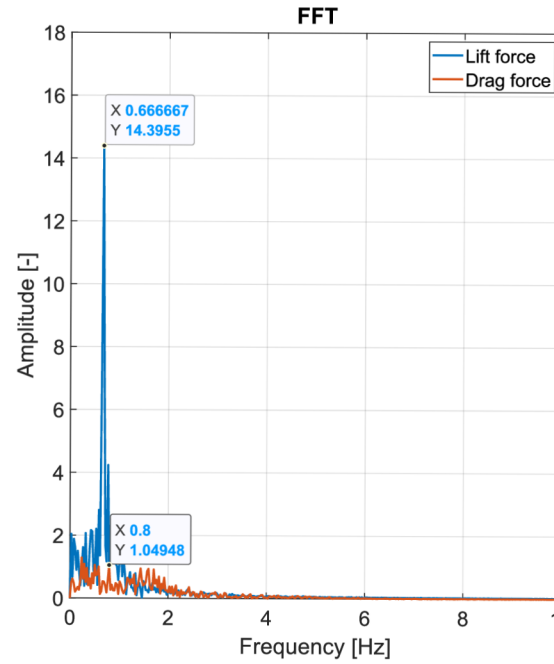
FFT
Lift force
Drag force
X 0.666667
Y 14.3955
X 0.8
Y 1.04948
Amplitude [-]
Frequency [Hz]

v=0,5 m/s

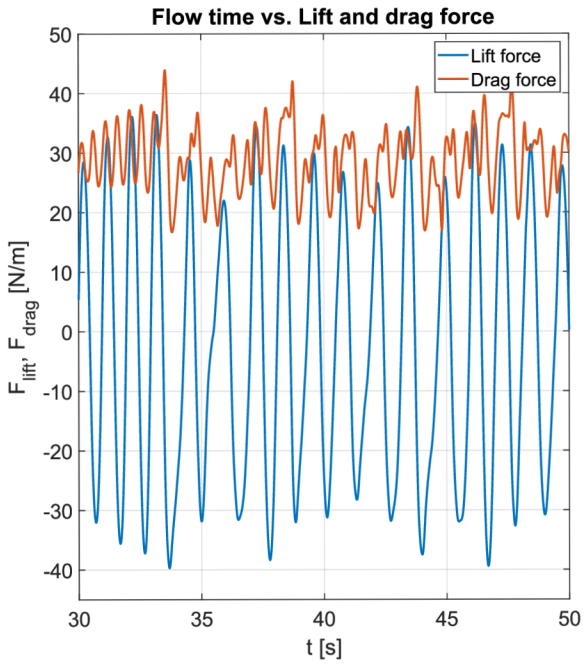
Flow time vs. Lift and drag force
Lift force
Drag force
F_lift, F_drag [N/m]
t [s]

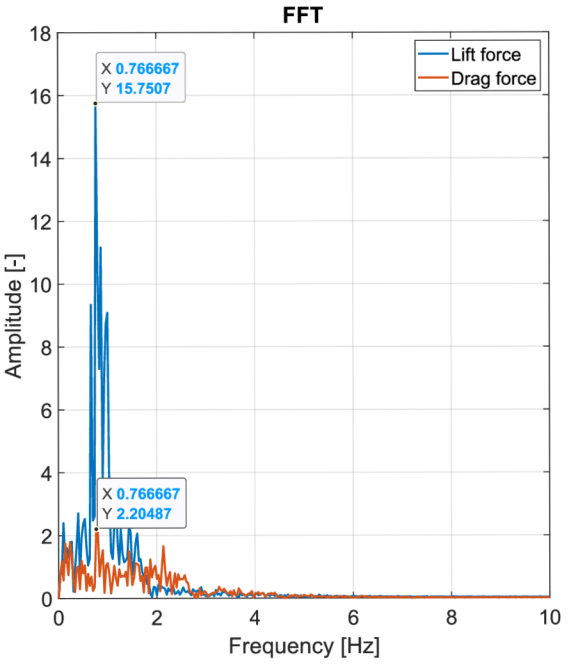
FFT
Lift force
Drag force
X 0.766667
Y 15.7507
X 0.766667
Y 2.20487
Amplitude [-]
Frequency [Hz]

v=0,6 m/s

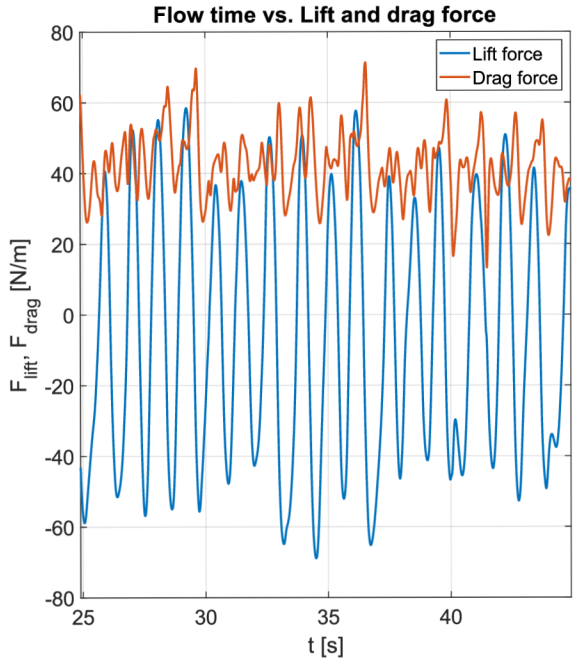
Flow time vs. Lift and drag force
Lift force
Drag force
F_lift, F_drag [N/m]
t [s]

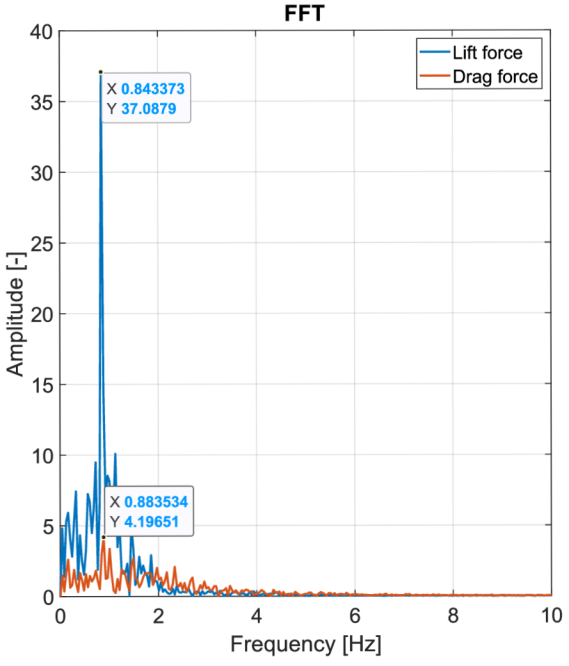
FFT
Lift force
Drag force
X 0.843373
Y 37.0879
X 0.883534
Y 4.19651
Amplitude [-]
Frequency [Hz]

Square cylinder

v=0,1 m/s

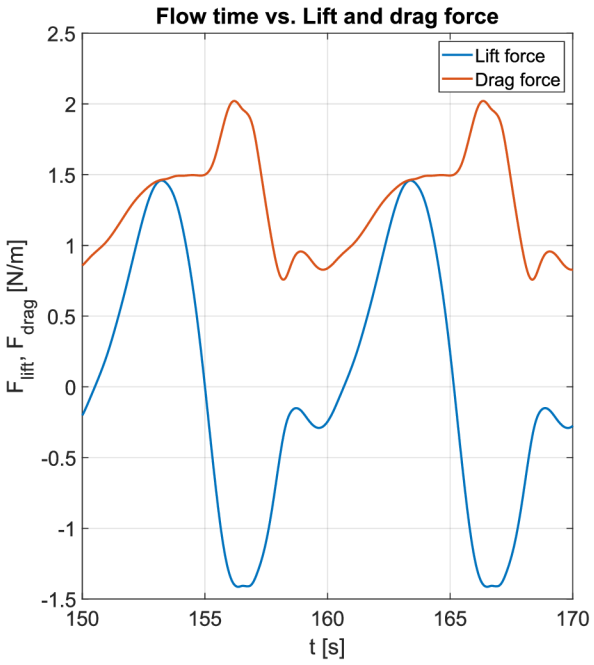

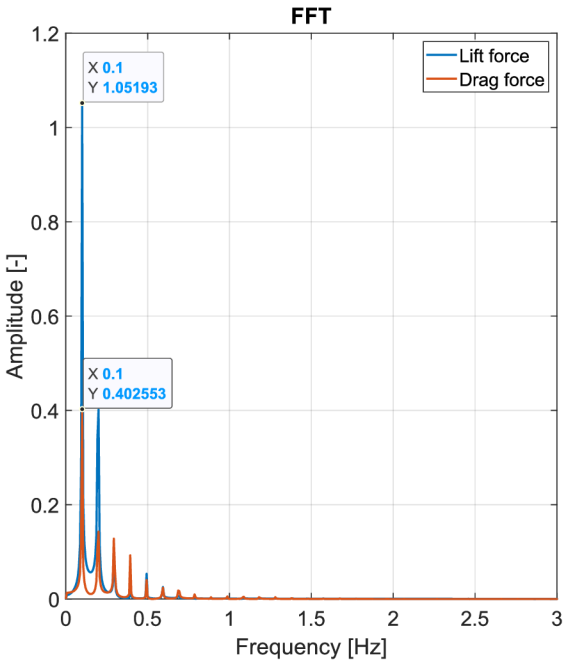

v=0,2 m/s

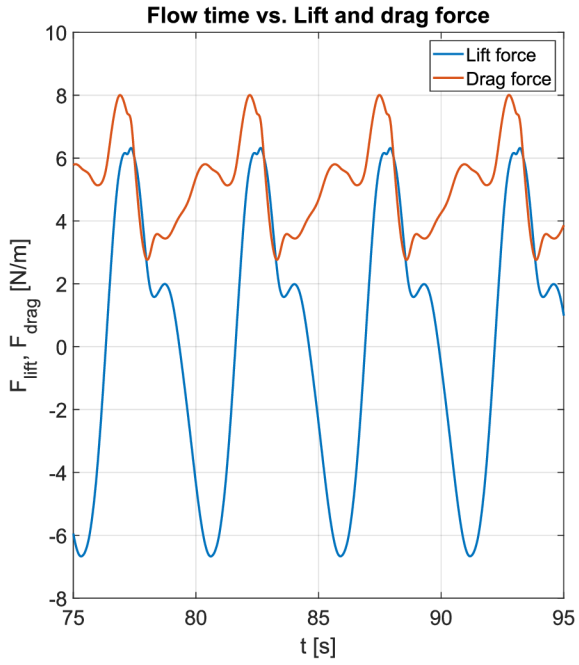

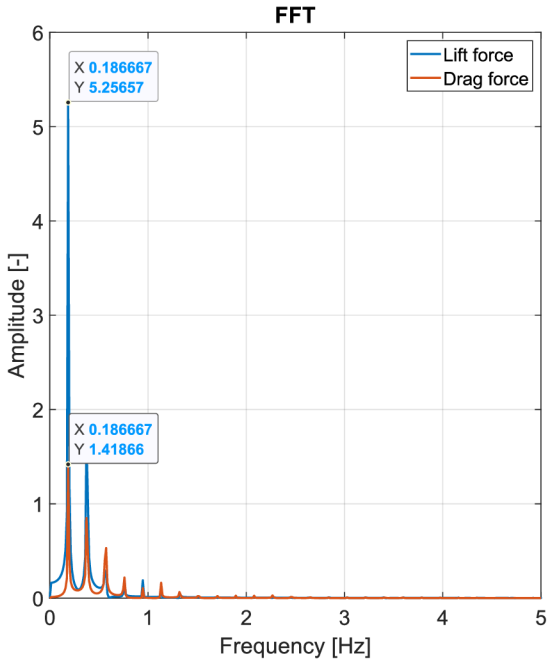

v=0,3 m/s

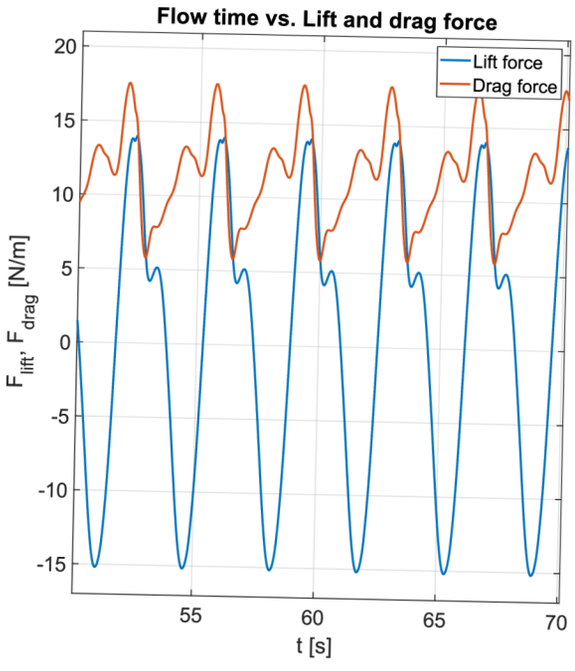
Flow time vs. Lift and drag force
Lift force
Drag force
F_lift, F_drag [N/m]
t [s]

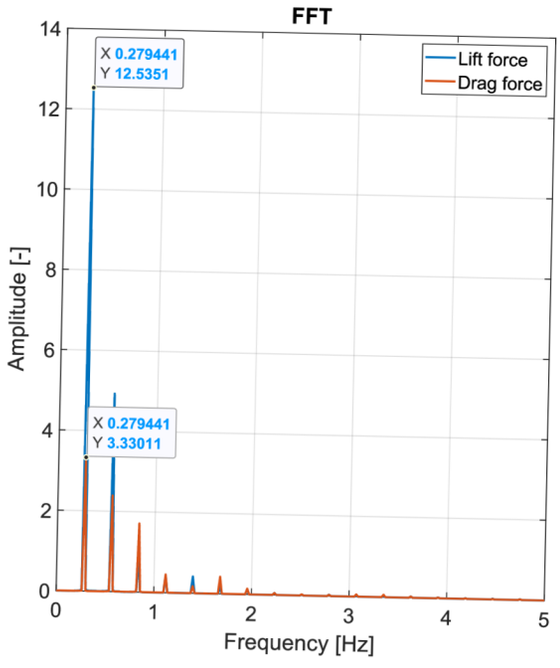
FFT
X 0.279441
Y 12.5351
X 0.279441
Y 3.33011
Lift force
Drag force
Amplitude [-]
Frequency [Hz]

v=0,4 m/s

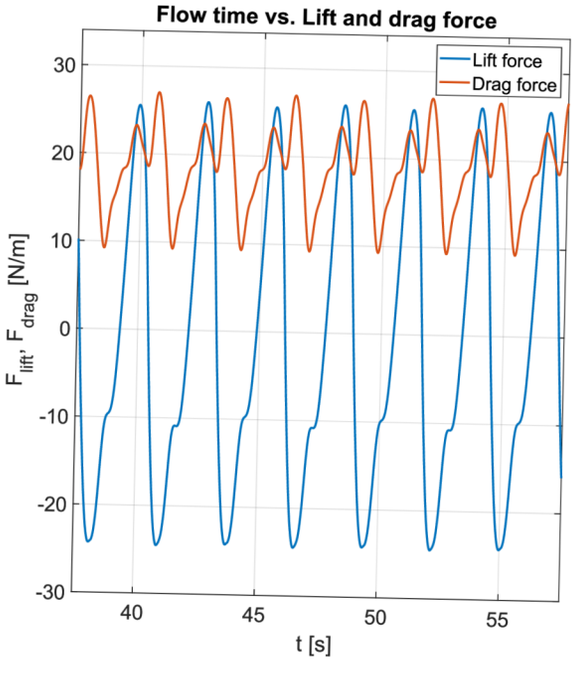
Flow time vs. Lift and drag force
Lift force
Drag force
F_lift, F_drag [N/m]
t [s]

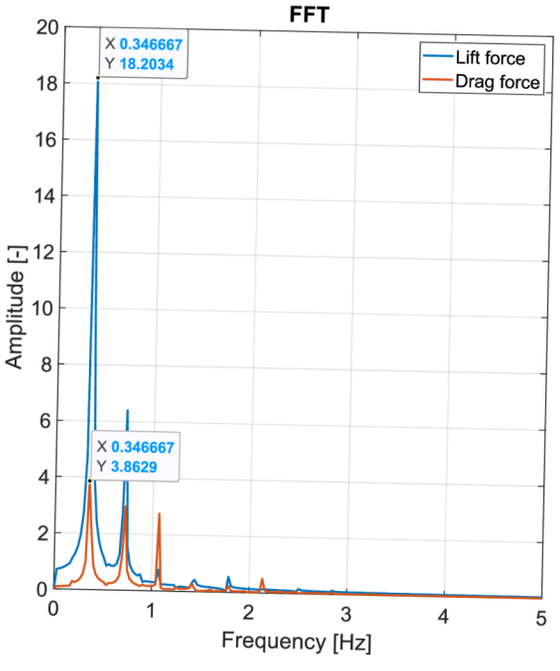
FFT
X 0.346667
Y 18.2034
X 0.346667
Y 3.8629
Lift force
Drag force
Amplitude [-]
Frequency [Hz]

v=0,5 m/s

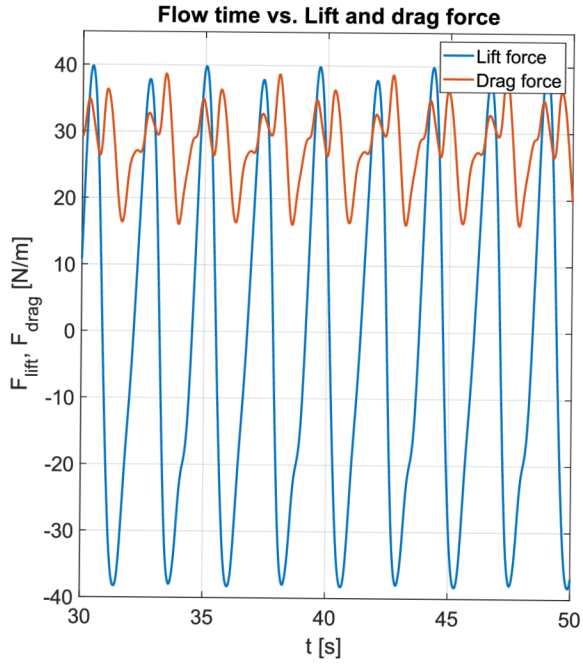
Flow time vs. Lift and drag force
Lift force
Drag force
F_lift, F_drag [N/m]
t [s]

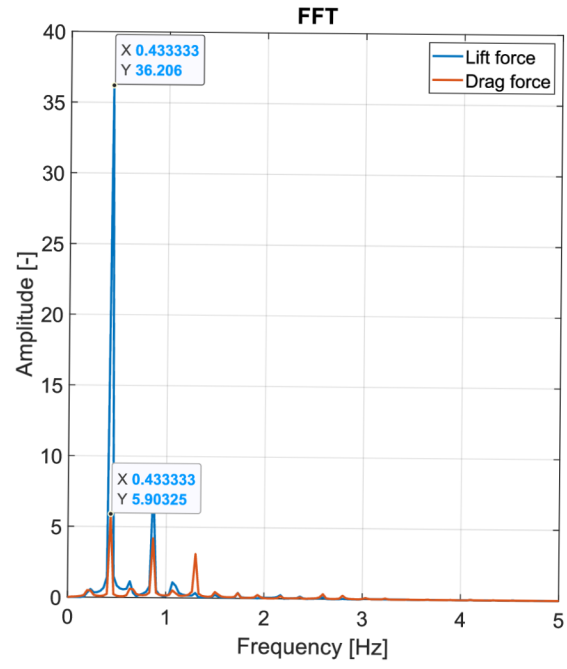
FFT
X 0.433333
Y 36.206
X 0.433333
Y 5.90325
Lift force
Drag force
Amplitude [-]
Frequency [Hz]

v=0,6 m/s

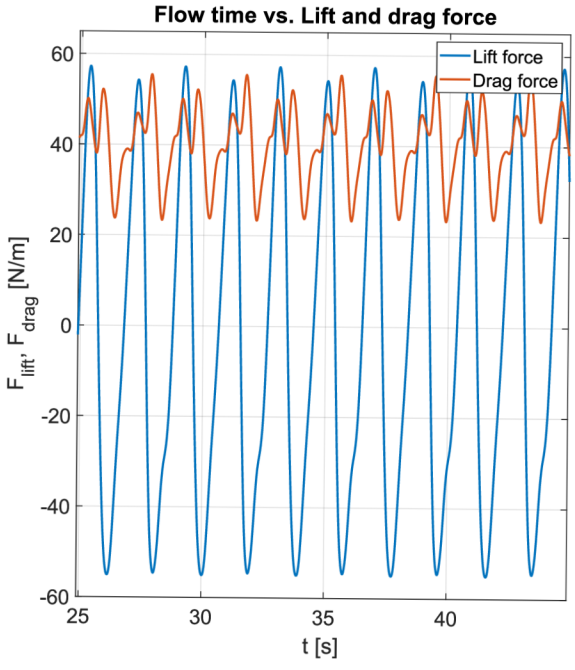
Flow time vs. Lift and drag force
Lift force
Drag force
F_lift, F_drag [N/m]
t [s]

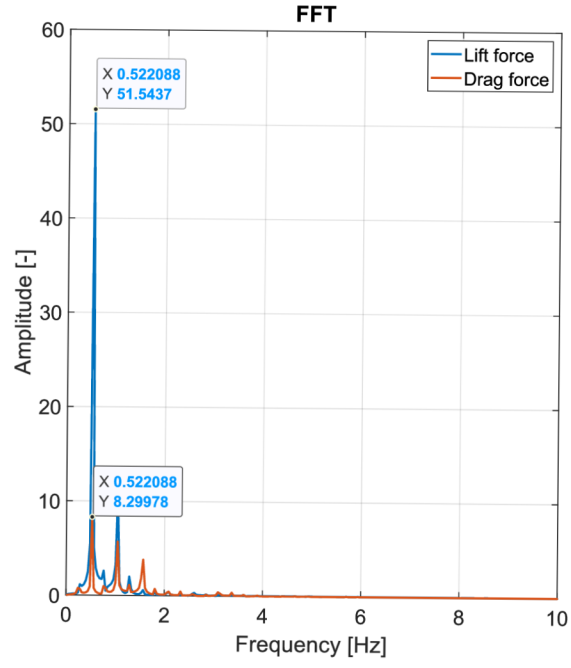
FFT
X 0.522088
Y 51.5437
X 0.522088
Y 8.29978
Lift force
Drag force
Amplitude [-]
Frequency [Hz]

Rectangular cylinder

v=0,1 m/s

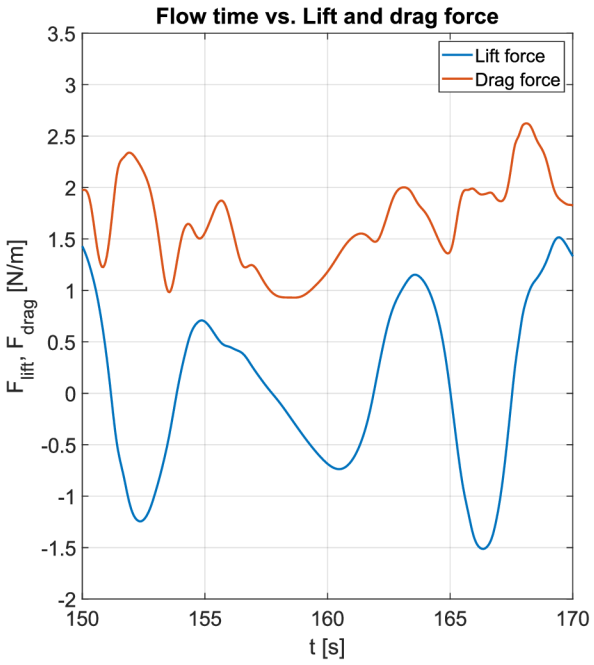

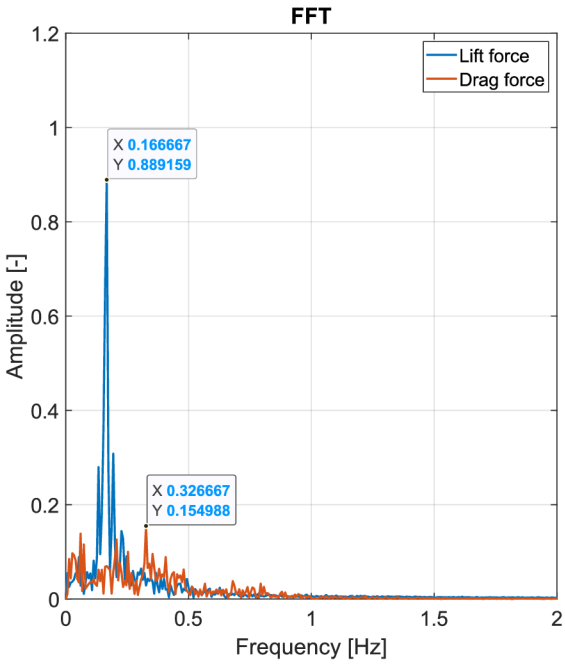

v=0,2 m/s

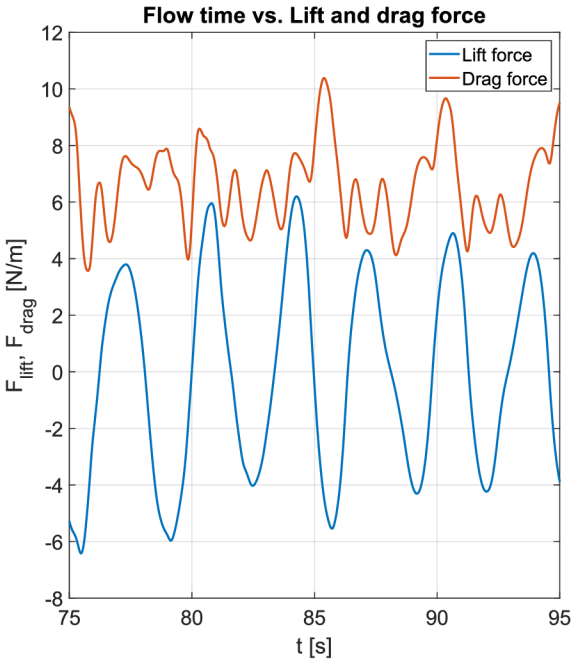

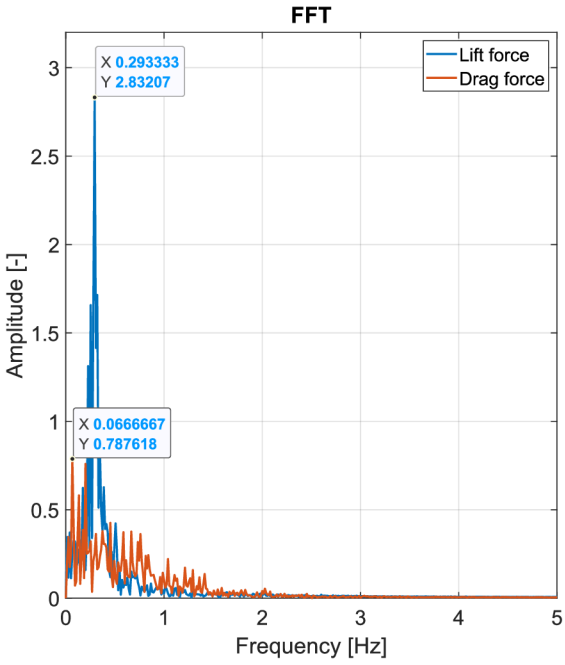

v=0,3 m/s

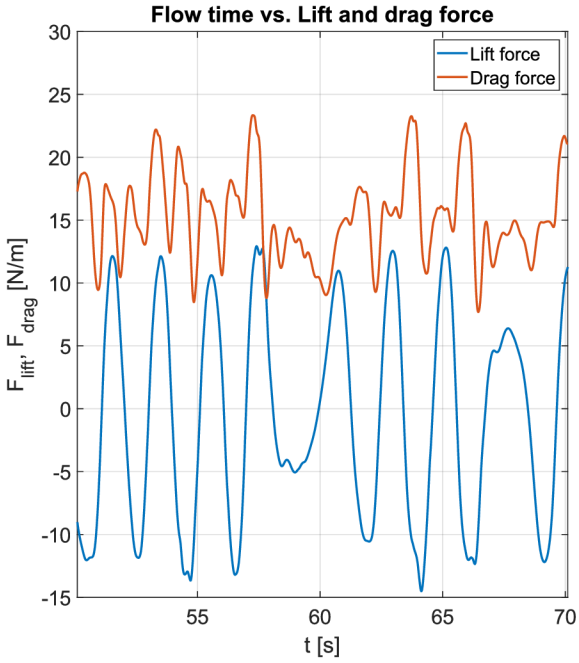
Flow time vs. Lift and drag force
Lift force
Drag force
F_lift, F_drag [N/m]
t [s]

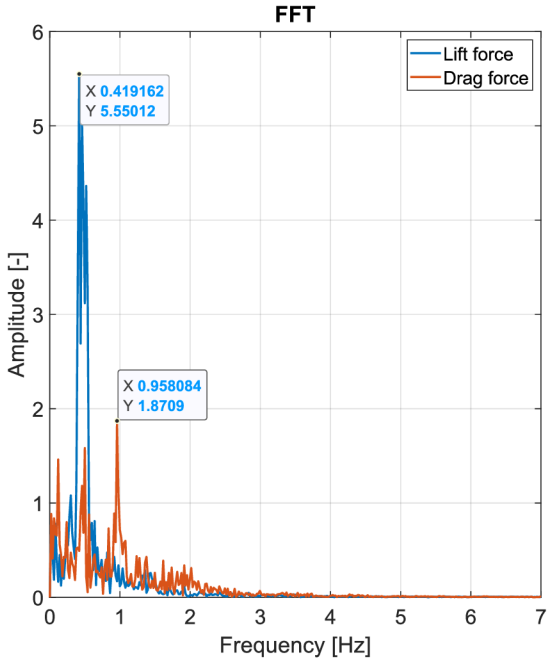
FFT
Lift force
Drag force
X 0.419162
Y 5.55012
X 0.958084
Y 1.8709
Amplitude [-]
Frequency [Hz]

v=0,4 m/s

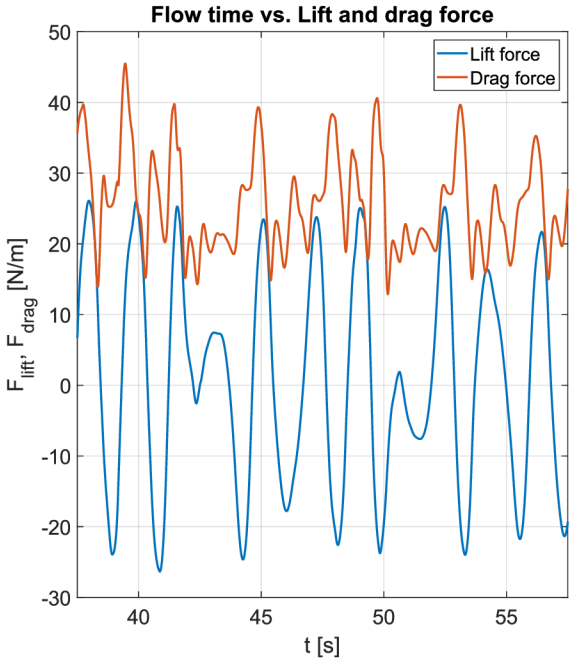
Flow time vs. Lift and drag force
Lift force
Drag force
F_lift, F_drag [N/m]
t [s]

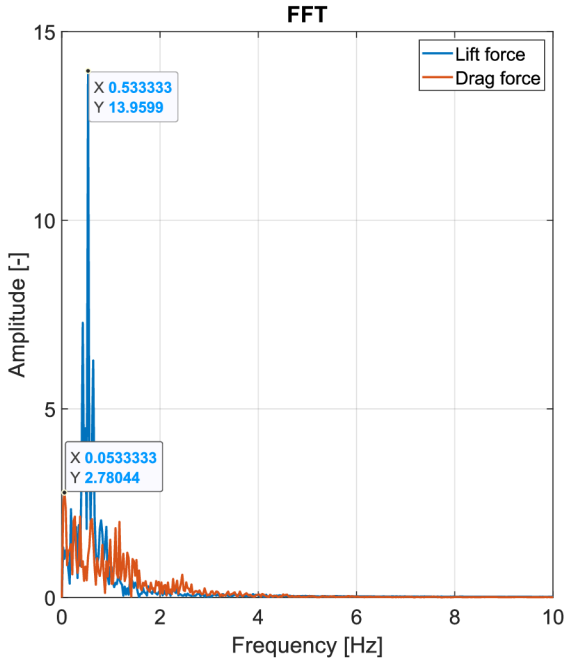
FFT
Lift force
Drag force
X 0.533333
Y 13.9599
X 0.0533333
Y 2.78044
Amplitude [-]
Frequency [Hz]

v=0,5 m/s

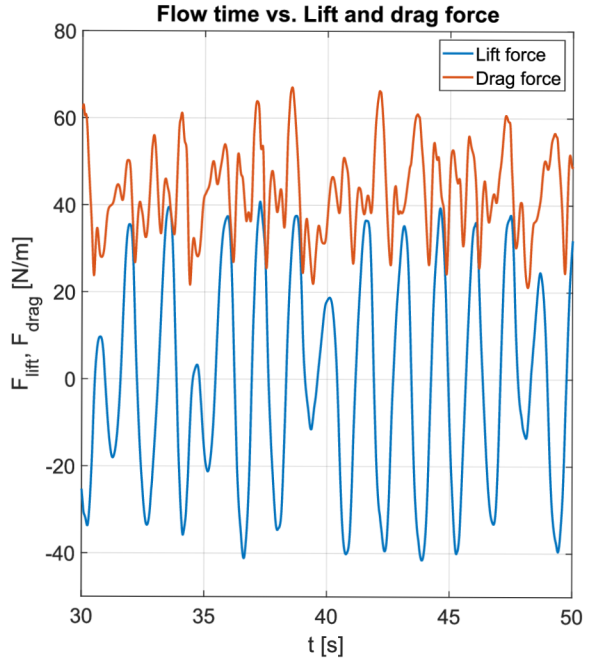
Flow time vs. Lift and drag force
Lift force
Drag force
F_lift, F_drag [N/m]
t [s]

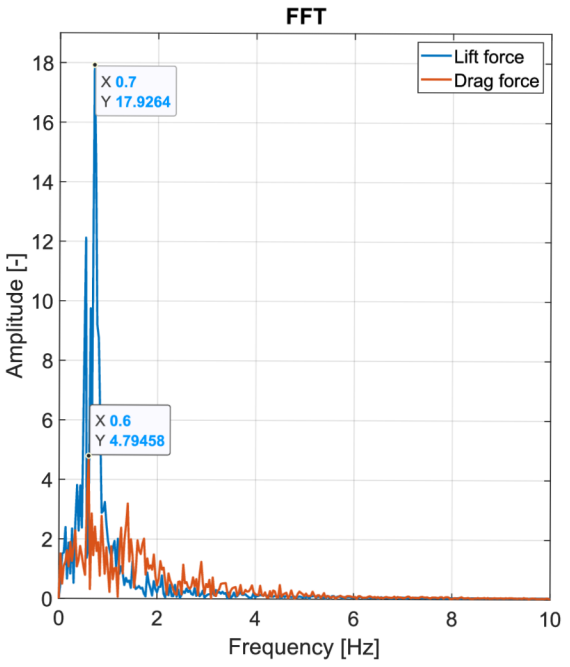
FFT
Lift force
Drag force
X 0.7
Y 17.9264
X 0.6
Y 4.79458
Amplitude [-]
Frequency [Hz]

v=0,6 m/s

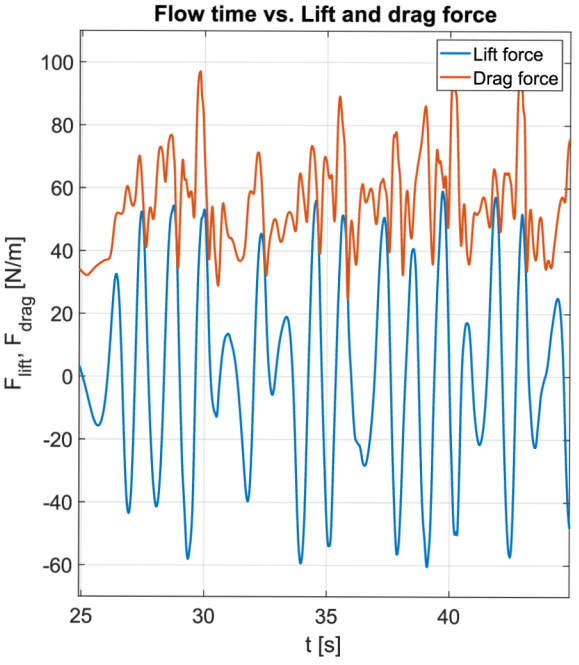
Flow time vs. Lift and drag force
Lift force
Drag force
F_lift, F_drag [N/m]
t [s]

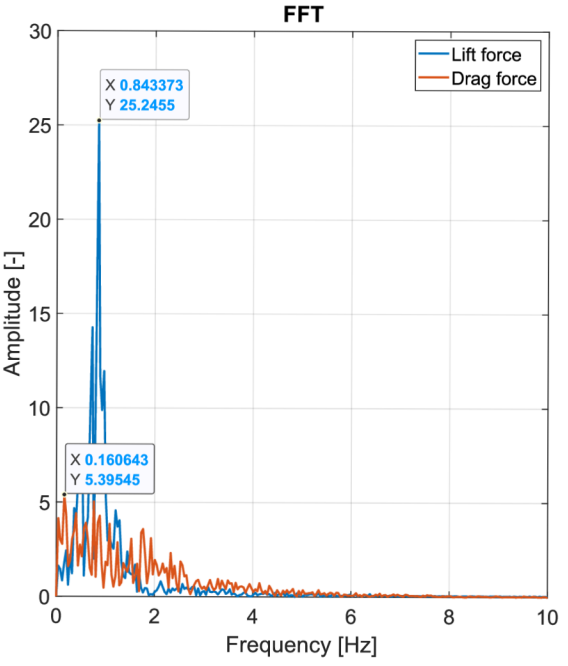
FFT
Lift force
Drag force
X 0.843373
Y 25.2455
X 0.160643
Y 5.39545
Amplitude [-]
Frequency [Hz]

Triangular cylinder

v=0,1 m/s

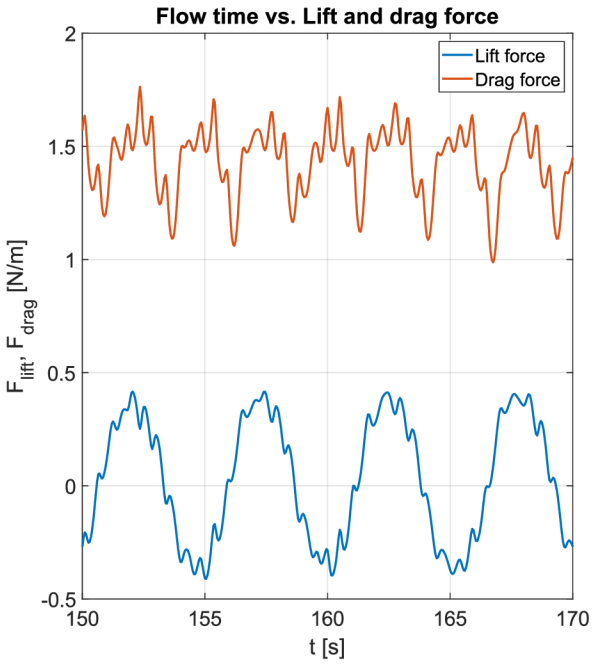

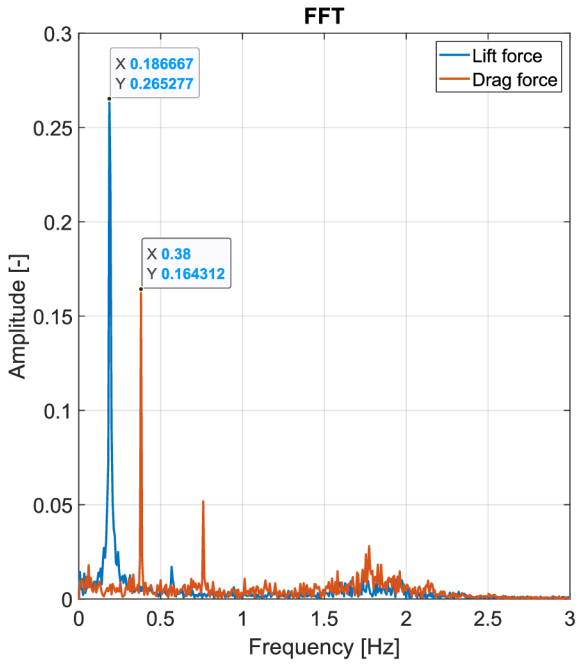

v=0,2 m/s

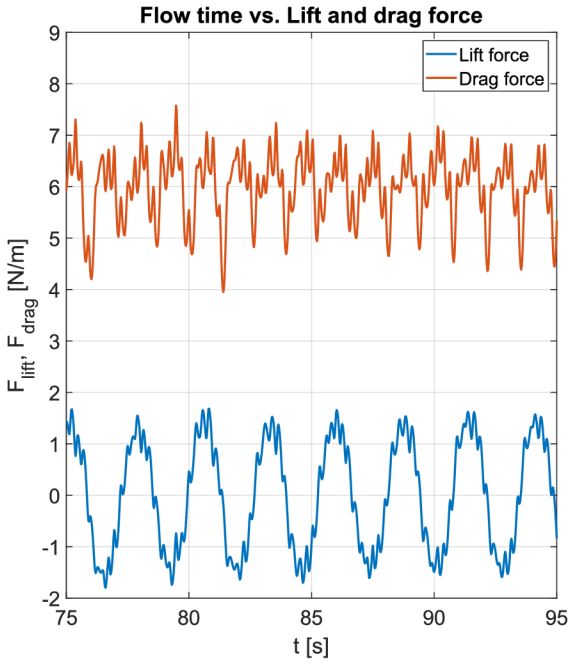

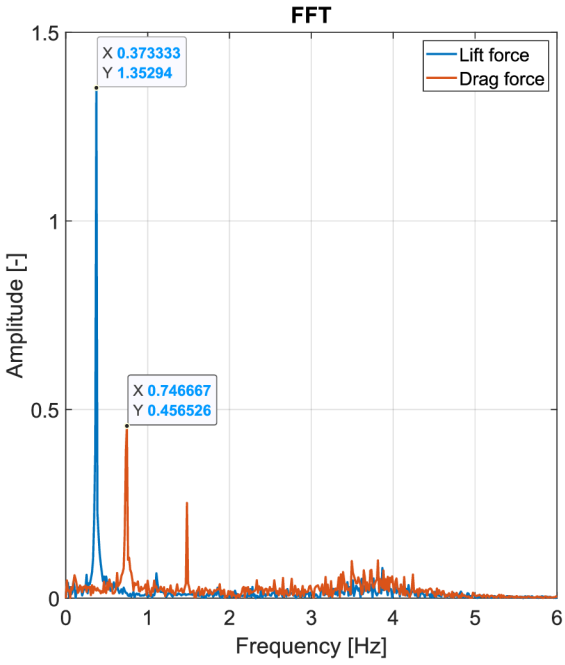

v=0,3 m/s

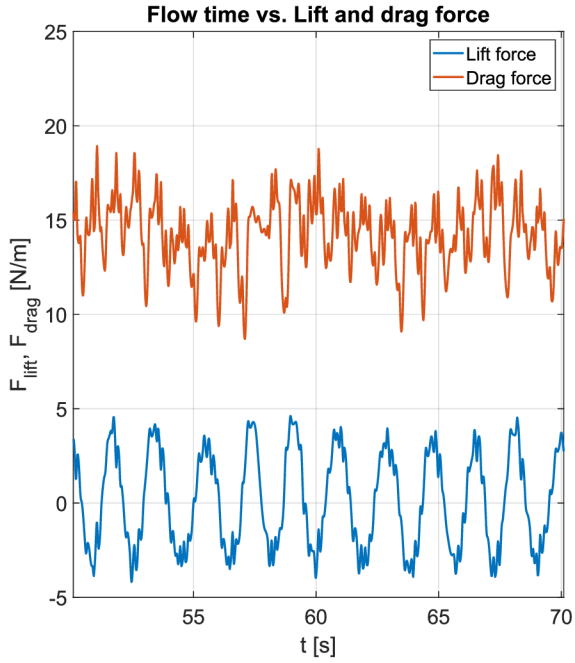
Flow time vs. Lift and drag force
Lift force
Drag force
F_{lift}, F_{drag} [N/m]
t [s]

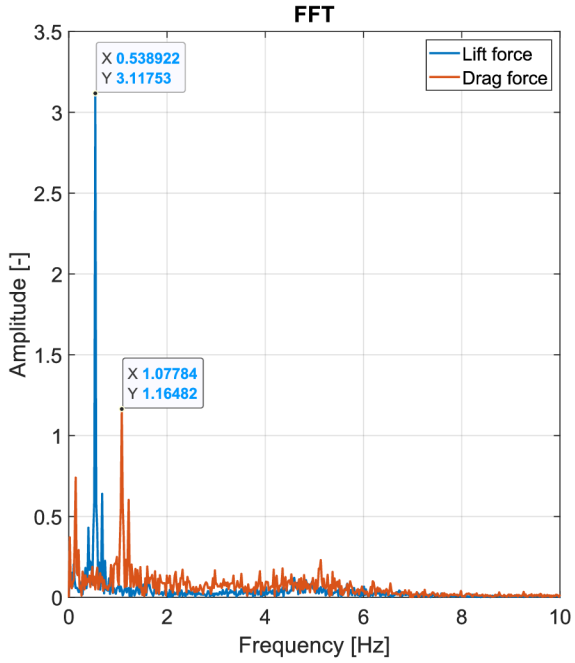
FFT
X 0.538922
Y 3.11753
X 1.07784
Y 1.16482
Lift force
Drag force
Amplitude [-]
Frequency [Hz]

v=0,4 m/s

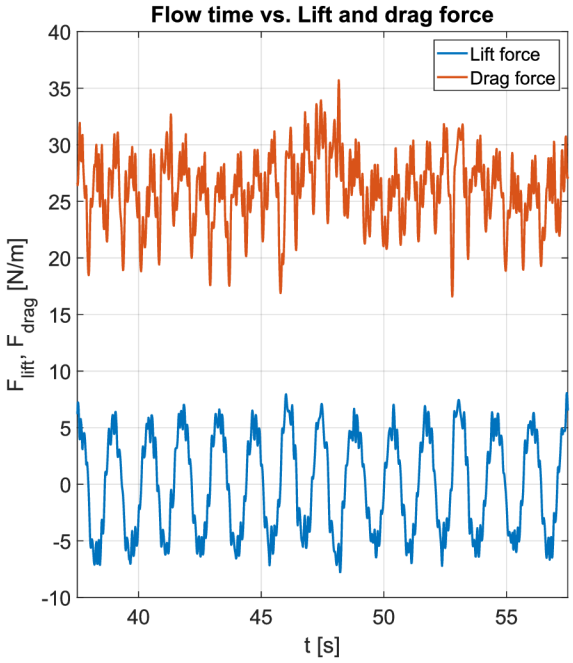
Flow time vs. Lift and drag force
Lift force
Drag force
F_{lift}, F_{drag} [N/m]
t [s]

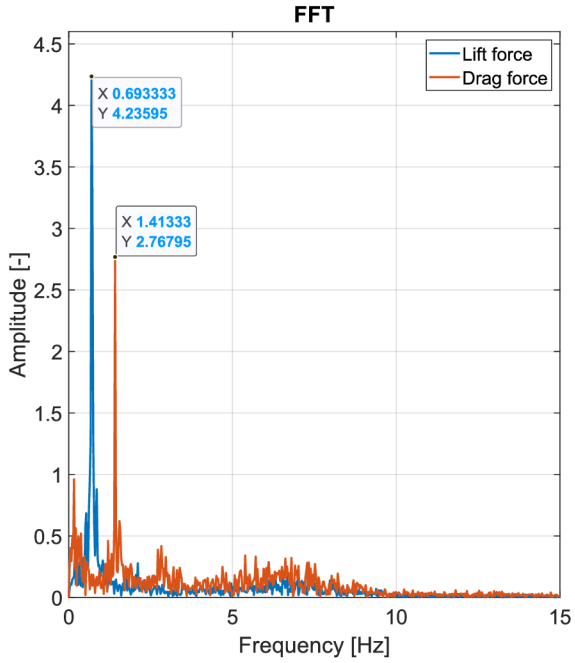
FFT
X 0.693333
Y 4.23595
X 1.41333
Y 2.76795
Lift force
Drag force
Amplitude [-]
Frequency [Hz]

v=0,5 m/s

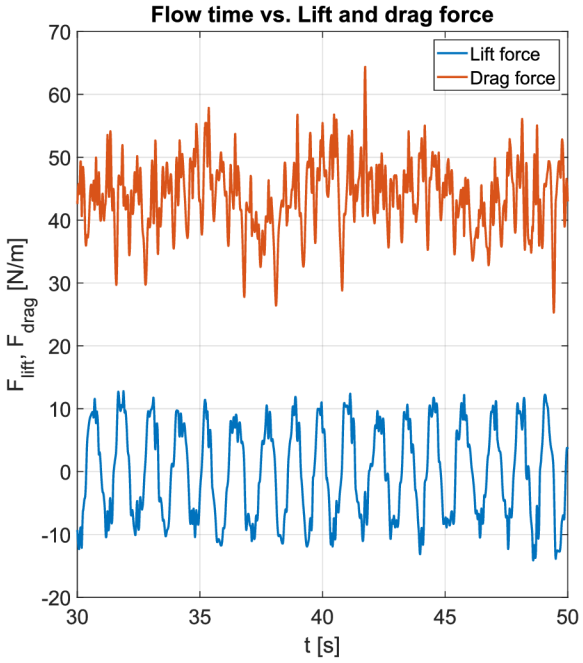
Flow time vs. Lift and drag force
Lift force
Drag force
F_{lift}, F_{drag} [N/m]
t [s]

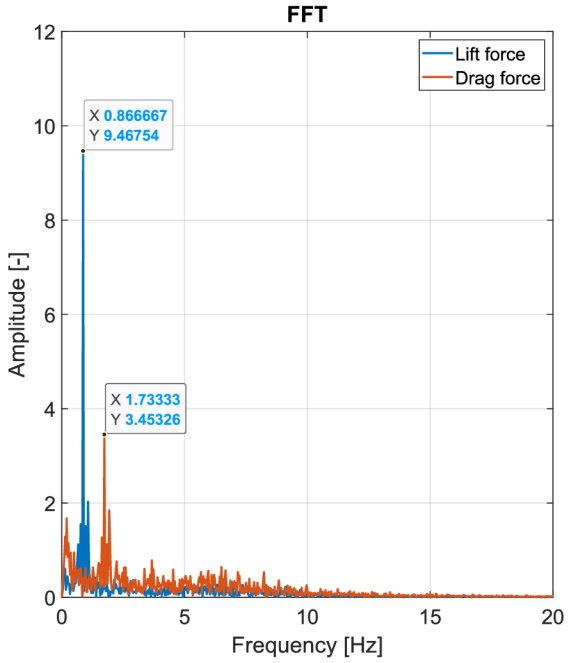
FFT
Lift force
Drag force
X 0.866667
Y 9.46754
X 1.73333
Y 3.45326
Amplitude [-]
Frequency [Hz]

v=0,6 m/s

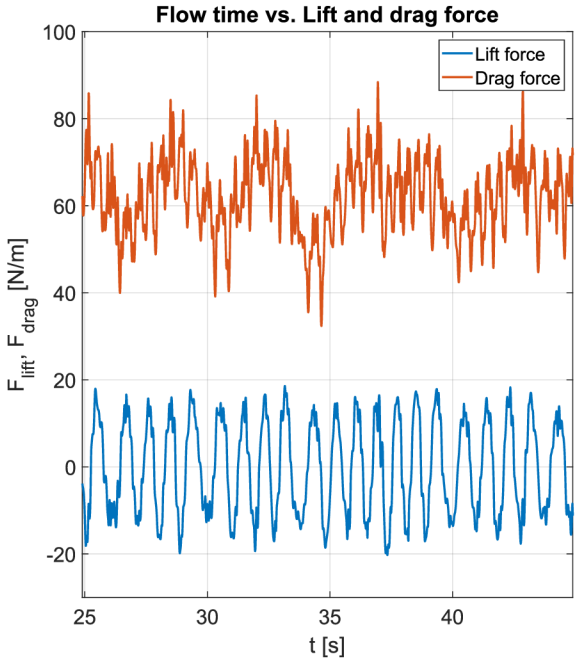
Flow time vs. Lift and drag force
Lift force
Drag force
F_{lift}, F_{drag} [N/m]
t [s]

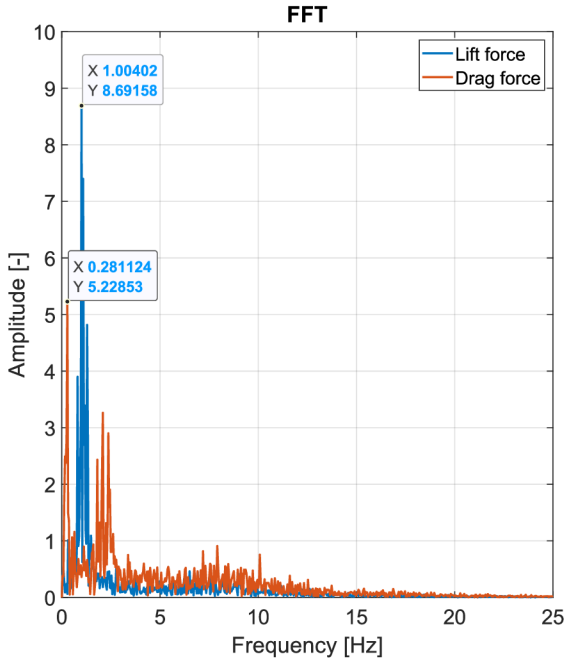
FFT
Lift force
Drag force
X 1.00402
Y 8.69158
X 0.281124
Y 5.22853
Amplitude [-]
Frequency [Hz]